Collective phenomena in active Brownian particles with feedback controlled interaction rules

Dissertation for the degree of
Doctor of Natural Sciences (Dr.rer.nat.)

submitted by
Tobias Doyle Bäuerle

at the

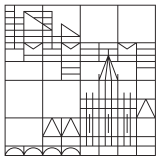

Faculty of Sciences
Department of Physics

Konstanz, 2020

Date of oral examination: 22 October 2020

First reviewer: Prof. Dr. Clemens Bechinger

Second reviewer: Prof. Dr. Peter Nielaba

Abstract

The formation of groups by animals or other living organisms is a widespread phenomenon in nature. Individuals coordinate their actions to gain an advantage compared to being isolated, for example regarding the protection from predators or the optimisation of foraging. The organisation principle is often poorly understood because it is not feasible to control the interactions between individuals. Therefore, investigating their collective behaviour demands versatile model systems that allow to control the interactions precisely. Due to their outstanding experimental accessibility, active Brownian particles are suitable candidates for this purpose.

In this thesis, I present the experimental realisation of programmable interaction rules in a suspension of active Brownian particles with light-activated self-propulsion. Using feedback controlled laser illumination, the propulsion velocity of each particle can be adjusted individually. In addition, asymmetric illumination allows to influence the propulsion direction by active reorientation. With different interaction rules, the performance and versatility of the experimental system is demonstrated.

First, the applicability of feedback control is confirmed by navigating single particles towards a target using different control strategies. The efficiency of these strategies is compared regarding possible limitations of resources. Subsequently, collective phenomena in a group of active Brownian particles are investigated with interaction rules inspired by biological systems. Imitating the quorum sensing of bacteria, particles that change their motility as a response to the local density, can form regions with enhanced particle density. Size, density and shape of these regions strongly depend on the specific response of the particles. Furthermore, active Brownian particles organise in cohesive collective states when following an interaction rule which is motivated by the behaviour of social animals. Detailed investigations of the observed rotating swirls, show that they are remarkably robust against internal and external perturbations. In addition, the transition between swirls and unordered swarms is analysed, revealing analogies to a second-order phase transition in thermal equilibrium.

These findings highlight the versatility of individually controlled active Brownian particles as a model system. The ability to test interactions under experimental conditions can be expected to be highly relevant for future research of collective behaviour.

Zusammenfassung

Die Organisation von Tieren und anderen lebenden Organismen in Gruppen ist in der Natur weit verbreitet. Hierbei koordinieren Individuen ihr Verhalten um sich einen Vorteil zu verschaffen, beispielsweise zum Schutz vor Raubtieren oder zur Optimierung der Nahrungssuche. Oftmals sind die Details der Gruppenbildung nur schlecht verstanden, da die Interaktionen zwischen Individuen nicht kontrolliert werden können. Um das kollektive Verhalten zu untersuchen, sind daher flexibel einsetzbare Modellsysteme nötig, bei denen die Interaktionen präzise gesteuert werden können. Aktive Brownsche Schwimmer sind aufgrund ihrer hervorragenden experimentellen Zugänglichkeit optimal für diesen Zweck geeignet.

In dieser Arbeit stelle ich die experimentelle Umsetzung eines derartigen Modellsystems vor. Interaktionen zwischen aktiven Brownschen Schwimmern, deren Antrieb durch Beleuchtung aktiviert wird, können unter Verwendung eines Feedback-gesteuerten Lasersystems frei programmiert werden. Dabei wird die Schwimmgeschwindigkeit durch die Intensität der Beleuchtung eingestellt. Zusätzlich führt eine asymmetrische Beleuchtung zu einer Änderung der Schwimmrichtung. Durch die Verwendung unterschiedlicher Interaktionsregeln wird die Leistungsfähigkeit und Vielseitigkeit des experimentellen Systems veranschaulicht.

Zunächst wird die Anwendbarkeit der Feedback-Kontrolle überprüft indem einzelne Schwimmer zu einem Ziel navigiert werden. Die Effizienz der verwendeten Kontrollstrategien wird dann bezüglich verschiedener Größen verglichen, deren Verfügbarkeit bei einer realen Anwendung eingeschränkt sein könnte. Anschließend werden kollektive Phänomene untersucht, die durch biologisch inspirierte Interaktionsregeln auftreten. Wenn die Schwimmer, in Anlehnung an Quorum Sensing bei Bakterien, ihre Geschwindigkeit in Abhängigkeit der lokalen Dichte verändern, können sich Gebiete mit gesteigerter Dichte an Schwimmern bilden. Dabei hängen Größe, Dichte und Form dieser Bereiche stark davon ab, wie die Schwimmer ihre Umgebung wahrnehmen und darauf reagieren. Des Weiteren organisieren sich aktive Brownsche Schwimmer in kohäsiven, kollektiven Zuständen, wenn ihr Verhalten durch eine Interaktionsregel bestimmt wird, die dem Verhalten von Tieren nachempfunden ist. Eine detaillierte Untersuchung offenbart eine bemerkenswerte Stabilität der entstehenden Vortex-Zustände gegen innere und äußere Einflüsse. Zudem zeigen sich Ähnlichkeiten zwischen dem Übergang von Vortex zu ungeordnetem Schwarm

und Phasenübergängen zweiter Ordnung im thermischen Gleichgewicht.

Diese Ergebnisse verdeutlichen die Vielseitigkeit von aktiven Brownschen Schwimmern als Modellsystem. Es ist anzunehmen, dass die Möglichkeit, unterschiedlichste Interaktionen unter experimentellen Bedingungen zu untersuchen, zukünfitg von großem Interesse für die weitere Erforschung von kollektivem Verhalten sein wird.

Contents

Introduction

The observation of animal groups in nature reveals an extensive amount of impressive phenomena. One can observe birds flying together in well-aligned flocks which are still able to rapidly change their direction, fish swimming in rotating groups that suddenly align and move in the same direction, or ants moving in trails towards a food source and back to the nest. In all these cases, a large number of individuals coordinate their behaviour resulting in the formation of complex patterns. Because of the substantial group sizes, it is obvious that the behaviour is not globally coordinated, but instead interactions between neighbours determine the global properties of the group. The concept, that order emerges only from interactions within a system, is known as self-organisation. It is not exclusive to animals (or biology in general), but can also be found in inanimate physical or chemical systems [5, 6]. However, self-organisation is particularly important for animals as the coordination of individuals often implies an advantage for each individual compared to being isolated [7]. Consequently, self-organisation is found in most living organisms, including bacteria, insects, fish, birds and humans [8].

The investigation of the collective behaviour of animals has drawn considerable attention in the last decades. In order to understand how local interactions between individuals lead to the formation of complex patterns, it is necessary to decipher the underlying interactions between individuals and to analyse the impact of modifications to the global properties of the group. Because it is typically not feasible to manipulate the interactions between animals in a controlled fashion, modelling and numerical simulations are important tools to study collective behaviour [7]. Meanwhile, various models are available which can reproduce typical collective states found in animals, e.g. unordered swarms, polarised flocks or rotating swirls [9, 10]. The development of the models commonly follows two different approaches. On the one hand, models can include only simple interactions between individuals. These interactions are often based on behavioural priorities of animals, e.g. avoidance of collisions and isolation [9]. The advantage of this approach is the possibility to determine which minimal requirements lead to a certain behaviour. However, these models resemble the real system only on a qualitative level. On the other hand, models can be constructed from the investigation of interactions between individuals in experiments [11–13]. Following this approach, models resemble reality in

more detail, but it is often not obvious which aspects of the observed interactions are required and which are unimportant for the emerging collective states.

Although simulating such models provides insights on the ingredients needed to obtain specific collective states, these simulations are only able to capture a simplified version of the real system. For example, differences in the individual behaviour, possible hydrodynamic interactions or additional sources of perturbations are typically neglected. However, such effects can drastically change the resulting collective behaviour [14] which makes experimental validation of the models important. Because interactions between animals cannot be controlled easily, model systems with precisely controllable interactions are required. As I will show in the following, suspensions of self-propelled colloidal particles (active Brownian particles) can be used for this purpose.

Colloidal suspensions consist of nano- to micrometre-sized particles which are dispersed in a liquid. Due to the small size of colloidal particles, their dynamics are strongly affected by thermal fluctuations and, in absence of additional interactions, their motion is diffusive. This is called Brownian motion and arises from the random collisions of solvent molecules with the particle. Because colloidal particles are significantly larger than atoms or molecules, their dynamics are comparably slow and the relevant time scales are typically on the order of milliseconds to hours. Because of these properties, colloidal suspensions have an outstanding experimental accessibility. Slow dynamics and particle sizes similar to the wavelength of visible light allow data acquisition using video microscopy. Furthermore, particles and also interactions between them can be manipulated easily and with high precision, e.g. by the use of optical tweezers [15]. Consequently, colloidal suspensions are frequently used as model systems for the investigation of effects that are otherwise difficult to observe experimentally. Some examples are the formation and melting of crystals [16, 17], glass transitions [18] and friction [19]. In addition, colloidal suspensions can easily be driven out of equilibrium which allows their use in the investigation of stochastic thermodynamics [20–23].

Reproducing the collective behaviour of self-propelling living organisms in a system of colloidal particles requires that these can self-propel as well. The first self-propelling colloidal particles were presented by Paxton et al. in 2004: bi-metallic rods made from gold and platinum self-propel by the catalytic decomposition of hydrogen-peroxide [24]. The general concept of such self-propelling particles is that they are able to locally convert energy to directed motion [25]. Because the particles are still subjected to Brownian diffusion, the resulting motion is a combination of both effects and hence they are called active Brownian particles. Meanwhile, various propulsion mechanisms have been developed of which some are activated by light [26–28] and therefore, in principle, allow the adjustment of the propulsion on a single particle level.

In this thesis I present the implementation of freely programmable interaction rules in a suspension of active Brownian particles. Combining the light-activated self-propulsion of particles in a binary liquid with feedback controlled, individual laser illumination, the propulsion properties of each particle can be set independently, according to the interaction rule. The different interaction rules applied throughout the thesis illustrate the flexibility of the experimental system to model various aspects of collective behaviour. Furthermore, they reflect the increasing possibilities due to the continuous improvement of the experimental setup.

Chapter 1 provides a brief overview of the collective behaviour in living organisms. Some particularly important collective states and possibilities to model collective behaviour are discussed.

Chapter 2 introduces active Brownian motion. It starts with the development of synthetic active Brownian particles, followed by the mathematical description of active Brownian motion and some examples of collective phenomena that can be observed even in the absence of programmable interactions.

Chapter 3 presents the details of the experimental system. The first part summarises the self-propulsion of active Brownian particles by demixing of a binary mixture composed of water and 2,6-lutidine. Then the experimental setup is discussed, in particular the acousto-optical deflector that allows to steer the illuminating laser beam to the position of each particle. The focus of the chapter lies on the various calibrations that are needed to ensure a well-defined and reproducible control over the propulsion of individual particles.

Chapter 4 is the first chapter in which a feedback controlled change of the swimming velocity of active Brownian particles is realised. Single particles are steered towards a target using different control strategies. These strategies determine if the particle's self-propulsion is turned on or off, based on its orientation and position relative to the target. The performance of the navigation is compared with respect to different figures of merit which resemble possible limitations of resources.

Chapter 5 concentrates on the self-organisation of active Brownian particles by quorum sensing. Quorum sensing denotes the communication method of bacteria by releasing and sensing signalling molecules, which allows them to measure the local population density. When the density exceeds a threshold, a change in the behaviour of a bacterium is triggered. Similarly, in the experimental realisation particles switch between self-propelled and diffusive motion, depending on the local concentration of virtual signalling molecules. This interaction leads to the formations of region with enhanced particle density which are then analysed in detail.

Chapter 6 addresses the collective behaviour of active Brownian particles with alignment interactions that are inspired by the priority of animals to prevent collisions and isolation. In particular, particles try to swim towards the centre of the group, but with a misalignment to either side to avoid the region with highest density. Then, they choose the swimming direction that maximises the alignment with close neighbours. Experimentally, this interaction is realised by active reorientation of the particles, in addition to their active motion. As a result, particles organise in

different collective states, depending on the interaction parameters. The resulting swirls are analysed regarding their robustness to internal and external perturbations and the transition between swirls and swarms is characterised.

Parts of this thesis were already published:

1. Haeufle, D. F. B., Bäuerle, T., Steiner, J., Bremicker, L., Schmitt, S. & Bechinger, C. External control strategies for self-propelled particles: Optimizing navigational efficiency in the presence of limited resources. *Phys. Rev. E* **94**, 012617 (2016).

2. Bäuerle, T., Fischer, A., Speck, T. & Bechinger, C. Self-organization of active particles by quorum sensing rules. *Nat. Commun.* **9**, 3232 (2018).

3. Lavergne, F. A., Wendehenne, H., Bäuerle, T. & Bechinger, C. Group formation and cohesion of active particles with visual perception-dependent motility. *Science* **364**, 70-74 (2019).

4. Bäuerle, T., Löffler, R. C. & Bechinger, C. Formation of stable and responsive collective states in suspensions of active colloids. *Nat. Commun.* **11**, 2547 (2020).

Chapter 1

Collective behaviour in living systems

The concept of group formation is universal in nature and can be observed in living species of all length scales. Such groups consist of many individuals who coordinate their actions and self-organise in various spatio-temporal patterns. This kind of organisation can be crucial for the survival of a species as the coordination of many individuals can imply a significant advantage compared to separated individuals [29]. Important aspects are for example foraging [30], detection and avoidance of predators [31], hunting of prey [32] and reproduction [33]. Some examples of the large variety of group-forming species are shown in Fig. 1.1.

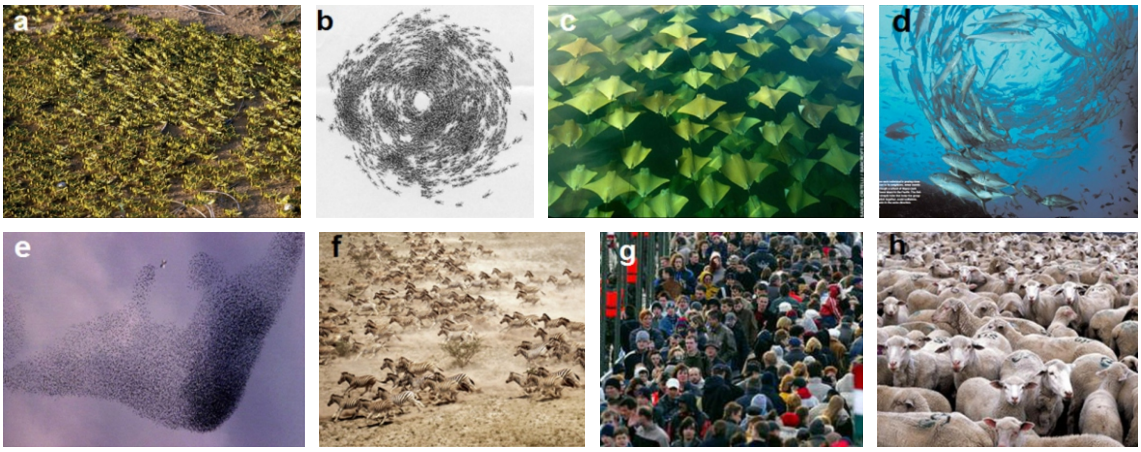

Figure 1.1: Examples of collective behaviour. **a** Marching locusts. **b** Rotating colony of army ants. **c** Array of golden rays. **d** Swirl of fish. **e** Flock of starlings. **f** Herd of zebras. **g** Humans forming traffic lanes. **h** Unordered herd of sheep. Reprinted from [8], Copyright 2012, with permission from Elsevier.

Although the properties of different species and their emerging collective states differ strongly, the principle of self-organisation is identical: rather simple interactions between individuals lead to complex group behaviour [7]. In contrast to inanimate systems which interact by physical forces, living individuals decide their behaviour as a response to so-called social forces [7]. This concept describes the decision-making according to a behavioural policy based on information about their

neighbours, external stimuli and also individual preferences. Individuals retrieve the relevant information using various means of communication, e.g. chemical signalling (bacteria [34], ants [35]), acoustic signalling (midges [33]) or visual perception (birds [36], fish [37]). According to the result of their decision, the individuals then adjust direction and velocity of their motion.

1.1 Collective states

Social interactions between individuals lead to a large variety of different emerging patterns and formations. Three of these collective states are observed particularly often: swarms, flocks and swirls (Fig. 1.2). The terminology for these collective states is not fully consistent in the literature and e.g. swirls are often referred to as mills, vortices or tori [38]. To distinguish between states, the alignment of the members of the group is considered.

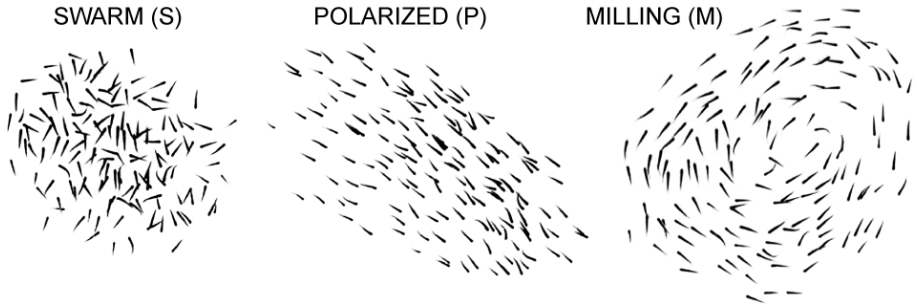

Figure 1.2: Collective states. Snapshots of 150 fish in a swarm state, polarised (flock) state and milling (swirl) state. Reprinted from [39].

Swarms are cohesive groups without global alignment and hence have nearly no centre of mass motion. Often this state is observed in insects [33,40,41], but it is also found in fish [39]. Typically, swarms form when social interactions are dominated by cohesion and the alignment with neighbours has low priority for individuals. Although swarms have no global order, locally strong correlations between individuals can be present confirming that the swarm is a result of interactions between individuals rather than the attraction to a fixed external landmark [33].

Flocks are collective states where most or all members of a group are aligned and move in the same direction. Thus, the group shows a strong centre of mass motion. Because flocks are strongly ordered, collisions are drastically reduced compared to swarms and the average velocity of individuals is higher [39]. Flocks are the dominant form of collective motion in birds [36, 42], but they are also observed in fish [10, 39] and insects [43]. To achieve global alignment, i.e. a high polarisation of the group, the interaction between individuals is typically dominated by the preference to align with their neighbours.

Swirls are groups in which all individuals rotate around their common centre of mass. Because swirls have no global alignment, similar to swarms they have nearly no centre of mass motion. However, locally individuals are highly ordered and therefore swirls share many features with flocks, e.g. the high velocity of individuals [39]. Swirls are mainly observed in fish [10,39], but also in bats [44] or bacteria [34]. Typically, the formation of swirls requires a sensitive balance between attractive and aligning contributions to the interaction between individuals.

1.2 Modelling of collective behaviour

The experimental investigation of collective behaviour in living systems is often difficult to achieve. On one side, it can be technically challenging to keep sufficiently large groups in captivity without influencing their natural behaviour, e.g. when a group of fish interacts with the boundary of the tank [39]. On the other side, to obtain empirical data from wild animals, the conditions one wants to investigate need to be available. In addition, a controlled manipulation of the interactions between individuals is typically not feasible and often it is unclear which aspects are relevant and how they affect the properties of a group [7, 11]. For such reasons, modelling of the interactions in living animals is important to gain insights about the underlying mechanisms of self-organisation.

Different theoretical models have been proposed to reproduce and explain the emergence of collective states. Because of the incredible variety of systems and corresponding models, only two kinds of models will be discussed here: models based on the Vicsek model [45] and zonal models [9, 46, 47]. Although the Vicsek model lacks important features, which are known to be important for animals, its simplicity and the resulting collective motion make this model relevant for the investigation of collective motion [7, 8]. In contrast, zonal models are specifically designed to describe the collective behaviour of animals based on realistic assumptions of their response to neighbours [9].

1.2.1 Vicsek model

The Vicsek model is the simplest and probably most well-known model leading to collective motion of self-propelled particles. In its original form, published in [45], point-like particles with constant velocity are considered, which align with particles in their surroundings. In each simulation step, the orientation of particles is updated to be the mean orientations of their neighbours within an interaction radius, plus additional noise to account for an imperfect steering mechanism. Despite its simplicity, the model leads to a phase transition from an unordered to an ordered state in which the orientations of all particles are aligned. When just considering their order, these states resemble swarms and flocks as discussed above. However, they are not cohesive because the Vicsek model does not include attraction between

particles. Obviously, the lack of cohesion (and also avoidance of collisions) limits the applicability to the collective behaviour of animals [7].

Nevertheless, the Vicsek model is central for the theoretical investigation of collective motion because its simplicity allows a detailed analysis with techniques from statistical physics [48]. In particular, the observed phase transition is of large interest. In the original publication [45], it was assumed that the phase transition is continuous, i.e. second order. This conclusion was based on two arguments: (i) the smooth change of the order parameter (the polarisation) when noise strength or density are varied, and (ii) the dependence of the transition on the system size. Closer investigations, however, suggest that the transition is discontinuous, i.e. first order. In simulations with larger system sizes, it was found that the probability distribution of the polarisation is bimodal and changes discontinuously [49]. Therefore, it is argued that the apparent continuity of the phase transition is due to strong finite-size effects [49, 50].

In addition to its relevance for statistical physics, the Vicsek model can also be used to describe some phenomena in living systems, at least with some modifications. For example, the phase transition in marching locusts in a ring-shaped arena is in agreement with the Vicsek model in one dimension when a weighting of the particle's own orientation is introduced [43]. Furthermore, a more complex adaptation of the model, namely adding hard-core repulsion and chemo-attractive interactions, allows to reproduce the swirling behaviour of bacteria [34].

1.2.2 Zonal models

Zonal models provide a more sophisticated approach to model the collective behaviour in animals, especially fish [9, 46, 47]. In these models, the social interaction between individuals is considered as a combination of repulsion, alignment and attraction. Repulsion corresponds to individuals trying to avoid a collision when distances become too small, alignment with neighbours enhances local order and hence reduces the number of collision, and attraction prevents individuals from becoming isolated.

The details of these contributions vary between the different models, however, the principle is the same. Each individual senses its neighbours in concentric zones with different radii and, depending on the zone, the presence of a neighbour triggers a different response. Because some features of the social interaction presented in Chapter 6 are inspired by the zonal model introduced by Couzin et al. [9], the following considerations concentrate on this model.

In Fig. 1.3 the sensory zones of an individual are sketched. Depending on the distance to its neighbours, an individual recognises them in three different non-overlapping zones: the zone of repulsion (zor), the zone of orientation (zoo) and the zone of attraction (zoa). To account for the restricted vision of animals, a blind region in the back of the individual is excluded from the zones. Using the information about neighbours in these zones, the (supposed) direction of motion $\mathbf{d}$

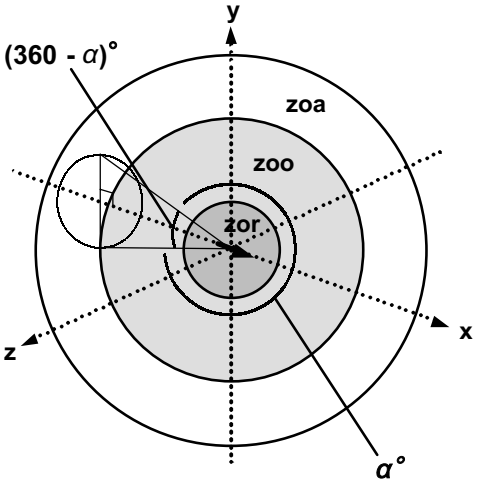

Figure 1.3: Sketch of a zonal model. An individual senses neighbours in three zones: zone of repulsion (zor), zone of orientation (zoo) and zone of attraction (zoa). Opposite to its orientation, a blind region is considered. Reprinted from [9], Copyright 2002, with permission from Elsevier.

is determined. Considering individual i, which perceives n_r, n_o and n_a neighbours in the zor, zoo and zoa, respectively, the different contributions are given by

$$\text{Zone of repulsion (zor)} \qquad \mathbf{d}_\mathrm{r} = -\sum_{i \neq j}^{n_\mathrm{r}} \frac{\mathbf{r}_{ij}}{|\mathbf{r}_{ij}|}, \tag{1.1}$$

$$\text{Zone of orientation (zoo)} \qquad \mathbf{d}_\mathrm{o} = \sum_{j=1}^{n_\mathrm{o}} \frac{\mathbf{v}_j}{|\mathbf{v}_j|}, \tag{1.2}$$

$$\text{Zone of attraction (zoa)} \qquad \mathbf{d}_\mathrm{a} = \sum_{i \neq j}^{n_\mathrm{a}} \frac{\mathbf{r}_{ij}}{|\mathbf{r}_{ij}|}, \tag{1.3}$$

with $\mathbf{r}_{ij}$ the vector from i to j, and $\mathbf{v}_j$ the velocity vector of j. The avoidance of collisions has highest priority and therefore $\mathbf{d} = \mathbf{d}_\mathrm{r}$ when at least one neighbour is located within the zor. Otherwise, $\mathbf{d} = 1/2\,(\mathbf{d}_\mathrm{o} + \mathbf{d}_\mathrm{a})$ when zoo and zoa are populated, or $\mathbf{d} = \mathbf{d}_\mathrm{o}$ ($\mathbf{d} = \mathbf{d}_\mathrm{a}$) if neighbours are only detected in the zoo (zoa). It is important to note that $\mathbf{d}_\mathrm{o}$ and $\mathbf{d}_\mathrm{a}$ are not unit vectors, but their length can take values $0 \leq |\mathbf{d}_\mathrm{o}| \leq n_\mathrm{o}$ and $0 \leq |\mathbf{d}_\mathrm{a}| \leq n_\mathrm{a}$. Accordingly, the weight of the zones varies both with the number of individuals and how well neighbours are aligned (zoo) and evenly distributed (zoa). As a consequence, $\mathbf{d}$ can change drastically when neighbours change zones. To account for errors in sensing and motion of animals, the resulting direction $\mathbf{d}$ is rotated by a random, Gaussian distributed angle. In this model, individuals reorient towards $\mathbf{d}$ with a finite rotation rate, in contrast to the Vicsek model that assumes instantaneous reorientation.

Although the model is still rather simple and does not capture the details of the decision-making of animals, it can, in principal, reproduce swarms, flocks and swirls. Depending on the widths of the different zones, sharp transitions between the different states can be observed [9]. This demonstrates that minor changes of the individuals' response can drastically change the property of the group [7]. In [39] it was shown that this simple model is able to reproduce the experimental

observations in groups of fish. Adding an additional parameter for the weighting of zoo and zoa, the model gains additional flexibility and the transition between states can be triggered by a change of the weighting [51]. Such change of the interaction is expected to happen in case of predator attacks [51]. Additional complexity in the geometry of the zones, i.e. overlapping zones with different blind regions for each zone, can also change the shape of the emerging collective states [52].

1.3 Phase transitions and criticality

Some animal species typically form only one type of collective state, e.g. midges form swarms [33, 40, 41] and birds form flocks [36, 42]. However, in other species different collective states and transitions between these can be observed. For example, locusts show a transition from unordered to ordered motion when the density of individuals exceeds a threshold [43]. Another particularly relevant example for the occurrence of different states is the collective behaviour of fish. In [39] it was shown that the same group of fish forms swarms, flocks and swirls and frequently switches between these states. The probability to find the group in a certain state, however, changes with the number of fish in the group. Remarkably, the observed multistability can be modelled with the zonal model discussed above [39]. In addition, numerical simulations of a more complex model, derived from experimental data of small groups of fish [13], also leads to swarms, flocks and swirls, depending on the interaction parameters and the group size [10]. Near to the transition between flocks and swirls, a high susceptibility of the group is observed [53]. Importantly, this model also shows multistability close to the transition.

Although the above examples indicate that the corresponding phase transitions are first order, it is expected that collective states in animals typically exist close to a critical point [54, 55], which is a feature of a second-order phase transition. This assumption is motivated by the requirement of groups to be both robust against noise, but also responsive to external stimuli, e.g. a predator [55]. In various biological systems evidence for near-criticality was found[1], including the collective behaviour of animals. An outstanding example is the coordinated transport of food in groups of ants which can be modelled by a fully connected Ising model [56, 57]. Furthermore, the collective motion of animals has been shown to be close to criticality. In midges [58, 59] and starlings [42] correlations of the velocity fluctuations largely exceed the interaction range of individuals.

Despite the clear indications for the vicinity of a critical point in some specific cases, continuous phase transitions between different collective states are not observed in experiments as this would require a systematic variation of interaction parameters and, thus, full control over the complex decision-making process in living animals.

[1] See [55] for examples.

Chapter 2

Active Brownian motion

The diffusive motion of micron- or nano-sized colloidal particles in a liquid is called Brownian motion, named after the biologist Robert Brown who discovered this phenomenon in 1827 [60]. Brownian motion is caused by the random forces acting on the particles when they collide with solvent molecules. If, in addition to their random motion, particles can convert energy from their surroundings into directed motion, they are active or self-propelled. The motion resulting from the combination of both effects is called active Brownian motion.

Self-propulsion at these length scales is substantially different from the motion of large objects because inertial effects become negligible [61]. The relevance of inertia can be measured by the Reynolds number Re which compares inertial and drag forces acting on moving objects. In a liquid, the hydrodynamic properties of such objects are described by the incompressible Navier-Stokes equation which becomes time-independent when inertial terms can be neglected for $Re \ll 1$. As a consequence, reciprocal motion cannot lead to propulsion at low Reynolds number. This concept is expressed in Purcell's scallop theorem [61]: a scallop, which just opens and closes its shell with different speed, cannot move in a low Reynolds number regime. Accordingly, the propulsion mechanism of micro-organisms or synthetic microswimmers needs to be irreversible in time. This can, for example, be realised by a periodic corkscrew-like motion or beating of a flexible oar [61].

Self-propulsion at low Reynolds number can be found in various biological systems, such as bacteria [62, 63], spermatozoa [64] and algae [65]. Although other propulsion mechanisms exist, most organisms propel by the rotation of flagella or the beating of cilia [63, 66]. The ability to self-propel allows the organisms a faster exploration of their surroundings when searching for regions with favourable living conditions. In some species the search mechanism is also improved by performing tactic motion, e.g. chemotaxis in bacteria to swim towards higher nutrient concentrations [62] or escape from repellents [67], or phototaxis in algae [68]. The active Brownian motion of living organisms is often a so-called run and tumble motion, where the propulsion is interrupted by phases of active reorientation [69]. This swimming behaviour is different from the typical motion of synthetic active Brownian particles which are constantly moving and reorient due to rotational diffusion (see below).

As active Brownian particles are intrinsically far from equilibrium, they allow

to gain insights on the statistical physics of non-equilibrium systems [70]. In addition, active Brownian motion has the potential for direct applications, e.g. sorting or transport of particles [71, 72], self-assembly of structures [73] or applications in biomedicine [74–76]. Furthermore, as I will show in the following chapters, the accessibility and controllability of active Brownian particles in experiments allows the use as a model system for the investigation of collective phenomena.

2.1 Synthetic active Brownian particles

In order to imitate the swimming behaviour of living organisms, many different kinds of synthetic microswimmers have been developed. These microswimmers can be divided into two groups: externally driven and self-propelled. Externally driven microswimmers are powered by an external field and their velocity and, more importantly, direction of motion are determined by this external field. Often these swimmers are inspired by the propulsion of living organisms, e.g. flexible magnetic filaments resembling the beating motion of spermatozoa [77] or helical rotors resembling the cork-screw motion of bacterial flagella (Fig. 2.1) [78, 79]. This kind of swimmer is useful in tasks that require directed motion, however, they lack the typical aspects of active Brownian motion.

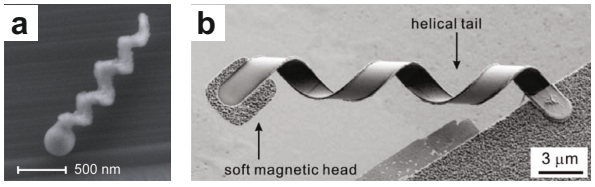

Figure 2.1: Biological inspired microswimmers. **a** Glass propeller with ferromagnetic coating. Reprinted with permission from [78]. **b** Helical ribbon with magnetic head. Reprinted with permission from [79]. Both Copyright 2009 American Chemical Society.

Contrary to externally driven swimmers, the swimming direction of self-propelled microswimmers is determined by the particle itself, rather than being imposed from the outside[1]. Accordingly, the direction changes due to rotational Brownian diffusion and hence these swimmers are referred to as active Brownian particles (AP). In order to move, an AP needs to break the symmetry of its surroundings such, that a directed force acts on the particle. Because gradients of the chemical or physical properties of the surrounding medium lead to directed motion of a particle by phoretic transport [80], self-propulsion can, for example, be realised when the AP locally generates such a gradient. The necessary asymmetry of the AP can be introduced e.g. by the shape of the particle, the use of different materials or the chemical functionalisation [25].

Many different realisations of APs self-propel by the catalytic decomposition of hydrogen-peroxide (H_2O_2). The propulsion mechanism of these catalytic swimmers

[1] Although the direction of motion is independent of an external field, the energy needed for self-propulsion may still be delivered by external fields.

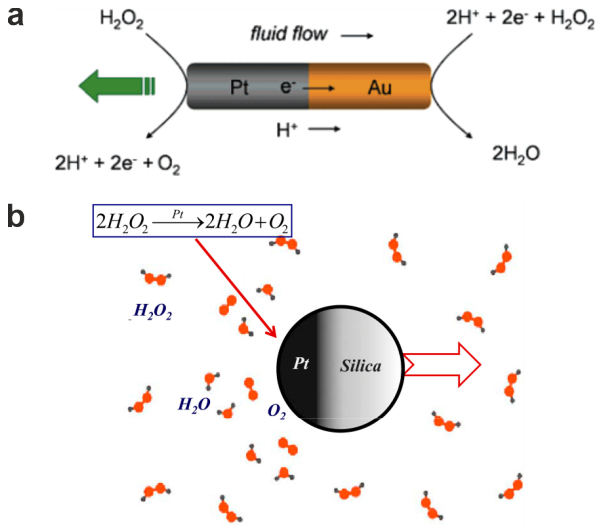

Figure 2.2: Catalytic active Brownian particles. **a** Electro-phoresis of a platinum-gold rod. Reprinted with permission from [81]. Copyright 2006 American Chemical Society. **b** Diffusiuphoresis of a platinum coated silica particle. Reprinted from [82].

depends on the combination of materials as well as their geometry and size. Micron-sized spherical colloids or rods consisting of platinum and gold [24, 83–85] or other metal combinations [86] propel by self-electrophoresis due to the flux of electrons and protons in the redox-reaction (Fig. 2.2a). When the catalytic reaction happens only on a single material, e.g. in the case of silica colloids with a platinum coated hemisphere [87, 88] or a light-activated hematite cube [27], the resulting concentration gradient leads to self-diffusiophoresis (Fig. 2.2b). Besides, for sufficiently large particles the decomposition of H_2O_2 can produce oxygen bubbles that propel the particle [82, 89, 90]. Catalytic self-propulsion has also been reported in a biocompatible system based on the enzymatic decomposition of urea [91]. Another possibility to produce a gradient is the asymmetric heating of a particle which leads to self-thermophoretic propulsion. This can be realised when a transparent particle, e.g. made from silica, is coated with a light-absorbing material on one hemisphere and illuminated with a laser beam [92] or when a homogeneously light absorbing particle is asymmetrically illuminated with a focused laser beam [93]. In the latter case, however, the particle is not only moving due to self-thermophoresis but also experiences optical forces [28].

Asymmetric heating also leads to self-propulsion when APs are suspended in a binary liquid which is kept at a temperature close to its lower critical point. This propulsion mechanism is used in the presented experiments and explained in detail in Section 3.1.1. Here it should only be noted that, compared to thermophoresis, significantly lower illumination intensities are required to induce self-propulsion and hence optical forces are negligible.

In addition, self-propulsion can also be achieved by spontaneous symmetry breaking. This is the case e.g. in droplets propelled by Marangoni flows [94–96], Quincke rollers [97, 98] or ferromagnetic rollers [99, 100]. In these systems, the swimmers are symmetric, but active motion is initiated due to fluctuations. The motion then

breaks the symmetry and the self-propulsion is stabilised.

Considering the implementation of controllable interactions between APs, the most important feature of a propulsion mechanism is the possibility to adjust swimming velocities independently. Therefore, the majority of available experimental systems cannot be used for this application. In particular, only light-activated systems (catalytic diffusiophoresis [27], thermophoresis [93] and demixing of a binary liquid) allow to address APs individually. Because the maximum duration of measurements is limited when fuel is consumed in a catalytic process and because optical forces should be avoided, the self-propulsion of a binary mixture is the best choice for the experiments in this thesis.

2.2 Properties of active Brownian motion

2.2.1 Brownian motion

In order to characterise active Brownian motion, first the case of Brownian motion is considered, i.e. without activity of the particle. The mathematical description of this scenario can be found in textbooks, e.g. [101]. The probability $\rho = \rho(\mathbf{r}, t)$ to find a particle at position $\mathbf{r}$ and time t follows the diffusion equation

$$\frac{\partial \rho}{\partial t} = D_\mathrm{T}\, \Delta \rho, \tag{2.1}$$

with the (translational) diffusion constant D_T. For starting condition $\mathbf{r}(t = 0) = 0$ the solution is

$$\rho(\mathbf{r}, t) = \frac{1}{(4\pi\, D_\mathrm{T}\, t)^{d/2}} \exp\left(-\frac{|\mathbf{r}|^2}{4\, D_\mathrm{T}\, t}\right), \tag{2.2}$$

where d is the dimensionality of the motion. For a spherical particle the translational diffusion coefficient is given by the Stokes-Einstein relation

$$D_\mathrm{T} = \frac{k_\mathrm{B} T}{6\pi\eta R}. \tag{2.3}$$

Here, k_B is the Boltzmann constant, T the absolute temperature, η the viscosity of the liquid and R the radius of the particle.

The translational dynamics of a particle in a liquid can be described by the Langevin equation which is based on Newton's laws. Considering the friction coefficient $\gamma = 6\pi\eta R = k_\mathrm{B} T / D_\mathrm{T}$, it reads

$$m \frac{d^2 \mathbf{r}}{dt^2} = -\gamma \frac{d\mathbf{r}}{dt} + \boldsymbol{\xi}_\mathrm{T}, \tag{2.4}$$

with mass m of the particle and a Gaussian distributed stochastic force $\boldsymbol{\xi}_\mathrm{T}$ characterised by

$$\langle \boldsymbol{\xi}_\mathrm{T} \rangle = 0, \tag{2.5}$$

$$\langle \xi_\mathrm{T}^i(t) \xi_\mathrm{T}^j(t') \rangle = \frac{2(k_\mathrm{B}T)^2}{D_\mathrm{T}} \, \delta_{ij} \, \delta(t-t'), \tag{2.6}$$

with i and j corresponding to different the different components of the vector. At low Reynolds number, inertia can be neglected and the approximation $m\frac{d^2\mathbf{r}}{dt^2} \approx 0$ simplifies Eq. (2.4) to the overdamped Langevin equation

$$\frac{\mathrm{d}\mathbf{r}}{\mathrm{d}t} = \frac{D_\mathrm{T}}{k_\mathrm{B}T} \, \boldsymbol{\xi}_\mathrm{T}. \tag{2.7}$$

Due to the stochastic force, the equation cannot be solved exactly, however, statistical properties can be derived. The mean-squared-displacement (MSD) given by

$$\langle \Delta \mathbf{r}^2 \rangle = \langle |\mathbf{r}(t_0 + t) - \mathbf{r}(t_0)|^2 \rangle_{t_0} = 2d \, D_\mathrm{T} \, t \tag{2.8}$$

is particularly important as it can be easily obtained from experimentally measured particle trajectories.

Analogue to the position $\mathbf{r}$, also the orientation $\hat{\mathbf{u}}$ of a Brownian particle is subjected to diffusion, with rotational diffusion constant

$$D_\mathrm{R} = \frac{k_\mathrm{B}T}{8\pi\eta R^3}. \tag{2.9}$$

Considering a single rotation axis, the orientation $\hat{\mathbf{u}} = (\cos(\theta), \sin(\theta))$ of the particle is fixed to a plane and described by a single angle θ. The corresponding equation of motion is then given by

$$\frac{d\theta}{dt} = \frac{D_\mathrm{R}}{k_\mathrm{B}T} \, \xi_\mathrm{R}. \tag{2.10}$$

ξ_R is a Gaussian distributed stochastic torque with zero mean, $\langle \xi_\mathrm{R} \rangle = 0$, and variance $\langle \xi_\mathrm{R}(t) \xi_\mathrm{R}(t') \rangle = 2(k_\mathrm{B}T)^2 / D_\mathrm{R} \, \delta(t-t')$. If the particle rotates freely in space, its orientation is described by two independent angles which both follow Eq. (2.10).

2.2.2 Active Brownian motion

Self-propulsion of the particle with velocity v causes an additional directed force

$$F = \frac{k_\mathrm{B}T}{D_\mathrm{T}} \, v \tag{2.11}$$

in Eq. (2.7) which is aligned with the particle orientation $\hat{\mathbf{u}}$. In general, APs can freely move and rotate in 3D, however, here the typical experimental conditions are considered in which APs only move in the x-y-plane and their orientation is

parallel to it. The corresponding overdamped equations of motion for position $\mathbf{r}$ and orientation $\hat{\mathbf{u}} = (\cos(\theta), \sin(\theta))$ of the particle become coupled and are given by

$$\frac{d\mathbf{r}}{dt} = \frac{D_\mathrm{T}}{k_\mathrm{B}T}\left(F\hat{\mathbf{u}} + \boldsymbol{\xi}_\mathrm{T}\right), \tag{2.12}$$

$$\frac{d\theta}{dt} = \frac{D_\mathrm{R}}{k_\mathrm{B}T}\ \xi_\mathrm{R}. \tag{2.13}$$

The MSD can be calculated analytically [102] to be

$$\langle \Delta\mathbf{r}^2 \rangle = \left(4D_\mathrm{T} + 2v^2\tau\right)t + 2v^2\tau^2\left(\exp\left(-t/\tau\right) - 1\right), \tag{2.14}$$

with the reorientation time $\tau = 1/D_\mathrm{R}$. For small $t \ll \tau$, this equation is approximated[2] by

$$\langle \Delta\mathbf{r}^2 \rangle = 4D_\mathrm{T}t + v^2t^2. \tag{2.15}$$

At such short times the motion of the particle is a combination of its ballistic self-propulsion and diffusive motion. At large times $t \gg \tau$, the MSD is approximated by

$$\langle \Delta\mathbf{r}^2 \rangle = \left(4D_\mathrm{T} + 2v^2\tau\right)t \tag{2.16}$$

which resembles diffusive motion, but with an enhanced effective diffusion constant $D_\mathrm{eff} = D_\mathrm{T} + v^2\tau/2$. This is because the directed self-propelled motion gets randomised by rotational diffusion. Before this happens an AP typically swims a distance called the persistence length $L = v\tau$. To determine the swimming velocity v and reorientation time τ in experiments, the MSD is calculated from the measured trajectories.

2.3 Collective phenomena of active Brownian particles

Even without the addition of programmable interactions between APs, various collective phenomena can be observed. Depending on the experimental system, interactions between APs are diverse and include e.g. steric repulsion and phoretic and hydrodynamic interactions. Because of the vast variety of emerging collective effects in active Brownian particles, here only few examples will be discussed.

2.3.1 Phase separation

One of the most remarkable collective effects of active Brownian particles is the spontaneous formation of dense clusters which are surrounded by a dilute gas. This clustering, which is observed in numerical simulations [103, 104] and experiments [27,105,106], is based only on the activity of APs and their (purely repulsive) steric interaction. The formed clusters are highly dynamic and constantly exchange particles with the surrounding gas (Fig. 2.3a).

[2] Series expansion of the exponential function: $\exp(-t/\tau) \approx 1 - t/\tau + t^2/2\tau^2 + \ldots$

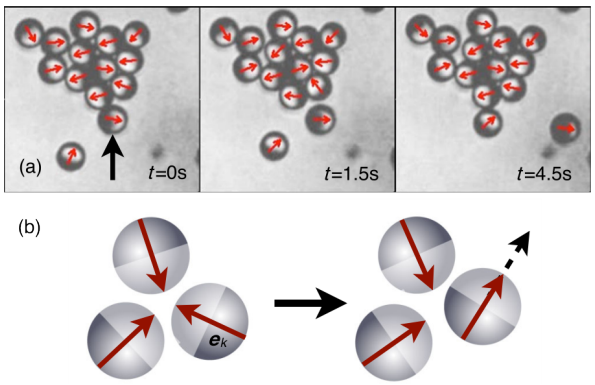

Figure 2.3: Phase separation of APs. **a** Snapshots of a cluster of APs with orientations marked as red arrows. **b** Sketch of the clustering mechanism. Reprinted figure with permission from [106] (dx.doi.org/10.1103/PhysRevLett.110.238301). Copyright 2013 by the American Physical Society.

The mechanism leading to cluster formation can be described as self-blocking. When APs collide, they block themselves and cannot continue to move before reorienting (Fig. 2.3b). Because the orientation of an AP changes only due to rotational diffusion, this will take a time on the order of the reorientation time $\tau = 1/D_{\mathrm{R}}$ [106]. If another AP approaches within this time, the inner particle is no longer able to move, even after reorienting. The balance between such events and the number of APs leaving the cluster (consisting of at least two APs) determines if the cluster will grow or dissolve. While the former only depends on the number of APs at the edge of the cluster, the latter depends on the density of the surrounding gas and the swimming velocity of APs. Accordingly, the formation of clusters is only observed when both parameters are sufficiently large [107].

Theoretical investigations of the cluster formation of active Brownian particles have shown that the transition between a homogeneous gas phase and a phase composed of clusters surrounded by a dilute gas is a second order phase transition [107, 108]. The critical point is defined by a critical swimming velocity and a critical particle density. Correspondingly, a regime exists in which hysteresis occurs and the final state of the system depends whether clusters existed initially [107, 108]. In addition, the phenomenology can also be described in the framework of motility induced phase separation (MIPS) [109]. When the average swimming velocity decreases sufficiently fast as a function of the local particle density, an initially homogeneous particle distribution becomes unstable: fluctuations of the local particle density lead to the accumulation of more particles which results in positive feedback and eventually phase separation.

2.3.2 Collective motion

When interactions between self-propelled particles go beyond steric repulsion, the emerging collective phenomena of self-propelled particles become diverse and strongly depend on the details of the experimental system. Remarkably, the observed collective states can be similar to flocks and swirls as discussed in the previous chapter. In particular, such behaviour can be observed in Quincke rollers [97, 98] or ferromagnetic rollers [99, 100].

Quincke rollers self-propel due to an electrohydrodynamic phenomenon known as Quincke rotation: In presence of a sufficiently strong, constant electric field, insulating particles in a conducting fluid start to rotate because the surface charge distribution of the particle is unstable against fluctuations. As soon as a particle rotates, the electric field leads to an electrostatic torque stabilising the rotation. When particles are close to a wall, the particle rotation leads to directed motion with a velocity that depends on the strength of the electric field. Interactions between the rollers arise from different hydrodynamic effects, both short- and long-ranged, and short-ranged electrostatic repulsion. Interestingly, similar to social forces between animals, these interactions act on the direction of motion. Because the group of rollers is not cohesive, experiments need to be carried out in a confinement whose geometry defines the properties of the resulting collective motion. In case of a periodic confinement (Fig. 2.4a), a transition from unordered motion to ordered motion in a polar band or a polar liquid is observed upon increasing the particle density [97]. In a circular confinement, the rollers form a vortex (swirl) rotating around an unordered dilute region in the centre (Fig. 2.4b) [98].

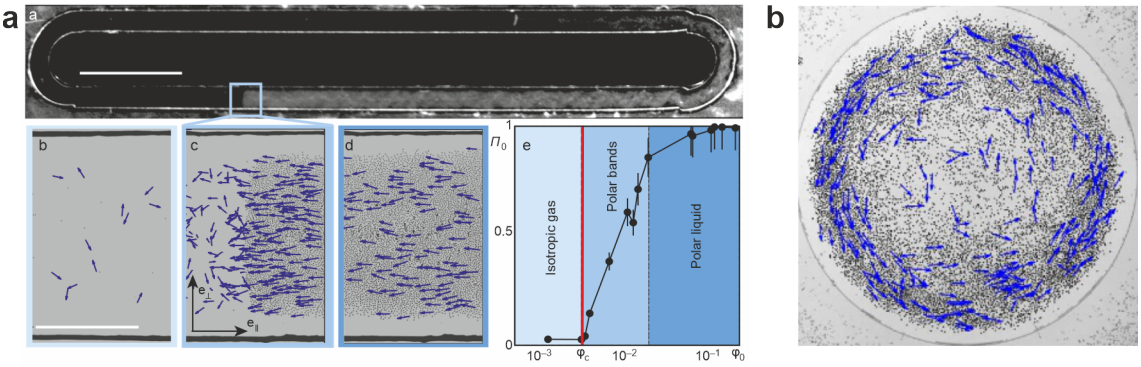

Figure 2.4: Collective behaviour of Quincke rollers. **a** Depending on the particle density, Quincke rollers in a periodic confinement move unordered or ordered, either in a polar band or a polar liquid. Reprinted with permission from Springer Nature, [97], Copyright 2013. **b** Quincke rollers in a circular confinement rotate around an unordered dilute centre. Reprinted from [98].

Similar observations can also be made in ferromagnetic rollers which self-propel in an oscillating, vertical magnetic field as sketched in Fig. 2.5a [99, 100]. Although the propulsion mechanism is seemingly alike the one of Quincke rollers, it relies on inertia [99]. Nevertheless, due to shape imperfections the motion of individual ferromagnetic rollers is similar to the motion of active Brownian particles. In a certain range of the oscillation frequency, the balance between hydrodynamic and magnetic interactions between the rollers leads to the formation of swirls (Fig. 2.5b) [100]. It should be noted that these swirls are only cohesive because the rollers move in a soft gravitational confinement. However, the formation of swirls surrounded by a dilute gas can also be observed without this confinement when the particle density

is sufficiently large.

Despite the similarity of the emerging collective phenomena to collective states observed in animals, the underlying interactions differ strongly. In the systems discussed above, interactions between particles are reciprocal which is often not the case in nature because of a limited sensing capability of the individuals, e.g. due to their field of vision. Besides, the flocks and swirls observed in active particles are not cohesive, which is in contrast to the case of animals, where cohesion is typically one of the main priorities.

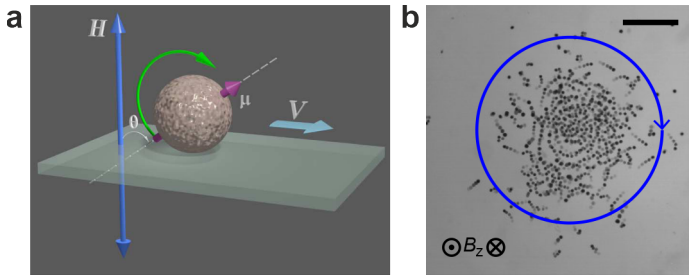

Figure 2.5: Vortex formation of ferromagnetic rollers.
a Sketch of the propulsion mechanism. Reprinted from [99].
b Group of rollers in a clockwise rotating vortex (swirl). Reprinted from [100].

Chapter 3

Experimental system

The implementation of tailored interactions between active Brownian particles (APs) requires precise control over strength and direction of their self-propulsion. The response of each particle needs to be adjusted individually, depending on the configuration of the system, namely the positions and orientations of some or all other particles. The light-activated self-propulsion of active Brownian particles in a binary mixture close to its critical point [110] provides the prerequisites for this individual adjustment of the swimming properties. In this system, the velocity of the swimmers is set by the light intensity and, in addition, they reorient in the presence of a light gradient [72]. Accordingly, the illumination with individual laser beams allows to control the self-propulsion of the particles independently. As active Brownian particles are permanently moving, stable propulsion requires frequent updates of the illumination.

In this chapter I will present the experimental system that allows to implement freely programmable interactions into a system of active Brownian particles. At the beginning I will introduce the propulsion mechanism and the experimental setup that gives the possibility to illuminate particles individually. The main focus of the chapter then lies on the various calibrations which are necessary to achieve consistent and reproducible illumination and propulsion conditions.

3.1 Self-propulsion of active particles

3.1.1 Self-propulsion by local demixing

The mechanism of self-propulsion by local demixing was first presented in 2011 using gold coated Janus particles, i.e. spherical particles with the coating on one hemisphere, in a critical mixture of water and 2,6-lutidine (2,6-dimethylpyridine) [110]. When illuminated with a laser beam, a Janus particle self-propels with the gold coated hemisphere in the back and a propulsion velocity that can be adjusted by the illumination intensity.

Self-propulsion of the APs is achieved by exploiting the phase-behaviour of a binary liquid which can either exist in a homogeneously mixed or in a separated phase. Depending on the (fixed) concentrations, the transition from the mixed to

the separated phase can either be first order (binodal decomposition) or, at the critical point, second order (spinodal decomposition).

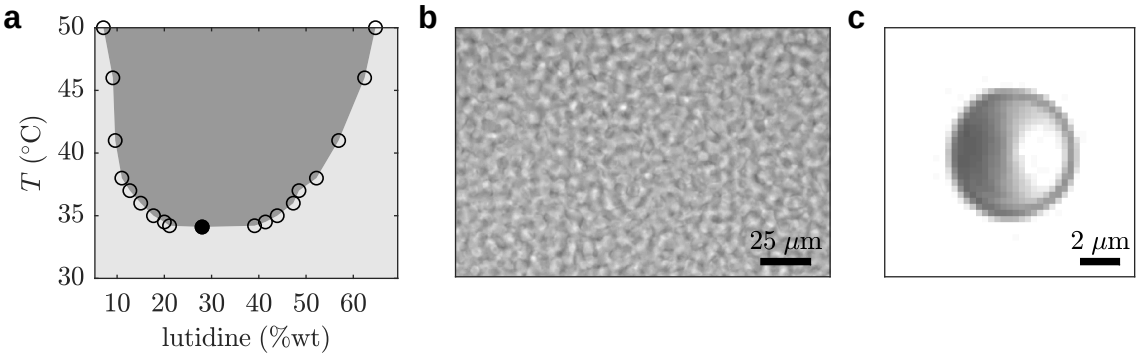

Figure 3.1: Phase behaviour of water/lutidine **a** Phase diagram of water and 2,6-lutidine with lower critical point (filled symbol). Data taken from [111]. **b** Spinodal decomposition of the binary mixture when heated above the critical point. **c** Snapshot of a carbon coated silica Janus particle.

The phase diagram of water/lutidine has an upper critical point at a temperature of $\approx 230°$ C [112] and in addition a lower critical point (LCP) with critical temperature $T_C = 34.1°$ C at a lutidine fraction of $c_L = 28$ %wt (Fig. 3.1a). If a critical composition is heated from $T < T_C$ to $T \gtrsim T_C$, it phase separates by spinodal decomposition (Fig. 3.1b).

When the critical mixture is kept in the mixed phase with a temperature $T < T_C$, selective heating of the particles above T_C induces local demixing. As self-propulsion requires an asymmetry of the demixed zone, Janus particles with a coating of a light-absorbing material on one hemisphere are used (Fig. 3.1c). In early experiments [26, 110] gold was used for the coating and later replaced by carbon to reduce Vander-Waals forces between particles. When particles are illuminated with a highly defocused laser beam of intensity I, light absorption on the coating leads to a heating $\Delta T \propto I$ [113]. The resulting temperature profile has its maximum on the coated surface and decays asymmetrically. If I, and thus ΔT, is large enough to reach the critical temperature T_C, the liquid demixes within the isotherm $T = T_C$.

Body forces acting on the edges of the demixed zone result in self-propulsion whose strength depends non-monotonically on the illumination intensity I [113]. The propulsion direction can be either parallel or anti-parallel to the orientation $\hat{\mathbf{u}}$ of the particle, defined by the vector from the coated to the uncoated surface. Different situations have to be distinguished (see Fig. 3.2):

- $I < I_0$
  A minimum intensity I_0 is necessary to heat the coated surface to the critical temperature T_C of the liquid. If the illumination intensity is smaller than I_0, no demixing and hence no self-propulsion is present.

- $I_0 < I < I_{\mathrm{rev}}$
  If I is sufficient to reach temperatures above T_{C}, a water-poor bubble forms near the coated, hydrophobic surface which results in the propulsion $\mathbf{v} = v\hat{\mathbf{u}}$. As long as the bubble is small, the velocity v increases linearly with I, before it saturates and finally decreases when I approaches the reversal intensity I_{rev}.

- $I > I_{\mathrm{rev}}$
  A second, water-rich droplet forms near the uncoated silica surface whose body forces point in the opposite direction. Accordingly, the propulsion direction is reversed, i.e. $\mathbf{v} = v\,(-\hat{\mathbf{u}})$. When the demixing zone increases further, the two bubbles cover the particle completely and finally all body forces cancel out, so that for $I \to \infty$ no propulsion is present.

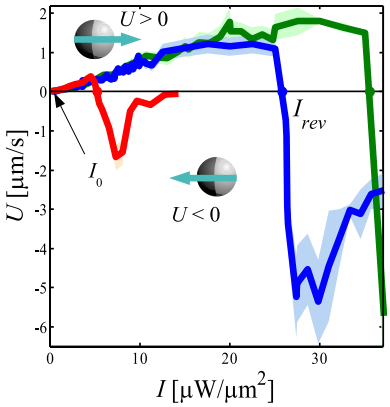

Figure 3.2: Propulsion velocity as a function of the illumination intensity in a binary mixture of water and PnP. For three different AP sizes (decreasing in the order red, blue, green), the intensity dependence of the propulsion is shown. $U > 0$ ($U < 0$) corresponds to the case when the propulsion direction is parallel (anti-parallel) to the AP orientation. Reprinted from [113].

When the illumination intensity is (nearly) constant over the particle, the amount of light absorbed on the coating is independent on the particle orientation $\hat{\mathbf{u}}$. In this case, $\hat{\mathbf{u}}$ is only affected by rotational diffusion which is typically restricted to 2D due to hydrodynamic interactions with the surface of the sample cell [114]. The details of the propulsion mechanism are explained theoretically and experimentally in [115] and [113], the latter in a critical binary mixture of water and PnP (propylene glycol n-propyl ether), which shows a similar behaviour as water/lutidine.

3.1.2 Active reorientation

When exposed to a light gradient ∇I, Janus particles in water/lutidine show active reorientation [72]. Due to the gradient, the absorbed intensity (and hence the heating) is not identical everywhere on the coated hemisphere and the demixing bubble becomes asymmetric. This results in a viscous torque Γ acting on the particle which is given by

$$\Gamma(\gamma) = -\Gamma_{\mathrm{max}} \sin(\gamma), \tag{3.1}$$

where γ is the angle between particle orientation $\hat{\mathbf{u}}$ and the negative direction of the gradient $-\nabla I$, and Γ_{max} is the maximum torque when $\gamma = \pm\pi/2$ and which depends

on the intensity I and the steepness of the gradient $|\nabla I|$. According to Eq. (3.1), APs reorient towards $\gamma = 0$ where the restoring torque vanishes, i.e. $\Gamma(0) = 0$. From the torque, an effective aligning potential

$$V(\gamma) = -\int \Gamma(\gamma)\, d\gamma = -\Gamma_{\max} \cos(\gamma) \tag{3.2}$$

can be defined and due to rotational diffusion of the AP orientation, γ will fluctuate around zero. According to the Boltzmann distribution, the probability for the misalignment γ is then

$$P(\gamma) \propto \exp\left(-\frac{V(\gamma)}{k_{\mathrm{B}}T}\right) = \exp\left(\frac{\Gamma_{\max}\cos(\gamma)}{k_{\mathrm{B}}T}\right). \tag{3.3}$$

3.1.3 Particle and sample preparation

APs are fabricated from silica particles[1] with a diameter of a few micrometres. In a first step, a suspension of particles in water is spread over the surface of a microscope slide and left to dry. It is important to ensure that in the drying process a monolayer of particles has formed, i.e. that no particles sit on top of others. Otherwise not all particles receive the same coating, which makes them unsuitable for experiments. Subsequently, a layer of carbon (depending on the experiment typically between 20 nm and 100 nm) is sputtered perpendicular onto the monolayer. Afterwards, the coated particles are removed from the microscope slide with an ultra-sonic bath and stored in water. Samples are prepared by mixing the correct amount of the coated particles with the binary water/lutidine mixture and filling the suspension into the sample cell[2] with a thickness of 200 µm which is then sealed with *Parafilm* to enhance its lifetime (Fig. 3.3).

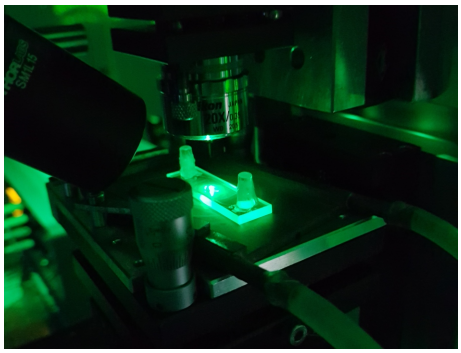

Figure 3.3: Sample cell.

3.2 Experimental setup

The experiments in this thesis require the individual control of the propulsion properties of APs which makes it necessary to be able to address APs with independent laser beams. This individual addressing of APs is realised by changing position and power of a single laser beam with an acousto-optical deflector (AOD). The experimental setup is shown in Fig. 3.4 and described in detail in the following.

[1] Microparticles GmbH
[2] Hellma 137-0.2-40

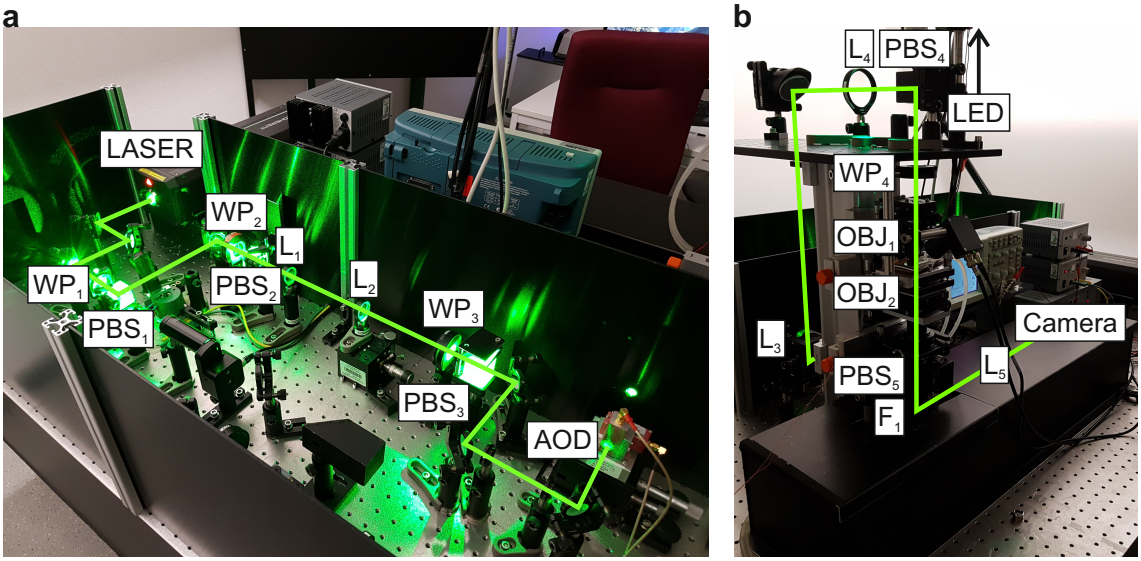

Figure 3.4: Experimental setup. **a** Preparation of the laser beam as optimal input for the AOD. **b** Collection of the deflected laser beams and imaging system.

3.2.1 Laser system

The light source for the illumination of APs is a laser[3] with wavelength $\lambda = 532$ nm, output power $P = 2.2$ W and beam diameter $d = 2.25$ mm. First, the output laser beam is adjusted to optimise performance of the AOD. Using polarising beamsplitter cubes ($\mathrm{PBS}_1, \mathrm{PBS}_2, \mathrm{PBS}_3$) together with $\lambda/2$-waveplates ($\mathrm{WP}_1, \mathrm{WP}_2, \mathrm{WP}_3$), the power is reduced from 2.2 W to approx. 0.1 W, which is sufficient for the experiments. This power reduction is necessary as the laser needs to be operated near its maximum output power, otherwise the shape of the laser beam becomes elliptical. In addition to the power reduction, PBS_3 also adjusts the laser polarisation to the required input of the AOD. The telescope, consisting of lenses L_1 and L_2 with focal lengths $f_{\mathrm{L1}} = 100$ mm and $f_{\mathrm{L2}} = 50$ mm, reduces the size of the laser beam by a factor of two.

3.2.2 Acousto-optical deflector

Function principle

An acousto-optical deflector is a device that exploits the interaction between light and a medium to control position and power of a laser beam. The function principle of an AOD is sketched in Fig. 3.5a.

A travelling acoustic wave is excited in the crystal of the AOD by conversion of a radio-frequency (rf-) input using a piezoelectric-transducer. The wavelength Λ of

[3] Coherent Verdi V2

this acoustic wave is given by

$$\Lambda = \frac{v}{f_{\mathrm{rf}}}, \tag{3.4}$$

with the speed of sound v and frequency f_{rf} of the rf-input, and corresponds to a periodic variation of the refractive index in the crystal. Laser light, with wavelength λ' inside the medium, can be reflected at this wave, when the Bragg condition

$$\sin(\Theta_{\mathrm{B}}) = \frac{\lambda'}{2\Lambda} \tag{3.5}$$

is satisfied. The resulting first-order beam is then deflected by $2\Theta_{\mathrm{B}}$ relative to the undeflected zero-order beam. The power of the first-order beam P_1 depends on the amplitude of the acoustic wave and hence on the power P_{rf} of the rf-input. In the case of small P_{rf}, the power P_0 of the zero-order beam, can be assumed to be unchanged and it follows $P_1 \propto P_{\mathrm{rf}}$. For increasing P_{rf} this assumption is no longer valid and saturation leads to deviations from the linear dependence.

As the Bragg angle Θ_{B} depends on the wavelength Λ of the acoustic wave and therefore on the frequency f_{rf} of the rf-input, the choice of f_{rf} defines the deflection angle Θ of the first-order beam in a range

$$\Theta = 2\Theta_{\mathrm{B}} \pm \Delta\Theta, \tag{3.6}$$

corresponding to a frequency range $f_{\mathrm{min}} \leq f_{\mathrm{rf}} \leq f_{\mathrm{max}}$. In the ideal case, the Bragg condition is only satisfied for one frequency, however, this issue can be technically solved, e.g. by using an anisotropic crystal or (slightly) diverging acoustic waves. Further details about the theoretical background of AODs can be found for example in [116].

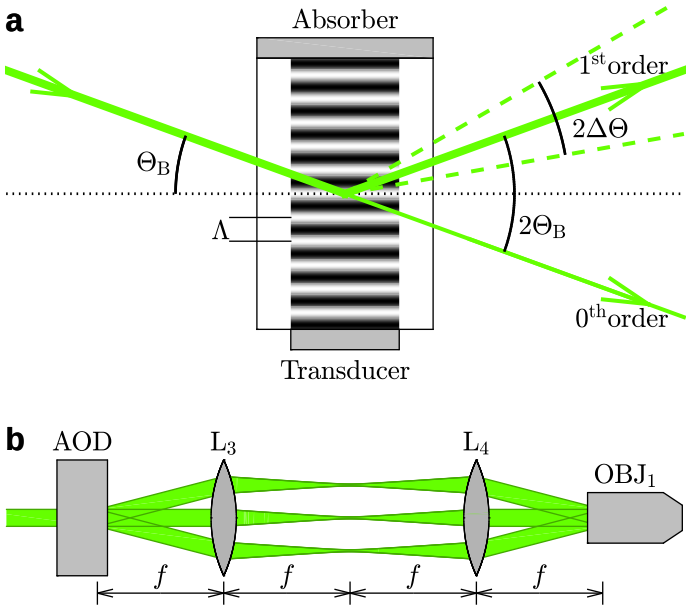

Figure 3.5: Beam steering with an acousto-optical deflector.
a Function principle of an AOD. Laser light enters the crystal with Bragg angle Θ_{B} and is partly diffracted by $2\Theta_{\mathrm{B}}$ (1^{st} order) and partly passes the crystal unaltered (0^{th} order).
b Sketch of a telecentric $4f$-telescope. A set of beams leaving the AOD in different directions is collected and then directed to the objective OBJ_1.

Application in the experimental setup

The AOD in the experimental setup is a 2-axis deflector[4] with anisotropic TeO_2 (tellurium dioxide) crystals. This model is optimised for a large range of deflection angles which is important to be able to address APs within the whole field of view.

As the distance of beams leaving the AOD in different angles is continuously increasing, a telecentric $4f$-telescope is used to direct the beams towards an objective which focuses them into the sample cell (Fig. 3.5b). Lens L_3 is placed at a distance f from the AOD and gathers the beams leaving the AOD at angle $-\Delta\Theta \leq \theta \leq \Delta\Theta$ with respect to the angle of the central beam. Between L_3 and L_4, beams propagate parallel, i.e. $\theta' = 0$, and distance $d = f \sin(\theta)$, before L_4 changes their direction to $\theta'' = -\theta$. At the objective (OBJ_1), all beams have the same position and differ only in their propagation direction. Accordingly, this optical path relates each (two-dimensional) deflection angle to a certain position in the sample cell. As L_3 also focuses the individual beams, a spacing of $2f$ between the lenses is necessary to re-collimate the beams.

Driving protocol

As the AOD deflects the laser beam only to one position at a time, APs cannot be illuminated simultaneously. Instead, the laser needs to be sent to each AP subsequently in a repeating cycle. This procedure implies two time scales which are relevant for the application of the AOD.

Switching between positions: When the position of the laser beam and therefore the frequency of the rf-input is changed, the new acoustic wave needs to travel through the crystal to replace the original wave. As long as both wavelengths are present at the region covered by the laser beam, it is not only deflected to the intended positions $(x_{\text{old}}, y_{\text{old}})$ and $(x_{\text{new}}, y_{\text{new}})$, but also to the combinations $(x_{\text{old}}, y_{\text{new}})$ and $(x_{\text{new}}, y_{\text{old}})$. Accordingly, these unintended traps can be suppressed when the rf-signal is interrupted for a delay time $t_{\text{delay}} \geq 2w/v$, with w the waist of the laser beam and v the sound velocity in the AOD crystal. For the experimental conditions, it follows $t_{\text{delay}} \geq 1.7$ µs.

Repetition of the cycle: In order to achieve stable self-propulsion of APs, the illumination should be quasi-static and therefore the time interval t_{rep} between two consecutive illumination periods as small as possible. In particular, it is important that t_{rep} is smaller than the typical time scale of the phase-separation kinetics of the binary water/lutidine mixture. From the inter-diffusion coefficient $D \sim 1.5 - 3 \cdot 10^{-10}$ m^2/s [117] at the experimental temperatures and the particle radius R, this time scale can be estimated by R^2/D [113] to be $\sim 15 - 70$ ms.

[4] AA Opto-Electronic DTSXY-400-532

Combining these consideration, in the experiments the rf-input is always active for 8 µs followed by an interruption $t_{\text{delay}} = 2$ µs. The number of different positions is limited to at most 400 which results in $t_{\text{rep}} = 4$ µs as shown in Fig. 3.6.

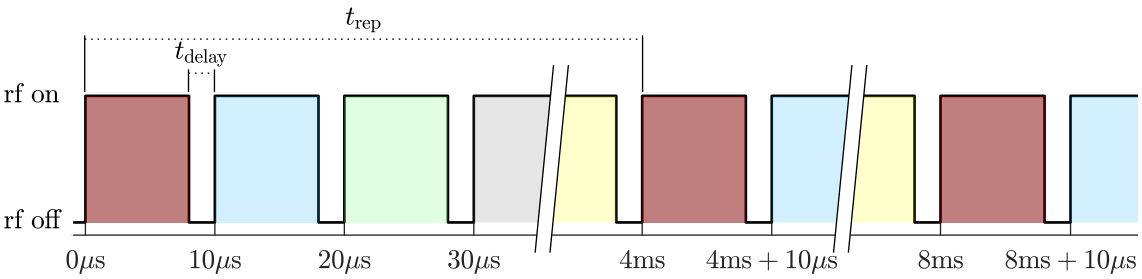

Figure 3.6: Sketch of the driving protocol. At most 400 different APs can be addressed (corresponding to different colours) which results in a repetition time $t_{\text{rep}} = 4$ ms when each AP is illuminated for 8 µs with a delay of $t_{\text{delay}} = 2$ µs between consecutive APs.

3.2.3 Imaging system

APs are imaged using a custom-built video microscopy system (Fig. 3.4b). The light source for the imaging is a green LED in *Köhler*-configuration [118], which provides a homogeneous illumination intensity in the sample plane. In order to reduce deviations between the optical path of LED and laser light, the colour of the LED is chosen to be as close as possible to the laser wavelength. An infinity corrected objective[5] (OBJ_2) in combination with an achromatic lens (L_5) with 180 mm focal length projects the sample plane to a cmos camera[6] with a resolution of 1280×1024 and a pixel size of 6.7 µm. The magnification of the imaging system was measured to be 21.3.

Using polarising beamsplitter cubes ($\text{PBS}_4, \text{PBS}_5$) and an interference filter (F_1), the laser light is filtered out. When replacing F_1 with a coloured glass filter, the laser light can also be imaged on the camera.

3.3 Illumination of individual particles

3.3.1 Calibration procedures

The illumination of APs with individual laser beams requires the precise control over the position and intensity of each laser beam. In the following the different calibrations which are necessary to ensure reproducible and well-defined illumination conditions are presented.

[5] Zeiss LD Plan-Neofluar 20x/0.4 Korr M27
[6] Pixelink PLB741-U

Frequency calibration

Initially, the frequency $f_{\mathrm{rf}} = (f_x, f_y)$ of the radio-frequency (rf-) input is set to the centre frequency f_{AOD} of the AOD and the optical path is adjusted so that the laser beam is centred on the camera. For the calibration, nine beams are placed on a grid with spacing Δf_x and Δf_y around f_{AOD}. Δf_x and Δf_y are chosen to be as large as possible while the beams still remain visible on the camera. The position of each beam (x, y) is found by a two-dimensional Gaussian fit to a microscopy image of the beam. A set of parameters A and f_0 is determined for the conversion between position and frequency according to

$$\begin{pmatrix} f_x \\ f_y \end{pmatrix} = \begin{pmatrix} A_x & A_{xy} \\ A_{yx} & A_y \end{pmatrix} \cdot \begin{pmatrix} x \\ y \end{pmatrix} + \begin{pmatrix} f_{0,x} \\ f_{0,y} \end{pmatrix} \tag{3.7}$$

using the least squares method. The parameters $A_{xy} \approx A_{yx} \approx 0$ indicate the rotation of the imaging relative to the diffraction directions of the AOD and should be zero in the ideal case. This calibration is used to calculate the correct frequencies to send to the AOD, based on the supposed position of the laser beam. Further calibrations of the beam position only act as a change of these supposed positions, but not on the conversion between position and frequency.

Flatfield calibration

In order to provide a position-independent and controllable strength of the diffracted laser beams, the diffraction efficiency of the AOD, with respect to the frequency and the power of the rf-input, needs to be mapped and adjusted. For this calibration, the sample cell is replaced by a photodiode which generates a voltage U proportional to the power of the incident laser light.

The first part of the calibration treats the non-linear dependence of the diffraction efficiency on the power of the rf-input P_{rf}. For a grid of 9 positions (x, y), corresponding to the centre and edges of the experimental field of view, and 20 equidistant values $0 \leq P_{\mathrm{rf}} \leq P_{\mathrm{rf,max}} = 250$ mW, the voltage U is measured (Fig. 3.7a). Although U also depends on the positions, i.e. rf-frequency, the shape of the power dependence is identical for all (x, y) as can be seen when normalising the voltage (Fig. 3.7b). The mean of all U/U_{max} curves can be well described by a polynomial of the form

$$f(x) = c_1 x + c_2 x^2 + c_3 x^3 + c_4 x^4, \tag{3.8}$$

which is shown as a black line. This expression is arbitrarily chosen and the fitted parameters c_1 to c_4 are used to calculate the required P_{rf} to reach equidistant diffraction efficiencies, which are then saved in a look-up table. Hereafter, relative power values $0 \leq P_{\mathrm{rel}} \leq 1$ are used and the power of the rf-input is calculated according to

$$P_{\mathrm{rf}} = 250\ \mathrm{mW} \cdot P_{\mathrm{rel}}. \tag{3.9}$$

Note that $P_{\mathrm{rf,max}} = 250$ mW is chosen to be well below the rf-power at which the diffraction efficiency of the AOD saturates. Larger $P_{\mathrm{rf,max}}$ leads to a frequency dependence of the normalised curves which would decrease the quality of the linearisation. In Figs. 3.7c and 3.7d the performance of the linearisation is shown.

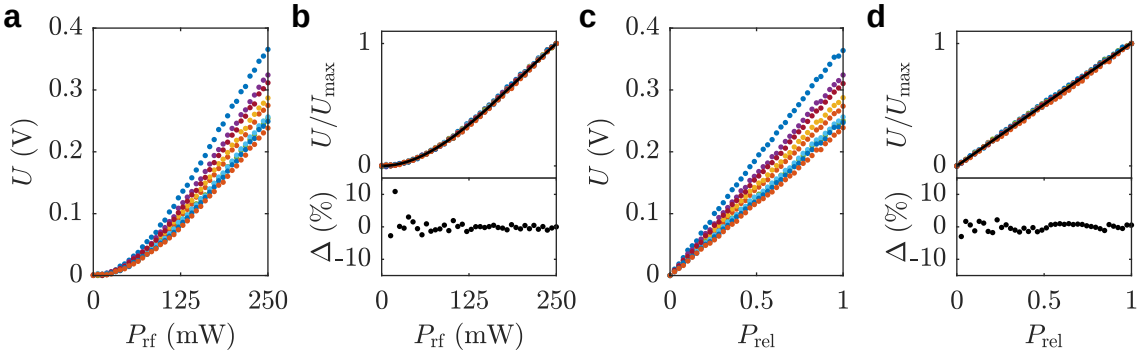

Figure 3.7: Linearisation of the diffraction efficiency. **a** Measured voltage U vs. the rf-power P_{rf} for 9 positions spanning the field of view. **b** Normalised signals and the corresponding fit (black line) according to Eq. (3.8) (top) and the residuals (bottom). **c** Voltage U vs. the linearised rf-power P_{rel} for the same positions as in **a**. **d** Normalised signals with a linear fit (top) and the corresponding residuals (bottom).

The second part of the calibration compensates the frequency dependence of the diffraction efficiency of the AOD. The voltage U is measured for a grid of 320 positions (20 in x-direction, 16 in y-direction) at rf-power $P_{\mathrm{rel}} = 0.5$. The grid points are equidistant and span a region which is in each direction $\approx 4\%$ larger than the experimental field of view. This allows a proper intensity matching even when positional corrections (see the following calibrations) need to be applied. The measured voltage U is interpolated to a 1 px precision (Fig. 3.8a) and the correction for the rf-power at each point is then given by

$$f_{\mathrm{corr}}(x, y) = \frac{U_{\mathrm{min}}}{U(x, y)}, \tag{3.10}$$

with U_{min} the smallest measured voltage. Combined with Eq. (3.9) this leads to the needed rf-power

$$P_{\mathrm{rf}}(x, y) = 250\ \mathrm{mW} \cdot P_{\mathrm{rel}} \cdot f_{\mathrm{corr}}(x, y). \tag{3.11}$$

After applying this correction, the voltage U and hence the laser intensity is independent of the position as shown in Fig. 3.8b for $P_{\mathrm{rel}} = 0.5$. The correction is also valid for different values of P_{rel} (blue data in Fig. 3.8c). Comparing the input laser power, i.e. at the entrance of the AOD, with the laser power at the sample stage, the total efficiency of the AOD is $\approx 11.3\%$ for the experimentally used timings and $P_{\mathrm{rel}} = 1$.

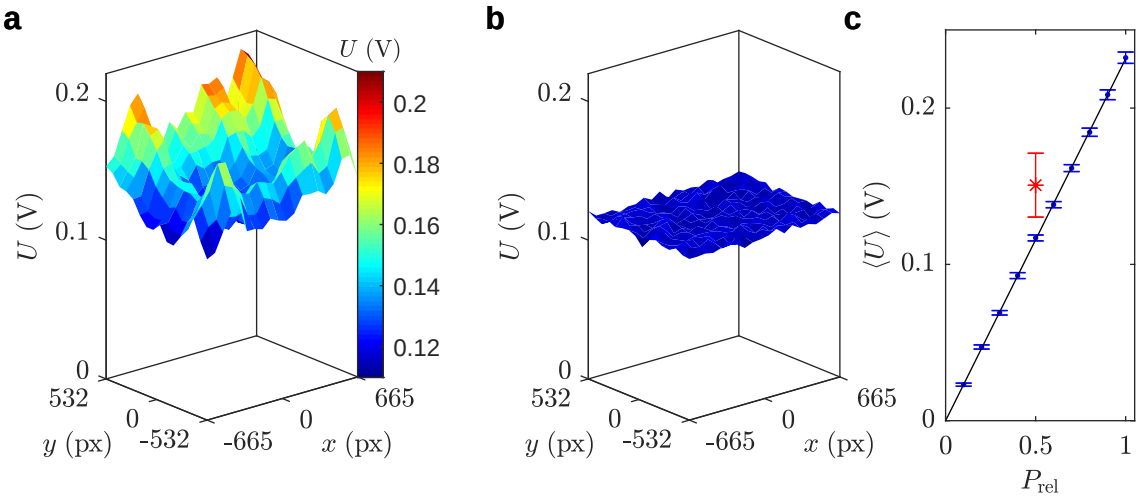

Figure 3.8: Flatfield calibration of the diffraction efficiency. **a** Voltage U for a grid of 20 (x-direction) times 16 (y-direction) positions at rf-power $P_{\mathrm{rel}} = 0.5$. **b** Voltage U after applying the flatfield calibration for the same positions as shown in **a**. **c** Mean voltage $\langle U \rangle$ averaged over all positions vs. the rf-power P_{rel} without (red) and with (blue) application of the flatfield calibration. Error bars correspond to the standard deviation of different positions. The black line is a linear fit to the blue data.

Position calibration

The relation between rf-frequency and position of the laser beam given by Eq. (3.7) is not precise enough for the experimental requirements. Two additional calibrations are used to match the real position of the laser beam with its supposed position, i.e. the position input in Eq. (3.7) is changed according to

$$\begin{aligned} x' &= x - \Delta_x(x, y), \\ y' &= y - \Delta_y(x, y), \end{aligned} \tag{3.12}$$

with x', y' the new input and Δ_x, Δ_y the position-dependent correction values.

Beam imaging: The first position calibration is supposed to correct large deviations, i.e. deviations on the order of ≈ 10 px. In this calibration, first the beam position is acquired by imaging and fitting of the laser beam for a grid of positions (x, y) which typically consists of more than 500 positions. Red data in Fig. 3.9a shows the distribution of the differences between the supposed and the fitted beam positions. Next, these differences are smoothed with their two next neighbours in each direction to reduce influence of errors arising from interference of the laser light on the camera chip. Finally, the smoothed data is inter- and extrapolated to a 1 px precision grid covering the whole field of view (Fig. 3.9b). Applying these corrections, deviations between fitted and supposed beam positions are strongly reduced to typically less than 2 px (black data in Fig. 3.9a).

Although this calibration method reliably corrects large deviations, due to its methodology it is not suitable to calibrate the position of the beam within the sample cell relative to the detected AP positions. As the optical path of the LED light (used for AP detection) and the laser light is not identical within the imaging optics, the positions on the camera (typically) do not match. Sources of this mismatch include e.g. aberrations due to small angular differences, chromatic aberrations and displacements when the light is passing through filters.

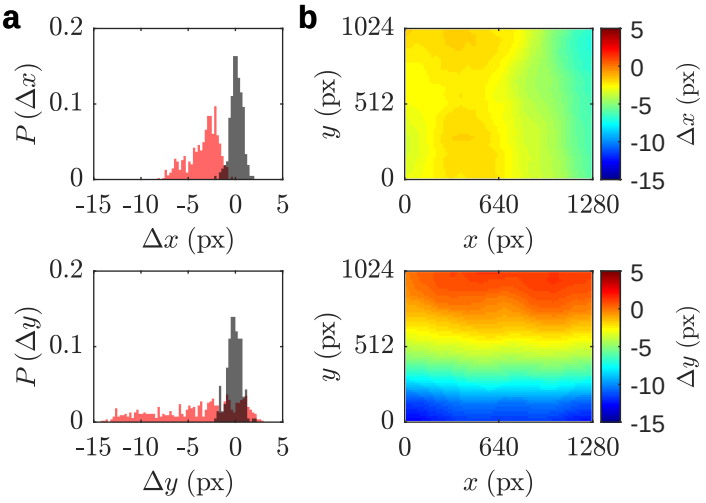

Figure 3.9: Position calibration by beam imaging.
a Probability distribution of the positioning error Δx and Δy without (red) and with (black) correction acquired by comparing a Gaussian fit of the imaged beam with its supposed position.
b Corresponding correction tables for the position adjustment.

Light scattering: The second calibration matches particle and laser position by using the light that scatters at particles and whose intensity depends on the overlap between beam and particle. For this calibration, a sample is prepared in which the coated APs are replaced by uncoated silica particles. This is necessary as otherwise the intensity of the scattered light would depend on the particle orientation.

A typical particle distribution that can be used for this calibration is shown in Fig. 3.10a. The number of particles in the field of view should be as large as possible to increase statistics, however, it is important that distances between particles are sufficiently large ($\gtrsim$ 50 px). The corrections Δ_x and Δ_y are now measured for the position of each particle independently. To minimise the effect of translational diffusion, particle positions are updated before starting the next data point.

The laser beam is scanned on a grid (50 px length, 15 $\times$ 15 points) centred at the detected position of the particle (sketch in Fig. 3.10a). Using an amplified photodiode[7], the intensity of the scattered light is recorded (Fig. 3.10b). The pause between consecutive scans of the grid is used to correlate the relative laser position with the amplitude of the signal. The position of the maximum is then extracted using a two-dimensional Gaussian fit to the data. The choice of a fit function is motivated by the shape of the signal, however, the precise expression used for the

[7] Thorlabs PDA100A

fit is not important here. The measured shifts Δ_x and Δ_y are first interpolated between the particles to a grid with 1 px resolution, then the data is smoothed to reduce effects of the particle motion during the calibration. A smoothing range of 100 px to either side was found to give best results. Finally, the smoothed data is extrapolated to the whole field of view (Fig. 3.10c).

Checking the final performance of the calibration (Fig. 3.10d), it can be seen that deviations between laser and particle position are typically smaller than 1 px, which is also the limitation for the detection of particle positions.

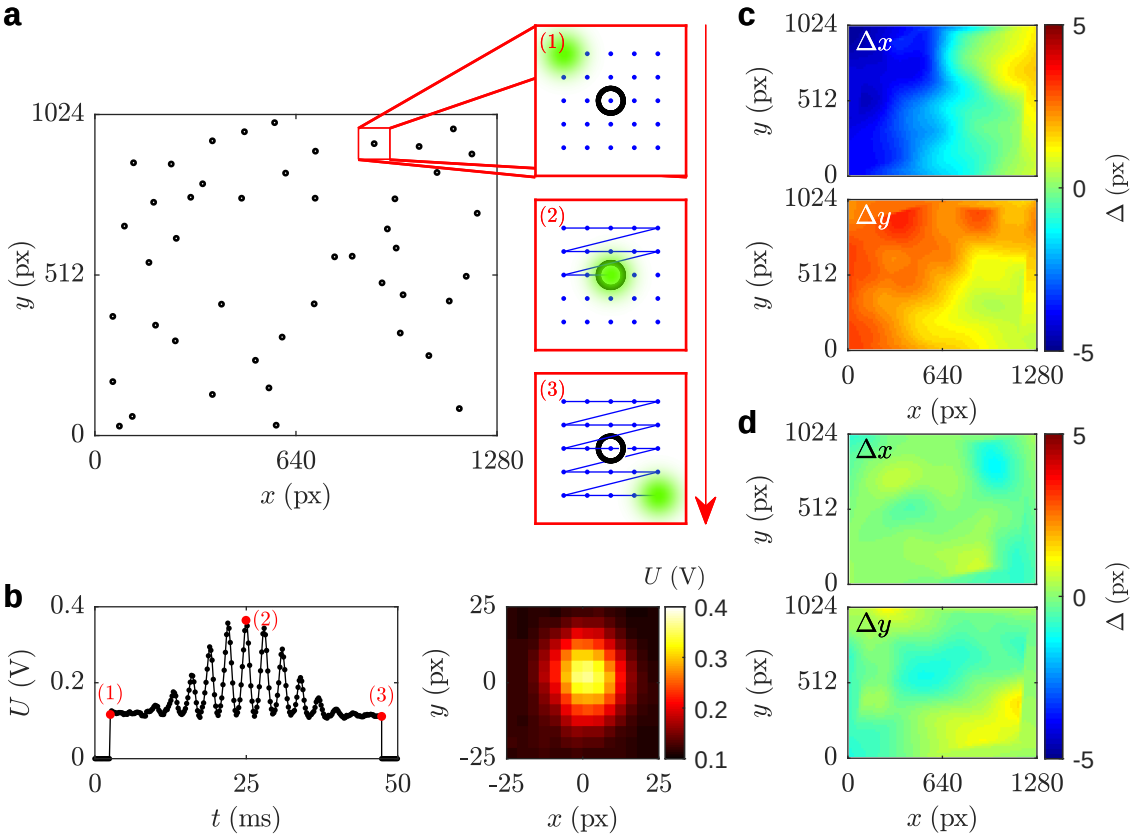

Figure 3.10: Position calibration by light scattering. **a** The laser beam is scanned over a grid surrounding the area of each uncoated particle. **b** Scattering signal acquired by the photodiode and the corresponding two-dimensional visualisation. **c** Resulting correction tables Δ_x and Δ_y. **d** After all corrections are applied, deviations between particle position and laser beam are typically smaller than 1 px.

In addition to the position-dependent deviation, which is corrected by this calibration, it is possible that the relative position of laser and detected particles changes over time, e.g. due to a change of the temperature around the experimental setup. The corrections that are needed to compensate this effect, however, are position-independent and can therefore be adjusted based on the active motion of APs.

Correction of the illumination intensity

In order to achieve stable propulsion of APs, the size of the illuminating laser beam needs to be similar to the size of the AP. Accordingly, laser beams overlap when distances between APs become small during experiments. Without correction, illumination intensities on the APs would increase, resulting in a higher swimming velocity. In order to compensate the effect of overlapping beams, it is necessary to reduce the beam intensities.

The radial intensity profile of the Gaussian beam illuminating AP i is given by

$$I_i(r) = I_{0,i} \exp\left(-\frac{2r^2}{w^2}\right), \tag{3.13}$$

with beam waist w and peak intensity $I_{0,i}$. Due to overlapping beams of other APs in its proximity, the intensity in the centre of particle i increases by

$$\Delta I_i = \sum_{i \neq j} I_{0,j} \exp\left(-\frac{2r_{ij}^2}{w^2}\right), \tag{3.14}$$

with distance r_{ij} between APs i and j. Because the exponential term decreases rapidly, it is sufficient to include only contributions with $r_{ij} < 2w$ in the summation. When the peak intensities are reduced according to

$$\hat{I}_{0,i} = \frac{I_{0,i}}{(1 + \Delta I_i)^{1.4}}, \tag{3.15}$$

the integrated illumination of each AP becomes independent of the particle configuration as tests of this empirical relation have shown for various arbitrary configurations with only active and mixtures of active and passive particles.

The performance of the correction is illustrated based on a typical particle configuration during quorum sensing experiments (Fig. 3.11a). The illumination intensity is supposed to be $I = 0$ for non-motile (blue) and $I = 0.2$ W/mm^2 for motile (red) particles when averaged over the AP with diameter $\sigma = 4.4$ µm. Without applied correction and beam waist $w = 5$ µm, the illumination intensity is up to 50% larger than intended (Fig. 3.11b). However, when the correction is applied, the effect of overlapping beams nearly vanishes for motile particles (Fig. 3.11c). Obviously, the correction does not affect non-motile particles as much because, even without correction, the intensity of the corresponding beam is already set to zero. Experimentally this is not relevant as the intensity is below the threshold intensity for the onset of self-propulsion indicated by the dotted line.

3.3.2 Real-time particle detection

In feedback controlled experiments, the applicability of a particle detection method depends on two competing features: its precision and robustness on the one side, and

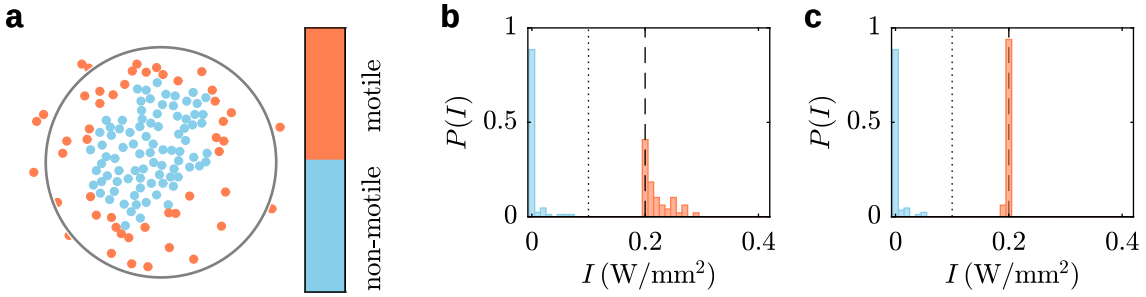

Figure 3.11: Correction of the illumination intensity. **a** Typical particle configuration during quorum sensing experiments. In order to achieve the supposed propulsion velocity, motile particles (red) need illumination intensity $I = 0.2$ W/mm^2, non-motile particles $I < 0.1$ W/mm^2, i.e. an intensity below the onset of self-propulsion (dashed and dotted lines in **b**,**c**). **b** Distribution of the corresponding integrated illumination intensity for beam waist $w = 5$ µm without intensity correction. **c** Same situation with intensity correction. [2].

the speed of the algorithm on the other. In this thesis, the detection methods were continuously improved to meet increasing experimental requirements. In general, the particle detection gets more complicated and time-consuming with an increasing number of particles in the system. Especially when particles collide, i.e. the distance between them vanishes, not all detection methods can reliably detect the particles. The method which delivers best results, both considering speed and robustness of the detection, is presented in the following. Position and orientation of particles are computed in two distinct steps.

Position detection: Under the experimental conditions, particles have a dark, circular ring around them in the video microscopy images (Fig. 3.12a). This feature allows the position detection by a circular Hough transform based on phase-coding [119] and adapted from the *imfindcircles*-function in *MATLAB* [120]. In the first step, the image is convolved with a Sobel filter in x- and y-direction and the resulting directional gradients are combined to a gradient image (Fig. 3.12b). In order to reduce calculation time in the next steps, a threshold is used on the gradient image to include only pixels where the gradient is sufficiently large. Each of these pixels contributes in the calculation of the so-called accumulator (Fig. 3.12c). Based on the direction of the gradient at this pixel, a circle centre is estimated for a range of radii around the known particle radius. The coordinates of these centres are then weighted by a complex number, corresponding to the radius they originated from, and accumulated. This allows the detection of circles with different radius, which can be present due to polydispersity of the particle size. Localisation of the peaks in the accumulator gives the centres of the particles. In order to enhance the computation speed, this localisation is restricted to a 1 px resolution.

Orientation detection: Close to the centre of a carbon coated particle, the brightness of the image increases from coated to uncoated side. Using the pixels closer to the centre than approx. half of the particle radius (coloured area in Fig. 3.12d), the particle orientation can be obtained from this feature by doing a principle component analysis of the brightness with respect to x- and y-position. Projecting the eigenvector of the largest eigenvalue to the x-y-plane gives the orientation of the particle (Fig. 3.12e).

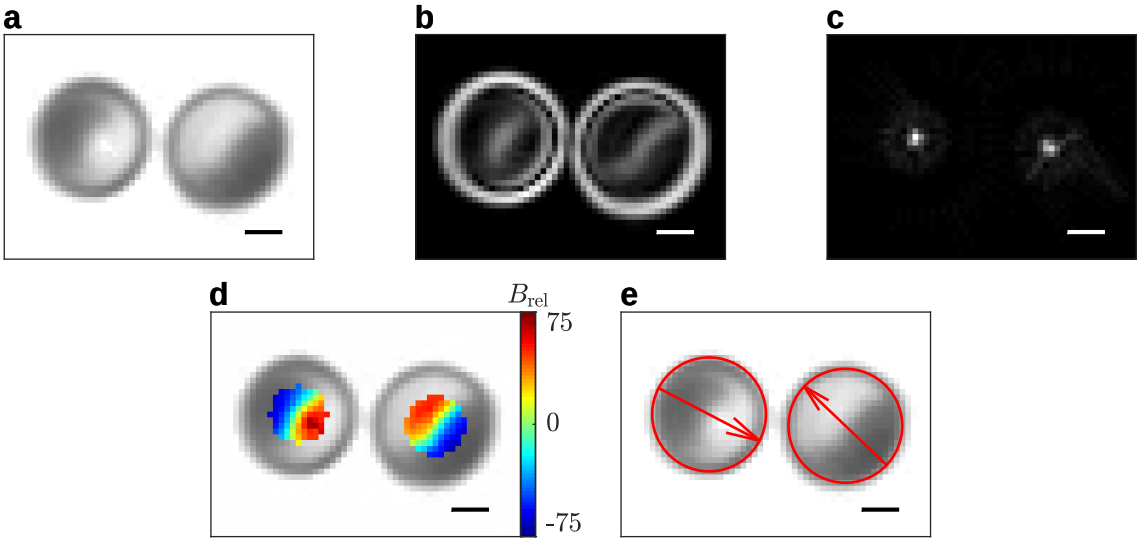

Figure 3.12: Particle detection. **a** Snapshot of two APs. **b** Gradient image calculated from the snapshot in **a**. **c** Accumulator resulting from the circular Hough transformation. **d** The central region of APs (coloured area) is used for the orientation detection. Colour code corresponds to the relative brightness B_{rel} of the coloured pixels **e** Result of the particle detection, arrows indicate the APs' orientation. Scale bars are 2 µm

3.3.3 Feedback control

Individual control of the propulsion properties of APs requires a feedback control for two reasons. First, as APs are constantly moving, it is necessary to regularly adjust the laser beam positions to ensure APs are illuminated as intended. Secondly, the change of the particle propulsion, as a response of an AP to its surroundings, requires changes in the position (torques) and power of the laser beam (velocity). The needed update rate of the feedback depends on the dynamics of configurational changes in the system, i.e. on the propulsion velocity and rotation of the APs. In all projects, the update rate was set to either 2 Hz or 5 Hz, so that APs typically move less than $\approx 5\%$ of their diameter between updates. In this interval, also the changes of the particle orientations are negligible as the rotational diffusion time is

at least ≈ 120 s for all used particle sizes. Accordingly, updates of the laser beams are quasi-instantaneous. The feedback control consists of the following three steps.

Image acquisition and particle detection: An image of the APs is recorded by video microscopy. This image is then evaluated to detect the particle positions and orientations (see Section 3.3.2).

Interaction rule: An interaction rule defines the response of an AP to its surroundings and can be defined arbitrarily, i.e. the rule is not limited to physical interactions. In particular, this allows to introduce non-reciprocal interactions between APs, which is e.g. important to model real biological systems. Based on the interaction rule and the positions and orientations of all APs in the system, a propulsion velocity v and torque Γ is calculated for each AP.

AOD sequence: From all v and Γ, the required positions and powers of the laser beams are calculated and converted to the corresponding rf-input for the AOD using the calibrations (Section 3.3.1).

Chapter 4

Navigation of individual active Brownian particles

Efficient navigation is a prerequisite for a variety of possible applications in systems of microswimmers. For example, the use as carriers for drug delivery in medical applications [121] or the controlled deposition of building blocks to assemble larger structures [122] need the possibility to direct the cargo towards the designated region. In externally controlled systems, e.g. magnetically activated microswimmers [123, 124], the direction of motion can be imposed from the outside. Accordingly, the navigation in such cases is a rather simple task. However, in systems of active Brownian particles (APs) different pathways for the navigation have to be used. Possibilities are for example the hydrodynamic guiding of APs at topological structures [125] or chemo- and phototactic steering [72, 126, 127]. In addition, also the random particle reorientation due to rotational diffusion can be exploited for the navigation of APs, as shown in the following.

When adjusting the swimming velocity of an AP according to its orientation, it is possible to stochastically control its swimming direction. This means that a target can be reached by the alternation between phases of active and diffusive motion, depending on whether the AP orientation is favourable to reach the target. The decision of the AP's swimming velocity follows a navigational policy, termed control strategy in the following. This steering method was shown to be applicable for the localisation of particles [93] and theoretically also proposed as a steering mechanism [128].

In this chapter, different control strategies will be employed to steer an AP towards a predefined target area and their performance with respect to, potentially, limited resources will be compared.

4.1 Control strategies

The goal of the steering is to direct an AP from its starting position $\mathbf{r}_0 = (0, 0)$ towards a target area located at $\mathbf{r}_\mathrm{T} = (l, 0)$ with diameter σ_T, identical to the particle diameter (red arrows of length l and red circles in Fig. 4.1). The initial orientation $\hat{\mathbf{u}}_0$ of the AP is aligned with the direct connection to the target (the

ideal path), i.e. $\hat{\mathbf{u}}_0 \parallel \mathbf{r}_\mathrm{T} - \mathbf{r}_0$. Three different control strategies (sketched in Fig. 4.1) are used to adjust the swimming velocity $v(t) = v\left(\mathbf{r}(t), \hat{\mathbf{u}}(t)\right)$ between $v = 0$ and the maximum velocity $v = v_\mathrm{max}$, based on the position $\mathbf{r} = (r_x, r_y)$ and the orientation $\hat{\mathbf{u}} = (u_x, u_y)$ of the AP.

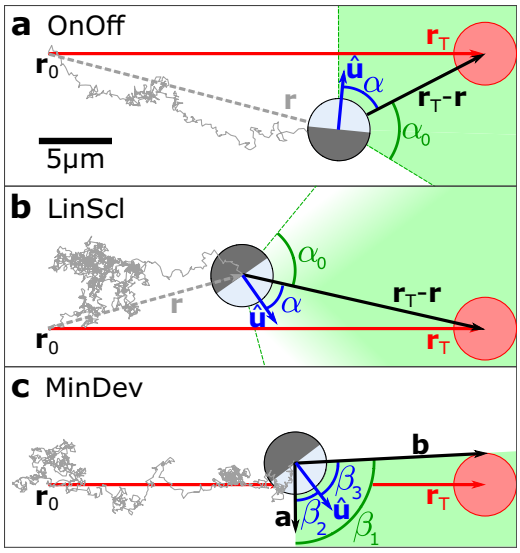

Figure 4.1: Sketch of the different control strategies.
a OnOff strategy.
b Linear scaling (LinScl) strategy.
c Minimal deviation (MinDev) strategy.
In all cases, the red arrow indicates the ideal path from initial position $\mathbf{r}_0$ to the target area (red circles) located at $\mathbf{r}_\mathrm{T}$. When it is oriented towards the green area, the AP self-propels with $v = v_\mathrm{max}$ (OnOff, MinDev) or $0 < v \leq v_\mathrm{max}$ (LinScl). Otherwise, it is diffusive, i.e. $v = 0$. In **c**, the length of vector **a** is increased for visibility. [1]

- **OnOff strategy (Fig. 4.1a)**
  The self-propulsion of the AP is either switched on or off, depending on the angle α between orientation $\hat{\mathbf{u}}$ and direction towards the target $\mathbf{r}_\mathrm{T} - \mathbf{r}$ given by

$$\alpha = \arccos\left(\hat{\mathbf{u}} \cdot \frac{\mathbf{r}_\mathrm{T} - \mathbf{r}}{|\mathbf{r}_\mathrm{T} - \mathbf{r}|}\right). \tag{4.1}$$

  α is compared with the parameter α_0 of the control strategy leading to the velocity

$$v_\mathrm{OnOff} = \begin{cases} v_\mathrm{max}, & \alpha \leq \alpha_0 \\ 0, & \alpha > \alpha_0. \end{cases} \tag{4.2}$$

- **Linear scaling (LinScl) strategy (Fig. 4.1b)**
  In contrast to the OnOff strategy, the self-propulsion is not either turned on or off, but v is linearly reduced with increasing α according to

$$v_\mathrm{LinScl} = \begin{cases} v_\mathrm{max} \cdot \frac{\alpha_0 - \alpha}{\alpha_0}, & \alpha \leq \alpha_0 \\ 0, & \alpha > \alpha_0. \end{cases} \tag{4.3}$$

- **Minimal deviation (MinDev) strategy (Fig. 4.1c)**
  This strategy is designed to keep the distance between AP position and the ideal path as small as possible, while still navigating towards the target. When the particle is oriented towards the green area in the sketch, the self-propulsion

is turned on, otherwise it is turned off. This area is defined by the connections from AP position $\mathbf{r}$ to the ideal path, $\mathbf{a} = (0, -r_y)$, and to the boundary of the target area, $\mathbf{b} = \mathbf{r}_\mathrm{T} - \mathbf{r} + (0, \mathrm{sgn}(r_y)\ \sigma_\mathrm{T}/2)$, respectively. The condition can be described using the angles

$$\beta_1 = \arccos\left(\hat{\mathbf{a}} \cdot \hat{\mathbf{b}}\right), \tag{4.4}$$

$$\beta_2 = \arccos\left(\hat{\mathbf{a}} \cdot \hat{\mathbf{u}}\right), \tag{4.5}$$

$$\beta_3 = \arccos\left(\hat{\mathbf{b}} \cdot \hat{\mathbf{u}}\right), \tag{4.6}$$

with $\hat{\mathbf{a}} = \mathbf{a}/|\mathbf{a}|$, $\hat{\mathbf{b}} = \mathbf{b}/|\mathbf{b}|$. From these angles, the swimming velocity is defined according to

$$v_\mathrm{MinDev} = \begin{cases} v_\mathrm{max}, & \beta_2 < \beta_1 \text{ and } \beta_3 < \beta_1 \\ v_{\mathrm{OnOff}\ 63^\circ}, & (l - \sigma_\mathrm{T}/2) < r_x < (l + \sigma_\mathrm{T}/2) \\ 0, & \text{else.} \end{cases} \tag{4.7}$$

The middle case applies to events when the AP is directly above or below the target area. Then the condition for self-propulsion (upper case) is unlikely to be met and the velocity is calculated according to v_OnOff with $\alpha_0 = 63^\circ$.

In the following, the control strategies that require an input parameter will be denoted OnOff α_0 and LinScl α_0, respectively, and treated as different control strategies depending on α_0.

4.2 Methods

4.2.1 Experimental parameters

In contrast to the following chapters, the experiments in this chapter were carried out using only one AP per measurement. This makes it unnecessary to regulate the laser intensity, i.e. the self-propulsion of APs, locally. Therefore, the AP is activated by a homogeneous laser illumination generated by scanning the laser beam with a frequency of 100 kHz to a grid of 980 equally spaced positions covering the whole field of view. The beam waist of the laser is adjusted to be approximately three times as large as the grid spacing, resulting in a flat intensity profile within the experimentally used region.

APs in the experiments have a diameter $\sigma = 4.2$ µm and a 30 nm carbon coating on one hemisphere. The thin sample cells ($\approx 2\sigma$) are heated to 2 K below the critical temperature. Under these conditions, the translational motion of APs is restricted to the x-y-plane due to gravitational forces, but they rotate in 3D. Translational and rotational diffusion constants D_T and D_R were experimentally determined to $D_\mathrm{T} = 0.027$ µm^2/s and $D_\mathrm{R} = 0.0083$ 1/s, corresponding to a reorientation time

$\tau = 1/D_\mathrm{R} = 120$ s. The velocity of APs is adjusted between 0 and $v_\mathrm{max} = 0.2$ µm/s at a rate of 2 Hz. In this regime, the performance of the navigation is independent of the rate as confirmed by numerical simulations.

4.2.2 Numerical simulations

Numerical simulations are performed by the discrete integration of the coupled equations of motion of the AP. As the rotational diffusion is not restricted to one degree of freedom under the experimental conditions in this chapter, also the out-of-plane rotational diffusion has to be taken into account. Therefore, the angular part (Eq. (2.13)) becomes vectorial, i.e. $\boldsymbol{\theta} = (\theta, \theta_\mathrm{out})$. The corresponding discrete integration is given by

$$\mathbf{r}(t+\tau) = \mathbf{r}(t) + \boldsymbol{\xi}_\mathrm{T} \cdot \sqrt{\tau} + \Delta\mathbf{r}_\mathrm{active}(\mathbf{r}(t), \hat{\mathbf{u}}(t)), \tag{4.8}$$

$$\boldsymbol{\theta}(t+\tau) = \boldsymbol{\theta}(t) + \boldsymbol{\xi}_\mathrm{R} \cdot \sqrt{\tau}, \tag{4.9}$$

with normal distributed, uncorrelated variables $\boldsymbol{\xi}_\mathrm{T}$ and $\boldsymbol{\xi}_\mathrm{R}$, characterised by zero mean and component-wise variance $2D_\mathrm{T}$ and $2D_\mathrm{R}$, respectively. The active displacement calculates to

$$\Delta\mathbf{r}_\mathrm{active} = \sqrt{2}\,\mathbf{u} \cdot v(\mathbf{r}, \hat{\mathbf{u}}) \cdot \tau, \tag{4.10}$$

with the in-plane orientation $\mathbf{u} = (\cos(\theta), \sin(\theta)) \cdot \cos(\theta_\mathrm{out})$ and $\hat{\mathbf{u}} = \mathbf{u}/|\mathbf{u}|$. The parameters D_T, D_R, v and τ in the simulations are set to the experimental values (Section 4.2.1). For each set of control parameters, e.g. different control strategies or target distances, simulations are repeated 600 times in order to obtain sufficient statistics. In each case, the particle trajectory is simulated for a time span of 21600 s = 6 h, or until the target area is reached.

4.2.3 Quantification of the navigation performance

The simplest criterion to judge the performance of any control strategy is its ability to navigate the AP to its target. For the comparison between different control strategies, however, this is not sufficient as most of the strategies reliably steer the AP. Therefore, the characterisation of the performance needs additional figures of merit. Considering the discrete time steps i with interval τ and the total number N of steps needed to reach the target, these are defined as follows:

- Time T
  The total time T the AP needs to reach the target

$$T = \sum_{i=1}^{N} \tau. \tag{4.11}$$

- Path deviation D
  The root-mean-square distance D to the ideal path

$$D = \sqrt{\frac{1}{N}\sum_{i=1}^{N} r_{y,i}^2}. \tag{4.12}$$

- Propulsion energy E
  The total propulsion energy E used for the self-propulsion

$$E = \sum_{i=1}^{N} I_i \, \tau, \tag{4.13}$$

  with the laser intensity I_i at time step i. In this quantity, the laser intensity is used rather than the laser power and therefore the unit of E is an energy per area.

- Total distance S
  The total distance S that an AP covers during the navigation

$$S = \sum_{i=1}^{N-1} \left|\mathbf{r}_{i+1} - \mathbf{r}_i\right|. \tag{4.14}$$

  As S does not only sum up the self-propelled motion of the AP, but also the contributions due to Brownian motion, this quantity strongly depends on the interval τ between the time steps.

These figures of merit allow to distinguish the performance of different control strategies with respect to, possibly limited, resources available for the navigation. The time T can for example be relevant if the microswimmer or, in case of delivery applications its cargo, has a limited lifetime. Similarly, the propulsion energy E can be important when the fuel for the self-propulsion is scarce. Obviously, the limitation of resources is highly system-dependent and thus the figures of merit need to be adapted to the specific conditions.

4.3 Results

4.3.1 Arrival probability

Even without any control, APs have a finite probability to reach the target area due to their random motion. In Fig. 4.2a this arrival probability P is shown vs. the target distance l for purely active ($v = v_{\max}$, solid line) and passive ($v = 0$, dashed line) particles, obtained from numerical simulations. For active particles the arrival probability is larger, but in both cases P decreases rapidly with l. Accordingly, the

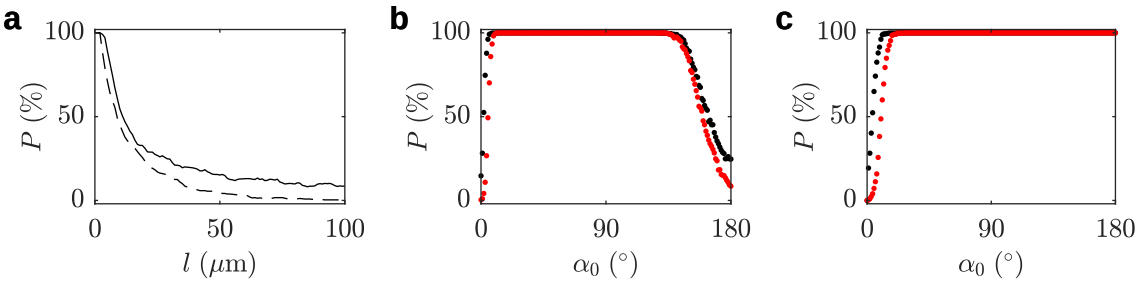

Figure 4.2: Arrival probability P. **a** P vs. target distance l for uncontrolled, permanently active (solid line) and passive (dashed line) particles to reach the target area. [1] **b** and **c** α_0-dependent probability P that the control with the OnOff α_0 (**b**) and LinScl α_0 (**c**) strategy is successful. Black (red) data corresponds to target distance $l = 30$ µm ($l = 100$ µm). All data is obtained from numerical simulations.

navigation becomes more relevant for large l. However, this also causes an increase of the time an AP needs to reach the target. In the following sections, the target distance is set to $l = 30$ µm or $l = 100$ µm with corresponding probability $P \lesssim 25\%$ and $P \lesssim 10\%$, respectively, for permanently active particles to reach the target by chance.

When APs are navigated using the OnOff or LinScl control strategy, the arrival probability P depends on the parameter α_0. This is shown in Fig. 4.2b for OnOff with target distances $l = 30$ µm (black) and $l = 100$ µm (red). Over a large range of α_0, all APs arrive at the target and only at the edges of the α_0-range navigation breaks down. This is because small and large α_0 correspond to the uncontrolled cases of purely passive ($\alpha_0 = 0°$) and active ($\alpha_0 = 180°$) particles. In contrast to this, LinScl does not show this breakdown at large α_0 (Fig. 4.2c) as the velocity reduction in case of unfavourable orientations still imposes a preferential direction. For experiments, all control strategies with $P = 100\%$ in the 6 h simulation time are suitable as this time scale is experimentally accessible.

4.3.2 Navigation of active particles in experiments

In the first experimental realisation of AP navigation, five different control strategies are investigated at a fixed target distance $l = 30$ µm. These control strategies are OnOff with $\alpha_0 = [13°, 32°, 63°]$, LinScl with $\alpha_0 = 63°$ and MinDev. The values of α_0 in the OnOff strategies correspond to the smallest angle for which APs reliably reach the target within 6 h ($\alpha_0 = 13°$) and the angles optimising T ($\alpha_0 = 63°$) and D ($\alpha_0 = 32°$), determined from numerical simulations (Fig. 4.3).

As supposed by these simulations, in all repetitions of the experiment APs reach the target. Comparing typical trajectories for each of the strategies (Fig. 4.4), large differences can be found. Trajectories of APs controlled with OnOff 63° exhibit a combination of straight motion during active intervals and passive reorientation phases. A reduction of α_0 leads to more and longer reorientation phases, as can be

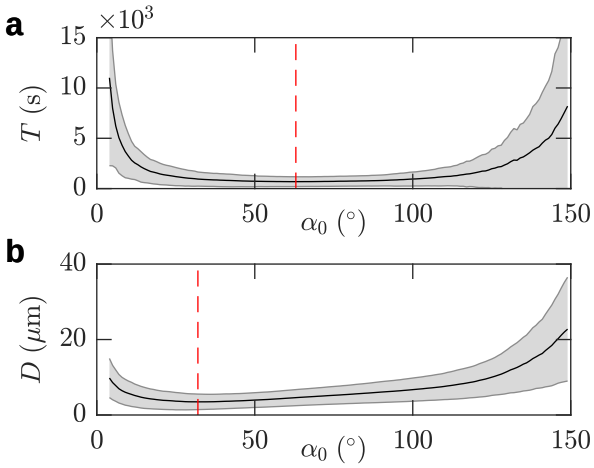

Figure 4.3: Performance of the OnOff strategy.
a T and **b** D depending on the angle α_0 for the control with the OnOff strategy and target distance $l = 30$ µm. The minima of T and D are located at $\alpha_0 = 32°$ and $\alpha_0 = 63°$ (red lines). Shaded error bands correspond to the standard deviation of 600 simulated trajectories. [1]

seen in the case of control with OnOff 32°, and ultimately results in trajectories that are completely dominated by diffusive motion (OnOff 13°). The control with LinScl 63° results in similar trajectories as in the case of OnOff 63°. As a small difference, it can be noticed that the motion during active intervals is not as straight which can be explained by the reduced swimming velocity. The MinDev strategy leads to trajectories with a large fraction of diffusive motion. In contrast to OnOff 13°, however, trajectories are typically closely confined near the ideal path.

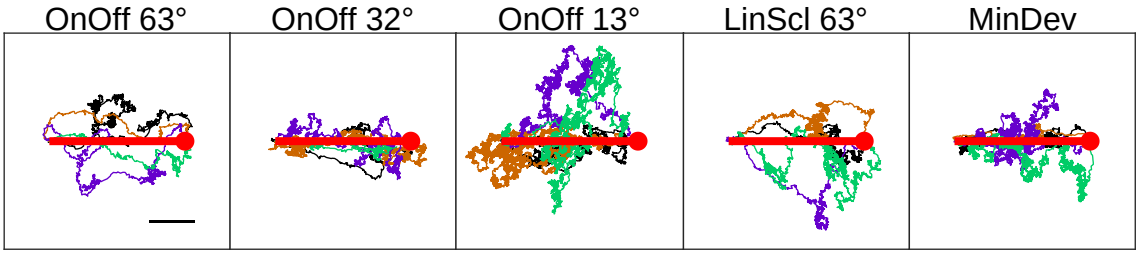

Figure 4.4: Experimental trajectories for a target distance $l = 30$ µm and five different control strategies. The target area and ideal path are shown as a red circle and line, respectively. Scale bar is 10 µm. Extended from [1].

In order to compare the navigation performance of the strategies quantitatively, the previously defined figures of merit are calculated from the trajectories (Figs. 4.5a to 4.5d). The most intuitive of these quantities, the total time T the AP needs to reach the target, is shortest in the case of control with OnOff 63° and shows an increase of more than a factor of 3 when the angle α_0 is reduced to 13°. The performance of the other investigated control strategies regarding T is in between these two cases. This behaviour is also expected from numerical simulations which show a nearly perfect agreement with the experimental results, in both the mean value and the standard deviation of different repetitions (black and red symbols in Fig. 4.5a). Differences of the performance regarding the root-mean-square distance D to the ideal path or the propulsion energy E are less prominent (Figs. 4.5b

and 4.5c). In case of D, results from experiments and numerical simulations differ slightly and experimental values are systematically larger. A possible origin for this deviation is that the swimming direction of APs in experiments is, in contrast to numerical simulations, distributed around their orientation and not always perfectly aligned with it. The total moved distance S shows a nearly identical dependence on the control strategy as T. This can be explained as the translational diffusion of the AP dominates its motion for small time steps τ as can be seen by comparing the diffusive ($\propto \tau$) and ballistic ($\propto \tau^2$) component of the MSD. Accordingly, it can be expected that for larger τ the dependence of S on the control strategy will change from the similarity with T to a similarity with E.

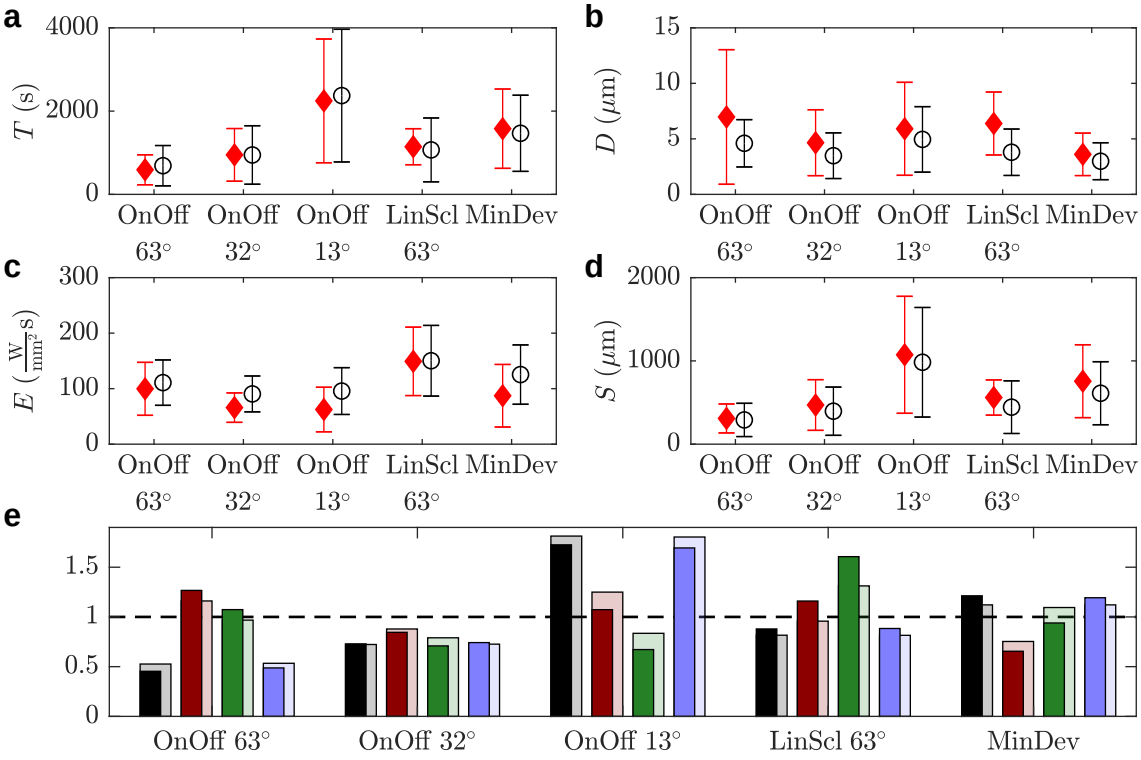

Figure 4.5: Navigation performance with target distance $l = 30$ µm. **a-d** Figures of merit T, D, E and S obtained from experiments (red) and numerical simulations (black). Error bars correspond to the standard deviation of different repetitions. **e** Renormalised figures of merit $\widetilde{T}$ (black), $\widetilde{D}$ (red), $\widetilde{E}$ (green) and $\widetilde{S}$ (blue). Filled bars correspond to experiments and transparent bars to numerical simulations. The dashed line indicates the average of all strategies. Extended from [1].

For a comparison of the different control strategies with respect to all figures of merit, their performance is summarised in Fig. 4.5e. Here, the values of each figure of merit $F = [T, D, E, S]$ is normalised according to

$$\widetilde{F} = \frac{F}{\langle F \rangle}, \tag{4.15}$$

with $\langle\cdot\rangle$ being the average over all investigated strategies. Accordingly, $\langle\widetilde{F}\rangle = 1$ (dashed line) and values below or above correspond to a good or bad relative performance. An important finding is that no best strategy exists, i.e. one that outperforms all others in every aspect. For example, OnOff 63° optimises T and S, but therefore shows performance below average in D and E, and OnOff 32° performs well in all figures of merit. LinScl 63°, in contrast, is globally outperformed by OnOff 32°. It should be noted that considering E, LinScl has a strong disadvantage due to the used propulsion mechanism. Because a threshold intensity has to be exceeded to activate self-propulsion, even small velocities $v \approx 0$ require a non-negligible intensity.

4.3.3 Variation of the target distance

Although the MinDev strategy is defined to optimise D, it is only slightly better than OnOff 32° for $l = 30$ µm. This indicates that this target distance is not large enough for the advantage of the MinDev strategy to become relevant. Figure 4.6 shows the dependence of D on l for both the MinDev (black) and the OnOff α_0 (red) strategy determined from numerical simulations. For each target distance, $\alpha_0 = \alpha_0(l)$ is chosen to minimise D. The numerical results show that differences between MinDev and OnOff are negligible for small l but become relevant when l is increasing as D saturates for MinDev but keeps increasing for OnOff.

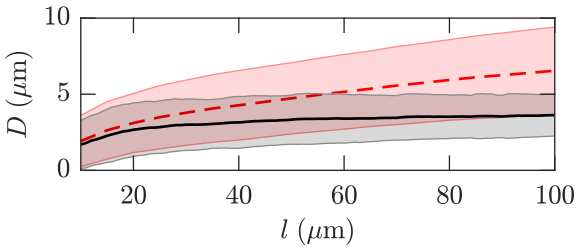

Figure 4.6: Dependence of D on the target distance l for the MinDev (black) and the OnOff α_0 (red) strategy. For each l, α_0 is chosen to minimise D. Error bands correspond to the standard deviation of 600 simulated trajectories. [1]

Experimentally, three different strategies are investigated for the target distance $l = 100$ µm: OnOff 76°, OnOff 35° and MinDev. The choice of these strategies is similar to the previous section, i.e. the α_0 values of the OnOff strategy optimise T ($\alpha_0 = 76°$) and D ($\alpha_0 = 35°$) in numerical simulations. These α_0 values are larger than the ones for $l = 30$ µm which shows that the target distance has an important influence on the performance of different control strategies. OnOff with minimal α_0 (corresponding to $\alpha_0 = 13°$ for $l = 30$ µm) and LinScl are disregarded as there was no additional benefit from these strategies.

The measured trajectories (Fig. 4.7) show similar features as for smaller l (cf. Fig. 4.4). Trajectories resulting from an OnOff strategy show a combination of active and passive intervals, with the fraction of passive ones increasing for smaller α_0. When the AP is controlled with MinDev, the trajectories seem to be mainly passive, however they are concentrated close to the ideal path which shows the advantage of the MinDev strategy in minimising D.

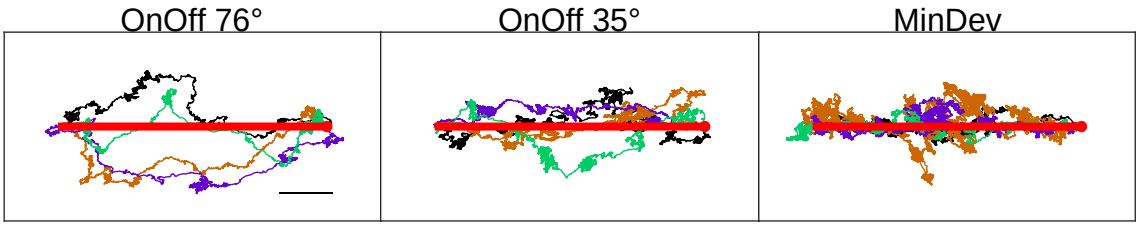

Figure 4.7: Experimental trajectories for a target distance $l = 100$ µm and three different control strategies. The target area and ideal path are shown as a red circle and line, respectively. Scale bar is 20 µm. [1]

The quantification of the trajectories using the figures of merit is shown in Figs. 4.8a to 4.8d. Clearly, differences between the control strategies are enhanced for the larger target distance, especially regarding D, which is much smaller for MinDev than for the other strategies. In case of the MinDev strategy, the experimental standard deviation varies strongly between the different figures of merit. It becomes very small for D ($\approx 40\%$) and, in contrast, is nearly as large as the mean value for T, E and S. Although large standard deviations might result from unidentified error sources in the experiments or an insufficient number of repetitions (17 per data point), the small standard deviation in D shows that the MinDev strategy is an efficient method to guide an AP along a predefined path.

When comparing the performance of the investigated strategies (Fig. 4.8e), it becomes obvious that the optimisation with respect to a certain figure of merit always goes along with an expense towards others. For example, OnOff 76° leads to very efficient navigation with respect to T and S, but D becomes large. MinDev on the other hand leads to small D while all other figures of merit are worse than for the other strategies.

4.4 Summary

The navigation of self-propelling micron-sized objects can play an important role for a variety of applications such as drug delivery in biomedical systems. Especially when resources are limited, e.g. due to the lifetime of carrier and cargo or the available energy for self-propulsion, efficient navigation is relevant.

In this chapter, I showed that control strategies can be employed to steer active Brownian particles towards a target. This does not require the ability to influence the swimming direction of a particle, but it is sufficient to modulate the amplitude of its self-propulsion depending on the orientation which changes due to rotational diffusion.

The efficiency of the navigation crucially depends on the control strategy and on the resources that are monitored. In the presented experimental and numerical results, control strategies always have strengths and weaknesses. The optimisation towards one aspect of the navigation performance, such as the time needed to reach

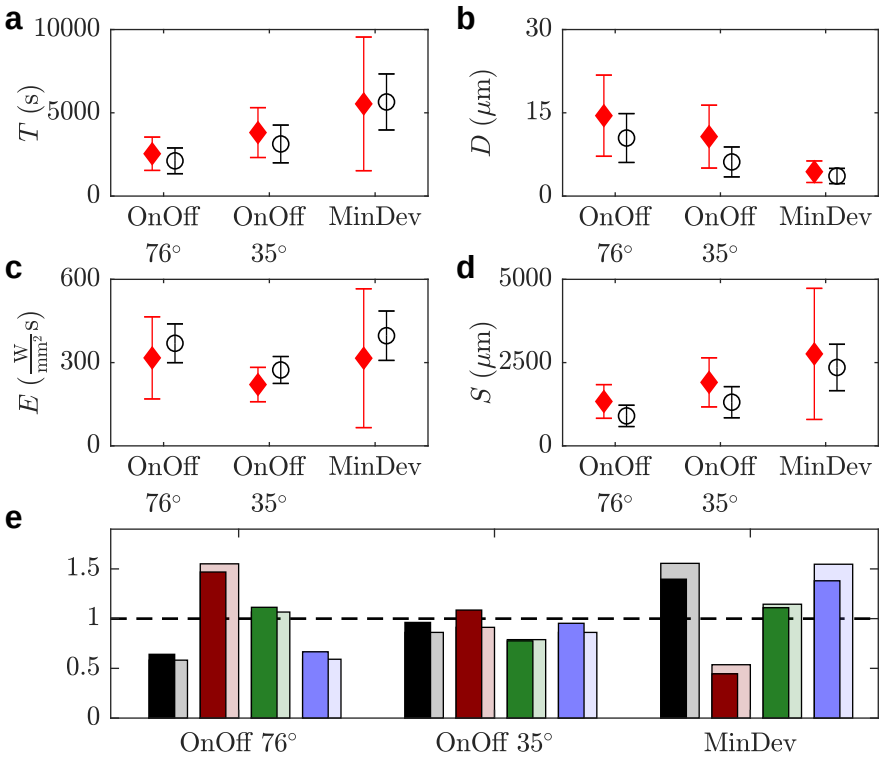

Figure 4.8: Navigation performance with target distance $l = 100$ µm.
a-d Figures of merit T, D, E and S obtained from experiments (red) and numerical simulations (black). Error bars correspond to the standard deviation of different repetitions. **e** Renormalised figures of merit $\widetilde{T}$ (black), $\widetilde{D}$ (red), $\widetilde{E}$ (green) and $\widetilde{S}$ (black). Filled bars correspond to experiments and transparent bars to numerical simulations. The dashed line indicates the average of all strategies. Extended from [1].

the target, always goes along with a degradation towards others. In addition, the performance of a control strategy depends on the parameters of the task, e.g. the distance over which the particle has to be navigated. Accordingly, the suitable choice of a control strategy strongly depends on the conditions and limitations in the specific system.

Chapter 5

Self-organisation of active Brownian particles by quorum sensing

The spontaneous self-organisation into complex structures can be found in living systems of all length scales. Some well-known examples are the formation of flocks of birds, schools of fish and also colonies of bacteria. A prerequisite for such collective behaviour is the ability of the group members to communicate[1] and in turn coordinate their actions. In groups of animals, e.g. fish, birds or insects, communication is achieved by various mechanisms, such as visual [129] or acoustic [130] perception, and the individual's reaction is determined from complex internal processing of the acquired information. In contrast, communication in colonies of bacteria is achieved by means of biochemical signalling, called quorum sensing [131]. Each cell releases signalling molecules (autoinducers) and detects the concentration in its surroundings. Obviously, the local concentration increases with the number of bacteria releasing molecules and, thus, this mechanism allows the individuals to measure the local population density and adjust their behaviour accordingly.

Quorum sensing was first reported in the bioluminescent species Aliivibrio fischeri which symbiotically colonise for example the light organ of the squid Euprymna scalopes, but can also be found in seawater [132]. When the population density of these bacteria is sufficiently large, i.e. the detected concentration of signalling molecules exceeds a certain threshold, a reaction of the individual bacteria is triggered and they start to luminesce [133]. The example of luminescence also illustrates the importance of coordination for bacteria. While luminescence of individual or few bacteria is a waste of resources and does not yield a macroscopic effect, at the high population density inside the light organ of the symbiont, the light emission is strong enough to imply a practical use for the host [134].

Meanwhile, quorum sensing has been found to regulate many different aspects of bacterial behaviour, for example the secretion of virulence factors [135], biofilm formation [136] and the motility [133, 137]. The latter can for example play an important role in early phases of colonisation. Although much is known about

[1] In this context, any signalling mechanism that allows individuals to acquire information about the neighbours in their surroundings is considered as communication.

the molecular processes involved in quorum sensing systems and it is possible to genetically suppress quorum sensing as a whole, it remains difficult to precisely tune the response of bacteria. Therefore synthetic active Brownian particles (APs), whose motility can be adjusted individually, can serve as a versatile model system as all relevant parameters can be controlled.

In this chapter, I will present the implementation of quorum sensing interactions into a system of more than 100 APs. Such interaction induces the formation of clusters at conditions where no phase separation in systems of permanently active particles can be observed. Additionally, small modifications of the interaction can also be used to influence the shape of the resulting clusters.

5.1 Mapping quorum sensing to a system of active Brownian particles

In a colony of bacteria, quorum sensing is achieved by each individual continuously releasing and detecting signalling molecules. As these molecules spread by diffusion, bacterium i senses the time-dependent concentration

$$c_i(t) = \widetilde{c} \sum_{j \neq i} \frac{\sigma}{r_{ij}(t)} \exp\left(-\frac{r_{ij}(t)}{\lambda}\right), \tag{5.1}$$

with the linear size σ of a bacterium, corresponding to the diameter of an AP, and the distance r_{ij} between bacteria i and j. The exponential term accounts for the decay of the concentration profile on a length scale $\lambda = \sqrt{D_\mathrm{C}\tau}$, with finite lifetime τ and diffusion constant D_C of the signalling molecules, which limits the interaction range. The constant pre-factor $\widetilde{c} = \gamma/(4\pi D_\mathrm{C}\sigma)$ is proportional to the rate γ at which individuals release molecules. In the following, all concentrations are given in units of $\widetilde{c}$ which removes the dependence on the choice of γ and D_C. Equation (5.1) assumes that the concentration profile is quasi-static, i.e. that it adapts instantaneously to positional changes. In the experimental system, this is justified as the dynamic of APs is slow compared to the diffusive spreading of typical signalling molecules such as N-acyl homoserine (AHL) with $D_\mathrm{C} \approx 500\ \mu\mathrm{m}^2/\mathrm{s}$ [138]. In general, however, this assumption is not always valid as some species of bacteria can reach velocities much larger than the swimming velocity of APs in the experimental system [139].

For the application of quorum sensing in a system of APs, the hypothetical concentration of signalling molecules is computed for each AP using Eq. (5.1) and the positions of all APs in the system. This is shown in Figs. 5.1a and 5.1b for a typical distribution of APs and decay length $\lambda = 10\sigma$, with the diameter σ of an AP. As expected, c is largest in the centre of the group where the local density of APs is highest and distances between particles are small. The behavioural response to the population density is implemented as a change of the AP motility given by

$$v_i(c_i) = v_0 \cdot \Theta(c_\mathrm{th} - c_i), \tag{5.2}$$

with the Heaviside step function Θ and the threshold concentration c_{th}. According to this rule, APs are motile (red) when the concentration is low and become non-motile (blue) when the concentration exceeds the threshold value (Figs. 5.1c and 5.1d). The application of a sharp threshold in the motility, rather than a smooth transition between $v = v_0$ and $v = 0$, is motivated by the behaviour of quorum sensing bacteria which typically switch between two states when a threshold concentration is exceeded [133, 137].

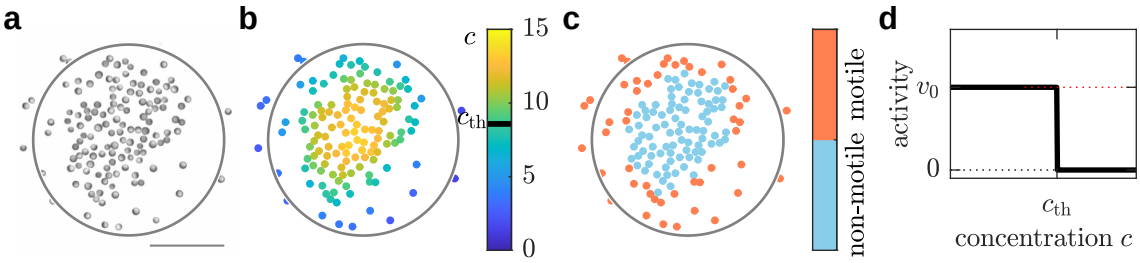

Figure 5.1: Quorum sensing in APs. **a** Snapshot of an experiment with applied quorum sensing interaction. Scale bar is 50 µm. **b** Calculated concentrations c computed for each AP according to Eq. (5.1) with $\lambda = 10\sigma$. **c** AP activity according to the quorum sensing rule shown in **d** with $c_{\mathrm{th}} = 8.6\widetilde{c}$. **d** Dependence of the AP activity on the concentration c. [2]

5.2 Methods

5.2.1 Experimental parameters

The APs in the experiments have a diameter of $\sigma = 4.4$ µm and a 30 nm carbon coating on one hemisphere. The sample cells have a thickness of 200 µm and are heated to $T = 25°$ C, which is ≈ 9 K below the critical temperature of the water/lutidine mixture. In this case, the dynamics of APs are different to the previous chapter. Again, the motion is restricted to the x-y-plane due to gravitation, but the change of the AP orientation by rotational diffusion depends now on its swimming conditions. When an AP is self-propelling, hydrodynamic effects align the orientation parallel to the substrate and its rotation is restricted to 2D. Without activity, the AP can still rotate in 3D, however, this case can be neglected because the orientation does not affect the particle motion when no self-propulsion is present.

Self-propulsion is achieved by steering a laser beam with beam waist $w = 5$ µm to the centre of APs. The intensity on the particle, averaged over time and particle area, is set to $I = 0.2$ W/mm^2 which corresponds to the velocity $v_0 = 0.2$ µm/s. From the mean-squared displacement in entirely passive or active experiments, the translational and rotational diffusion constants were determined to $D_{\mathrm{T}} = (0.0208 \pm 0.0012)$ µm^2/s and $D_{\mathrm{R}} = (112.6 \pm 26.1)^{-1}$ 1/s, respectively.

For the implementation of quorum sensing, AP positions are acquired at a rate of 2 Hz. The corresponding intended AP activities are calculated following the procedure in the previous section and the laser intensity is adjusted accordingly. A circular confinement with radius $R = 65$ µm and reflective boundary conditions is used to keep the average density, i.e. number of APs, in the system constant. This is realised by adding an offset of 2.6 µm to the position of the laser beam such, that the local intensity gradient on the AP leads to reorientation towards the centre of the confinement. As this process is not instantaneous, APs are still able to leave the confinement before reorienting and re-entering the confinement with their orientation pointing towards the centre. Because such events abruptly change the concentration sensed by other APs, all particles that leave the confinement by less than 10 µm are taken into account for the summation according to Eq. (5.1). Typically, this distance is enough for APs to adapt their swimming direction. On average, $N = 122$ APs are inside the confinement which corresponds to a density $\rho_0 = 0.0092\ 1/\mu\text{m}^2$ ($\approx 15\%$ of close packing). To account for varying particle numbers, both during, but more importantly between different measurements, the concentration is also adjusted to the current number of APs (see Section 5.2.3).

In order to obtain experimental data with similar starting conditions, each repetition of the experiments starts by collecting all APs in the central region of the confinement. This is important to cancel out any bias from the previous measurement, e.g. when a cluster has formed close to the boundary of the confinement. Then, a phase of Brownian diffusion (typically 600 s) allows aggregates, which may have formed during the collection of APs, to dissolve. After the quorum sensing interaction is initialised, the system equilibrates for 30 min before data is taken, to ensure that steady-state conditions are reached.

5.2.2 Numerical simulations

Numerical results are obtained from the discrete integration of the overdamped coupled equations of motion of the APs (cf. Eqs. (2.12) and (2.13)). Steric interactions between APs are modelled with the repulsive Weeks-Chandler-Anderson potential

$$U(r_{ij}) = 4\epsilon \left[\left(\frac{\sigma_{\text{wca}}}{r_{ij}} \right)^{12} - \left(\frac{\sigma_{\text{wca}}}{r_{ij}} \right)^{6} + \frac{1}{4} \right], \tag{5.3}$$

which is cut-off at $r_{\text{cut}} = 2^{1/6}\sigma_{\text{wca}}$. In order to obtain an effective particle diameter $\sigma = 4.4$ µm, the parameters are set to $\sigma_{\text{wca}} = 3.98$ µm and $\epsilon = 100\ k_{\text{B}}T$ [140]. The discrete integration for position $\mathbf{r}_i$ and orientation $\hat{\mathbf{u}}_i = (\cos(\theta), \sin(\theta))$ of particle i then reads

$$\mathbf{r}_i(t+\tau) = \mathbf{r}_i(t) + \left(v_i(c_i)\hat{\mathbf{u}} - \frac{D_{\text{T}}}{k_{\text{B}}T} \nabla_i U\Big(\Big\{ \mathbf{r}_j \Big\} \Big) \right) \cdot \tau + \boldsymbol{\xi}_{\text{T},i} \cdot \sqrt{\tau}, \tag{5.4}$$

$$\theta_i(t+\tau) = \theta_i(t) + \xi_{\text{R},i} \cdot \sqrt{\tau}, \tag{5.5}$$

with normal distributed, uncorrelated variables $\boldsymbol{\xi}_{\mathrm{T},i}$ and $\xi_{\mathrm{R},i}$, characterised by zero mean and component-wise variance $2D_{\mathrm{T}}$ and $2D_{\mathrm{R}}$, respectively. The time step is set to $\tau = 40$ ms and the other parameters to the experimentally determined values $D_{\mathrm{T}} = 0.02$ µm^2/s, $D_{\mathrm{R}} = (1/120)$ 1/s, and $v = 0$ or $v = 0.2$ µm/s, depending on the concentration c. Although concentration and motility are updated every time step, changes of the motility are only recorded every 12 time steps, corresponding to 480 ms, to be comparable to the experimental data with time step 500 ms.

Because APs can reorient instantaneously in the numerical simulations, the experimental boundary conditions are modelled by using $N = 132$ APs in a confinement with radius $R = (65{+}10)$ µm. In addition, simulations with periodic boundary conditions are employed to exclude the possibility that the observed effects are an artefact of the reflective boundary conditions.

5.2.3 Adjustment of the concentration

In experiments and numerical simulations, the activity of an AP depends on the concentration c of hypothetical signalling molecules at the position of the AP, compared with a threshold concentration c_{th}. However, c changes with the particle number N, the decay length λ and the system size R. In order to make results obtained under different conditions more comparable, a reference concentration can be used to adjust either c or c_{th}.

Therefore, a particle in the centre of the confinement, i.e. at $\mathbf{r} = 0$, is considered. This particle senses the concentration, generated by all other particles j,

$$c(0) = \int_0^R r\,dr \int_0^{2\pi} d\phi \sum_j \delta(|\mathbf{r} - \mathbf{r}_j|) \frac{\widetilde{c}\,\sigma}{r} \exp\left(-\frac{r}{\lambda}\right). \tag{5.6}$$

Assuming a homogeneous particle distribution inside the confinement, without an overlap to the particle in the centre, the sum can be expressed as

$$\sum_j \delta(|\mathbf{r} - \mathbf{r}_j|) \approx \bar{\rho}\,\Theta(r - \sigma)\,\Theta(R - r), \tag{5.7}$$

with $\bar{\rho} = N/(\pi R^2)$ being the average density[2]. Equation (5.6) is then calculated to

$$\begin{aligned} c(0) &= \int_\sigma^R dr \int_0^{2\pi} d\phi\, \widetilde{c}\,\sigma\,\bar{\rho} \exp\left(-\frac{r}{\lambda}\right) \\ &= \widetilde{c}\,\frac{2\,N\,\lambda}{R^2}\left(\exp\left(-\frac{\sigma}{\lambda}\right) - \exp\left(-\frac{R}{\lambda}\right)\right). \end{aligned} \tag{5.8}$$

This reference concentration $c(0) = c_0(N, \lambda, R)$ is used to adjust c to variations of the particle number N, and to keep the threshold concentration constant when varying other parameters.

[2] When one particle is fixed, the density would be slightly smaller in the rest of the confinement, however, this deviation is less than 0.5% for the experimental configuration.

5.3 Results

5.3.1 Enhanced cluster formation

Without quorum sensing interaction between particles, both motile and non-motile APs are equally distributed within the circular confinement. In contrast, when the interaction is turned on, APs are preferentially located near the centre (cf. Fig. 5.1a). The degree of this inhomogeneity strongly depends on the value of the concentration threshold c_{th}. In order to quantify this effect, the time-averaged particle density ρ is calculated as shown in Figs. 5.2a to 5.2d for four different threshold values $c_{\mathrm{th}} = [5.9, 7.3, 8.6, \infty]\,\widetilde{c}$ and decay length $\lambda = 10\sigma$. In the following, a cluster is defined as a region where the local density deviates sufficiently from the average density ρ_0 in the confinement, i.e. when $\rho/\rho_0 > 1.2$. According to this definition, clusters can be packed rather loosely, in contrast to clusters in phase separated systems of permanently active particles, where the cluster density is near to close packing [104, 106]. The formation of clusters is only observed within a certain range of threshold values c_{th} (at constant λ), for values outside this range, the particle distribution in the confinement remains homogeneous. When c_{th} is smaller than the concentration sensed by every AP, the situation is equivalent to a suspension of passive particles and obviously does not lead to the formation of clusters. At intermediate c_{th}, APs can sense concentrations below and above the threshold and cluster formations is observed. In this regime, clusters become more compact with increasing c_{th}, i.e. the density ρ increases while the cluster shrinks (Figs. 5.2a to 5.2c). When c_{th} is further increased, cluster formation is prevented because all APs sense sub-threshold concentrations and are permanently active (Fig. 5.2d). In this situation, the effects of the quorum sensing interaction vanish.

In previous studies, experiments and numerical simulations have shown that systems of permanently active particles can phase separate into clusters surrounded by a dilute gas [27, 103–107]. However, this phase separation only happens when swimming velocity and particle density in the system are sufficiently large [107]. In Fig. 5.3a the onset of phase separation, depending on the area fraction Φ and the Peclet number $Pe = 3v_0/(\sigma D_{\mathrm{R}})$, is shown based on numerical data (blue circles, data from [141]). The experimental conditions in this chapter (red cross) are far from this regime which demonstrates that, indeed, the quorum sensing interaction between APs leads to the formation of clusters. This is also in agreement with the observation that no clusters exist when c_{th} becomes too large.

The mechanism of cluster formation in systems of quorum sensing APs is similar to the one known from permanently active particles. In this case, an AP gets blocked and cannot continue to move in its propulsion direction when it collides with another AP or an already existing cluster. Before it can detach from the cluster, it needs to reorient by rotational diffusion which takes a time $\sim 1/D_{\mathrm{R}}$. If another AP arrives at the cluster within this time, the cluster will grow until it reaches a steady-state size which is determined by the rates of APs joining and leaving the cluster [106].

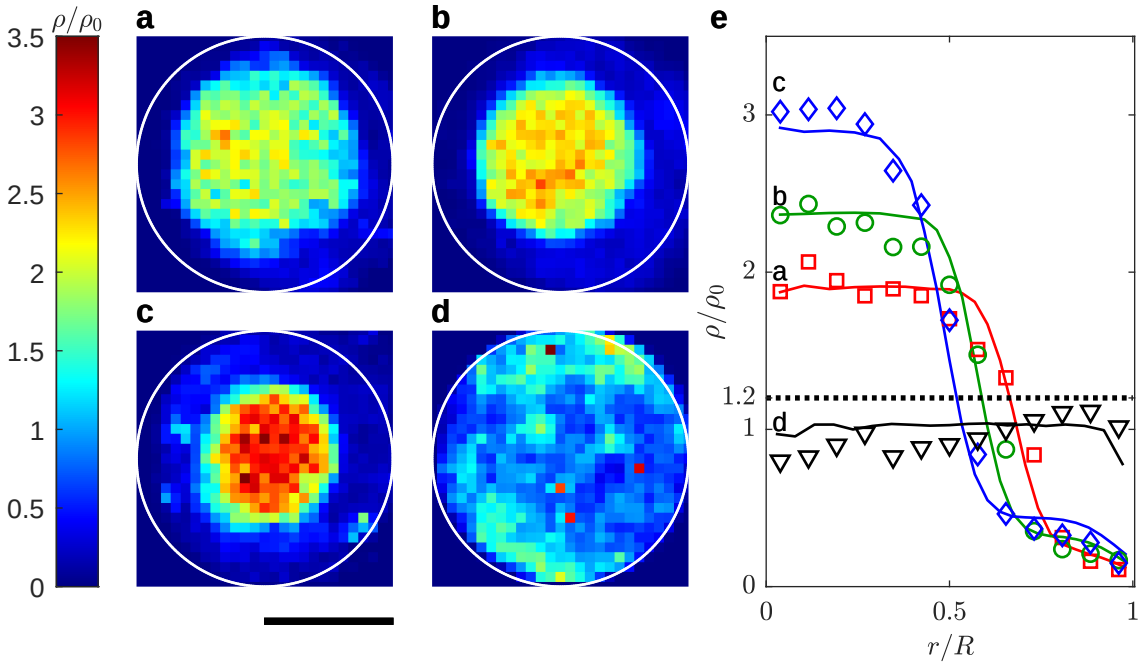

Figure 5.2: Cluster formation by quorum sensing. **a-d** Normalised steady-state particle density ρ/ρ_0 for different concentration threshold values $c_{\mathrm{th}} = [5.9, 7.3, 8.6, \infty]\,\widetilde{c}$, obtained from experiments with $\lambda = 10\sigma$. Scale bar is 65 µm. **e** Radial density distribution for the threshold values in **a-d** obtained from experiments (symbols) and numerical simulations (solid lines). When the density exceeds $\rho/\rho_0 = 1.2$ (dotted line), a cluster has formed. [2]

Considering APs interacting via quorum sensing, APs approaching a dense region, i.e. a cluster, will stop their active motion as a consequence of the interaction. Because this does not require contact between APs, the resulting clusters can be dilute. Another consequence of the quorum sensing interaction is an increase of the requirements for an AP to leave a cluster. As before, it is necessary that the AP reorients, but in addition the AP also needs to move away from the cluster by translational diffusion before it becomes active again. Accordingly, the flux of APs leaving the cluster is reduced which, in turn, allows a lower flux of APs joining the cluster in the steady-state. This explains why cluster formation can still be observed at swimming velocities and densities substantially lower than required for permanently active particles (Fig. 5.3a).

Besides the extension of the parameter range leading to the formation of clusters, the quorum sensing interaction between APs also changes the structure of the cluster. This can be seen in snapshots of numerical simulations (Figs. 5.3b to 5.3d) with 1000 APs and periodic boundary conditions. Here, the swimming velocity of APs is increased to $4v_0 = 0.8$ µm/s and the average density in the system to $4.4\rho_0$ (green square in Fig. 5.3a). As expected, permanently active particles form a dense cluster surrounded by a dilute gas (Fig. 5.3b). When APs additionally interact via quorum sensing, a crystalline core of non-motile APs forms in the centre of the cluster.

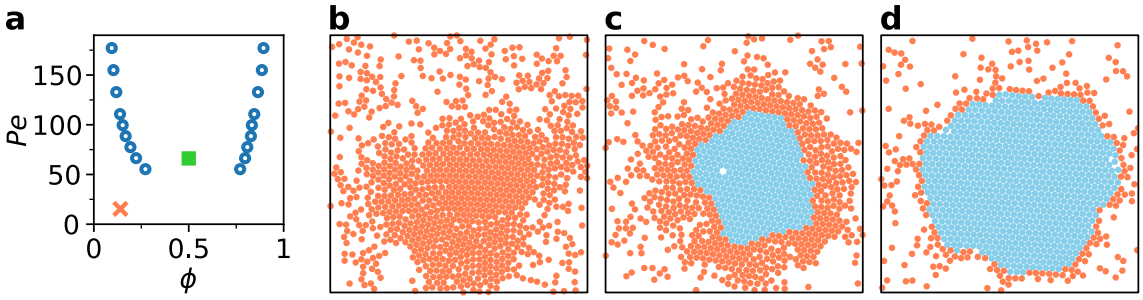

Figure 5.3: Cluster formation at large density and velocity. **a** Binodal line of the phase separation of APs with permanent activity (blue circles, numerical data taken from [141]) for area fraction Φ and Peclet number $Pe = 3v_0/(\sigma D_\mathrm{R})$. The experimental conditions in this chapter are marked as a red cross. **b-d** Numerical results for 1000 APs with velocity $4.4v_0 = 0.8$ µm/s, density $4.4\rho_0$ (green square in **a**) and periodic boundary conditions for **b** APs without quorum sensing interaction (corresponding to $c_\mathrm{th} = \infty$) and **c**,**d** with $c_\mathrm{th} = 13.5\widetilde{c}$ and $c_\mathrm{th} = 10\widetilde{c}$, respectively, and $\lambda = 2.5\sigma$. Blue (red) circles correspond to passive (active) APs. [2]

This core grows with decreasing c_th, until it reaches the cluster edges (Figs. 5.3c and 5.3d). This happens because the non-motile particles inside the cluster are compressed by the motile ones pushing from the edges. Further reducing c_th also allows APs without direct contact to the cluster to become passive and the crystalline region vanishes.

5.3.2 Phase behaviour of quorum sensing particles

Further details about the cluster formation in presence of quorum sensing can be obtained from a quantitative analysis of the observed clusters. Therefore, the concentration threshold c_th and decay length λ are systematically varied in experiments and numerical simulations. Information about the properties of a cluster can be extracted by fitting the radial density profiles to

$$\rho(r) = \frac{\rho_\mathrm{c} + \rho_\mathrm{g}}{2} - \frac{\rho_\mathrm{c} - \rho_\mathrm{g}}{2} \tanh\left(\frac{r - r*}{2w_\mathrm{int}}\right), \tag{5.9}$$

with the cluster density ρ_c, the gas density ρ_g, the radius $r*$ of the cluster and the width w_int of the cluster interface. Additional theoretical results are derived from a mean-field theory developed by Andreas Fischer and Thomas Speck (University of Mainz) [2]. In Fig. 5.4a the complete phase diagram, obtained from numerical simulations, is shown. Cluster formation is observed for any λ, but only within a well-defined range of c_th-values. When c_th is too small (large), all APs sense concentrations above (below) the threshold value and are passive (active), marked by the blue (red) area. Within the parameter range leading to cluster formation, the cluster density ρ_c is colour-coded. The limits of this range are obtained from numerical simulations, however, the lower limit is also in agreement with the result of

the mean-field theory. When the decay length λ increases, each AP senses higher concentrations because the contribution of each of its neighbours increases and, in addition, more neighbours contribute. As a consequence, the c_{th}-range leading to cluster formation is shifted to larger values. Considering an increase of c_{th} at constant λ, the clusters become denser and smaller (Figs. 5.4b and 5.4c). Experimental (filled red symbols) and numerical (open black symbols) data show good agreement, whereas the mean-field theory (blue line) only reproduces the general trend of the shrinking because if neglects fluctuations. In Fig. 5.4d the decay length λ is varied while keeping the threshold value $c_{\mathrm{th}} = 1.2c_0$ constant with respect to the reference concentration c_0 (Eq. (5.8)). Especially at small λ, fluctuations play an important role because fewer neighbours contribute to the concentration an AP senses. Accordingly, the deviation between mean-field theory and results obtained from experiments and numerical simulations becomes smaller with increasing decay length λ.

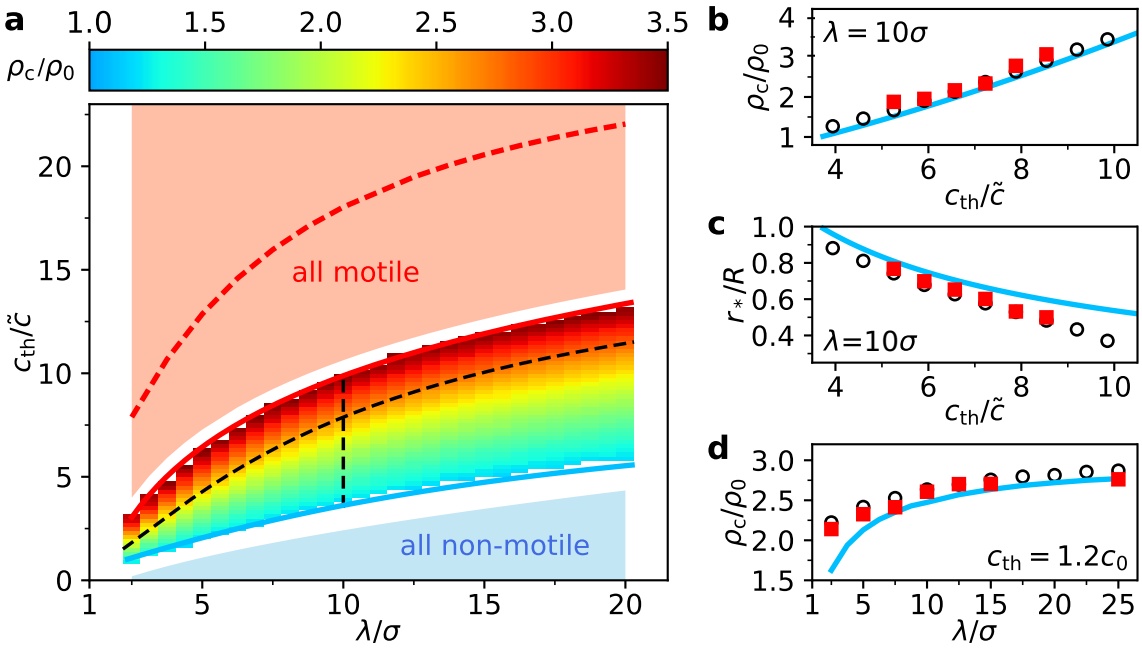

Figure 5.4: Dependence of the cluster formation on concentration threshold c_{th} and decay length λ. **a** Phase diagram obtained from numerical simulations. Cluster formation is observed within the colour-coded region enclosed by solid red (upper limit of c_{th} leading to stable clusters) and blue (lower limit of c_{th} from mean-field theory) lines. Experimental data in **b-d** were taken along the black dashed lines. The red dashed line indicates the theoretical value of c_{th} at which close packing is reached. **b**,**c** Cluster density ρ_c and cluster radius $r*$ vs. c_{th} for constant $\lambda = 10\sigma$ (vertical black dashed line in **a**). **d** Cluster density ρ_c vs. decay length λ for adjusted $c_{\mathrm{th}} = 1.2c_0$ (cf. Eq. (5.8)). In **b-d** experimental data is shown as filled red symbols, numerical data as open black symbols and results of the mean-field theory as solid blue lines. [2]

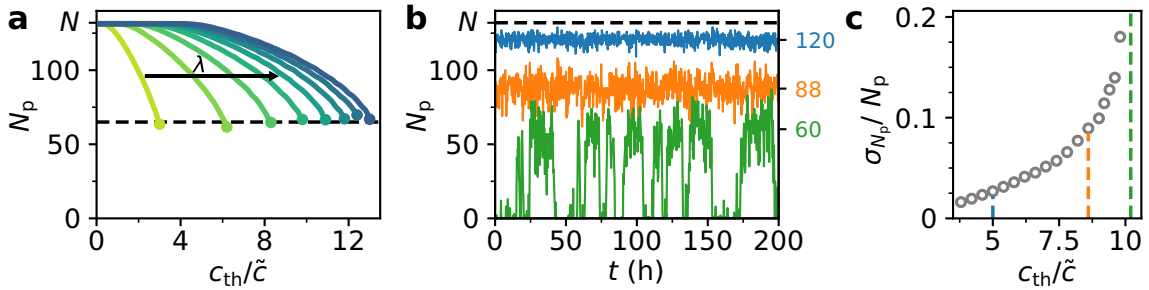

Figure 5.5: Limit of cluster stability. **a** Averaged number of passive particles $\langle N_\mathrm{p} \rangle$ vs. threshold concentration c_th for decay lengths $\lambda = [2.5, 5, 7.5, 10, 12.5, 15, 17.5, 20]\,\sigma$ (left to right) obtained from numerical simulations. Symbols correspond to maximum c_th where cluster formation is observed. As indicated by the dashed line at $N_\mathrm{p} = 65$, clusters become unstable at a similar number of passive particles, independent of λ. **b** Time evolution of N_p for $c_\mathrm{th} = [5, 8.6, 10.2]\,\tilde{c}$ (top to bottom) and $\lambda = 10\sigma$. $\langle N_\mathrm{p} \rangle$ (right axis) includes only frames with existing cluster. **c** Standard deviation σ_{N_p} divided by the mean $\langle N_\mathrm{p} \rangle$ vs. c_th for $\lambda = 10\sigma$ in the range where stable clusters are observed. [2]

The mean-field theory suggests the formation of clusters up to c_th-values that are considerably larger than observed and which correspond to the limit where close packing is reached in the cluster (red dashed line in Fig. 5.4a). This discrepancy can be explained by the shrinking of the cluster for increasing c_th. In this situation, the cluster does not only become smaller and denser, but also the number of passive particles N_p forming the cluster decreases (Fig. 5.5a). When an AP leaves the cluster, it reduces the concentration sensed by other APs in the cluster. This effect can trigger a chain reaction if the concentration drops below c_th for other APs, which becomes more likely for clusters composed of fewer passive particles. For a system of $N = 132$ APs, simulations show that this effect destabilises clusters when the number of passive particles is $N_\mathrm{p} \sim 65$ (dashed line in Fig. 5.5a) independent of λ, which prevents the formation of stable clusters at large c_th. This is also supported by the increasing fluctuations in the number of passive particles (Figs. 5.5b and 5.5c). An increase of the average density ρ_0 in the system reduces the influence of this effect and the maximum cluster density ρ_c is shifted towards close packing [2]. In addition, the fraction of passive particles needed for stable clusters is reduced for larger system sizes [2].

5.3.3 Mechanism of cluster formation

Cluster formation in quorum sensing APs is only observed when the threshold concentration c_th is adjusted such, that both active and passive particles exist. Using numerical simulations, it is found that the coexistence of both kinds of particles is not sufficient to induce clustering and the system remains homogeneous, independent of the mixing ratio. Accordingly, the ability of APs to change their motility is the driving mechanism of cluster formation. In Figs. 5.6a and 5.6b the importance

of motility changes is illustrated. Considering the case of quorum sensing APs, a motile particle (red) approaching a cluster of passive particles (blue) will sense an increasing concentration. When c_{th} is exceeded, the AP becomes passive and joins the cluster. In order to leave the cluster, a passive particle first has to diffuse away from the cluster until its sensed concentration is not sufficient to remain passive anymore. When it becomes active, its orientation determines if it will swim away from the cluster (sketched) or rejoins. In contrast, when particles are lacking the ability to switch their motility, the active particle is not joining the cluster. However, the cluster of passive particles will still dissolve due to diffusion.

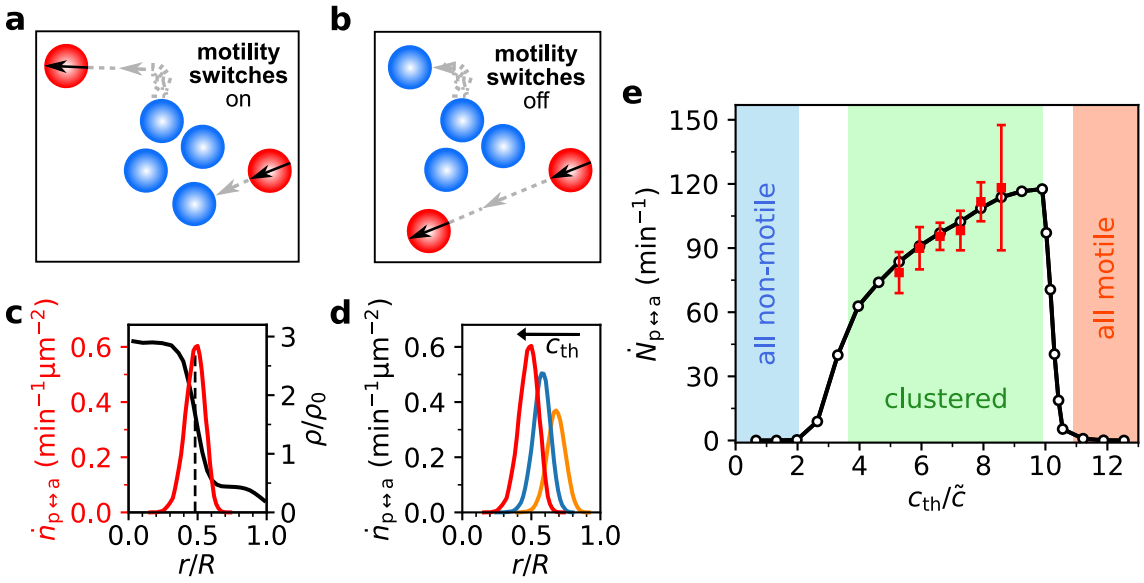

Figure 5.6: Motility switches. **a** When an AP (red) approaches the cluster of passive particles (blue) and its sensed concentration increases above c_{th}, it becomes passive and joins the cluster. Similarly, a passive particle can diffuse away from the cluster and become active. If it is oriented away from the cluster, it will leave it. **b** Without motility switches, the AP (red) will swim past the cluster. **c** Radial density profile $\rho(r)$ (black) and motility change density $\dot{n}_{\mathrm{p}\leftrightarrow\mathrm{a}}(r)$ obtained from simulations with $c_{\mathrm{th}} = 8.6\widetilde{c}$ (red) and $\lambda = 10\sigma$. The dashed line marks the centre of the interface which coincides with the maximum of motility changes. **d** Motility change density for three different threshold values $c_{\mathrm{th}} = [5.9, 7.3, 8.6]\,\widetilde{c}$ and $\lambda = 10\sigma$. **e** Rate of motility changes $\dot{N}_{\mathrm{p}\leftrightarrow\mathrm{a}}(r)$ vs. c_{th} in experiments (filled symbols) and numerical simulations (open symbols) for $\lambda = 10\sigma$. Error bars correspond to the standard deviation of different measurements. [2]

Motility changes can be quantified by the motility change density $\dot{n}_{\mathrm{p}\leftrightarrow\mathrm{a}}(r)$ which describes the number of change events per time within a ring at distance r from the centre of the cluster. $\dot{n}_{\mathrm{p}\leftrightarrow\mathrm{a}}(r)$ becomes largest at the interface between cluster and dilute gas as shown in Fig. 5.6c for simulations with $c_{\mathrm{th}} = 8.6\widetilde{c}$ and $\lambda = 10\sigma$. In this region, configurational changes are most pronounced leading to sufficient changes of the sensed concentration. Accordingly, when increasing c_{th}, the radial position of

the distribution shifts to smaller radii as the cluster shrinks. In addition, the height of the peak increases (Fig. 5.6d). Integrating $\dot{n}_{\mathrm{p}\leftrightarrow\mathrm{a}}(r)$ over the whole system, one receives the total rate of motility changes $\dot{N}_{\mathrm{p}\leftrightarrow\mathrm{a}}$ which is shown in Fig. 5.6e as a function of the threshold concentration c_{th} for experimental (red filled symbols) and numerical (open black symbols) data.

Cluster formation is only observed if the number of motility switches reaches a certain level (left edge of the green area), which is nearly independent of the decay length λ [2]. When c_{th} is increased, the cluster density increases and, thus, the deviation of the particle distribution compared to thermal equilibrium. Accordingly a growing amount of motility control is required to sustain the non-equilibrium conditions which manifests in an increasing switching rate $\dot{N}_{\mathrm{p}\leftrightarrow\mathrm{a}}$. When clusters become unstable due to large values of c_{th}, $\dot{N}_{\mathrm{p}\leftrightarrow\mathrm{a}}$ drops abruptly. For small λ, the motility switching rate is generally larger and the decrease in the regime of unstable clusters is less abrupt, because the impact of fluctuations is stronger [2]. However, the observed c_{th}-dependence of the switching rate is similar for all λ which demonstrates the importance of switching dynamics for cluster formation in APs interacting via quorum sensing.

5.3.4 Influencing the structure and shape of quorum sensing clusters

In order to further investigate the collective behaviour of quorum sensing APs, modifications of the original response can be considered. So far, an AP switches its motility from active to passive upon sensing a concentration above a threshold value c_{th}. In addition, now a second concentration threshold $c_{\mathrm{th},2} > c_{\mathrm{th}}$ is introduced, above which the AP re-activates its propulsion, i.e. $v(c > c_{\mathrm{th},2}) = v_0$ [142]. Accordingly, APs are only passive within an intermediate range of sensed concentrations. As shown in Fig. 5.7a this second threshold leads to a 'ring'-like structure of the resulting cluster. Because APs in the centre of the cluster sense largest concentrations, particles in this region become active and tend to leave it. This reduces the density in the centre until it is not sufficient anymore for APs to sense concentrations above the second threshold. As a consequence, the density in the centre is strongly reduced, but it is still significantly larger than the density of the dilute gas outside the cluster.

Another possibility to modify the response of APs to their environment is the assumption of anisotropic spreading of the signalling molecules. In this situation the concentration profile generated by each AP becomes angle-dependent. This can be implemented as an additional term $f(\Theta)$ in Eq. (5.1) leading to

$$c_i(t) = \widetilde{c} \sum_{j \neq i} \frac{\sigma}{r_{ij}(t)} \exp\left(-\frac{r_{ij}(t)}{\lambda}\right) f(\Theta_{ij}), \tag{5.10}$$

with Θ_{ij} the angle between the x-axis and the vector connecting particles i and j. The choice $f(\Theta) = \cos^4(\Theta)$ leads to an elliptical shape of the cluster parallel

to the x-axis (Fig. 5.7b), which is rotated by 90° for $f(\Theta) = \sin^4(\Theta)$ (Fig. 5.7c). Even almost quadratic clusters can be obtained when the angle-dependent function is changed to $f(\Theta) = \cos^4(2\,\Theta)$.

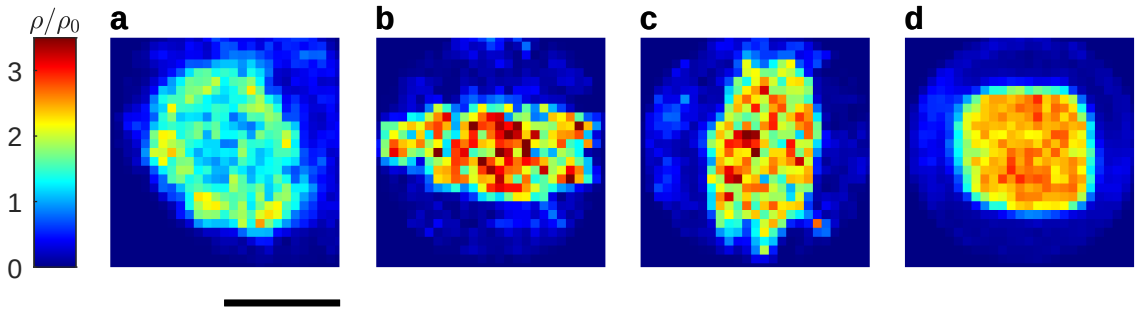

Figure 5.7: Structural changes of quorum sensing clusters. **a** 'Ring'-like structure induced by a second quorum sensing threshold $c_{\mathrm{th},2} > c_{\mathrm{th}}$ above which APs become motile again. **b** Elliptical cluster when concentrations are weighted with $f(\Theta) = \cos^4(\Theta)$. **c** $f(\Theta) = \sin^4(\Theta)$ rotates the elliptical cluster by 90°. **d** Quadratic cluster observed for $f(\Theta) = \cos^4(2\,\Theta)$. Arrows in **b-d** indicate the direction of the x-axis. [2]

5.3.5 Cohesive groups of active particles[3]

APs interacting via quorum sensing form stable clusters at velocities and densities that do not lead to cluster formation in permanently active particles. However, these clusters are not cohesive and, thus, require a surrounding gas of APs which generates a flux towards the cluster. In order to obtain a cohesive group of APs, it is necessary to modify the interaction such, that APs preferentially move towards the group. In the following, it will be shown that this behaviour can be achieved by switching the AP motility based on visual perception [3], rather than on the local density. Note that it is not necessary to introduce (pairwise) attractions or active reorientations as in previous studies [49, 143].

Motivated by vision, APs only perceive neighbours within a vision cone V^α with half angle α to their front (Fig. 5.8a) [144]. The perception of AP i is then calculated according to

$$P_i = \sum_{j \in V_i^\alpha} \frac{1}{2\pi r_{ij}}, \tag{5.11}$$

with the distance r_{ij} between particles i and j. The choice of a distance-dependent perception function is inspired by the metric interaction in midges [33]. In case of unrestricted vision, i.e. $\alpha = \pi$, this perception function reproduces the concentration

[3] Experimental data in this section was taken by Hugo Wendehenne, the theory developed by François Lavergne, my main contribution was the development of the experimental setup. Therefore, I decided to present these results only in a shortened version.

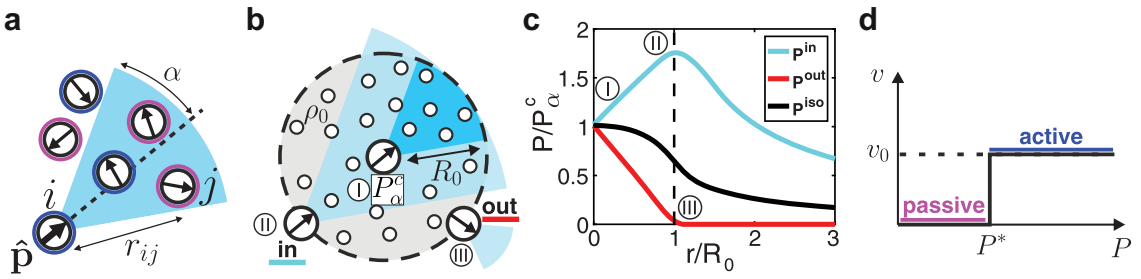

Figure 5.8: Perception-dependent motility. **a** An AP perceives other APs within its vision cone with half angle α (blue area) weighted with the inverse distance between them. **b** Illustration of the perception for three APs at different position within the group. **c** Perception profiles considering a homogeneous particle distribution with radius R_0. The black line corresponds to full vision ($\alpha = \pi$) , cyan and red to vision with $\alpha = \pi/4$ for APs oriented inwards and outwards, respectively. (I), (II), (III) correspond to the APs highlighted in **b**. **d** Dependence of the AP activity on the perception. Adapted from [3].

profiles of quorum sensing with $\lambda = \infty$, however, when $\alpha < \pi$ the interaction between APs becomes non-reciprocal. In Fig. 5.8b a typical AP configuration is sketched where the three highlighted particles (I), (II) and (III) illustrate the effect of restricted vision. (I), located in the centre of the group, perceives only few particles whereas (II), located at the edge and oriented inwards, perceives nearly all members of the group. In contrast, (III), located at the edge and oriented outwards, does not see any member of the group. In Fig. 5.8c the perception P/P^c_α depending on the radial position r within the group is shown for inwards (cyan) and outwards (red) oriented APs with $\alpha = \pi/4$ as well as for isotropic vision ($\alpha = \pi$, black). P^c_α is the perception of an AP with vision angle α located in the centre of a homogeneous group. Depending on the perception P_i of AP i, its motility is given by

$$v_i(P_i) = v_0 \cdot \Theta(P_i - P^*), \tag{5.12}$$

with the Heaviside step function Θ and perception threshold P^* (Fig. 5.8d). Accordingly, APs are passive when their perception is low and become active when their perception exceeds the threshold value. This motility response is the opposite of the response in case of quorum sensing (cf. Eq. (5.2)).

The realisation of experiments with perception-dependent motility requires only small modifications compared to experiments with quorum sensing APs. Obviously, the orientation of APs has to be acquired from the video microscopy image. In addition, the reflective boundary condition is removed. In Fig. 5.9, a time series of experimental snapshots is shown for $\alpha = \pi/4$ and threshold perception $P^* = P^c_\alpha = aN/(\pi^2 R_0)$. This perception threshold corresponds to the hypothetical perception in the centre of a homogeneous group with radius R_0. The initial group ($t = 0$) becomes compact and reaches a steady-state in which dominantly APs in the centre of the group are active (blue), while APs at the edges remain passive (magenta). The group is cohesive and no APs are exchanged with the surroundings.

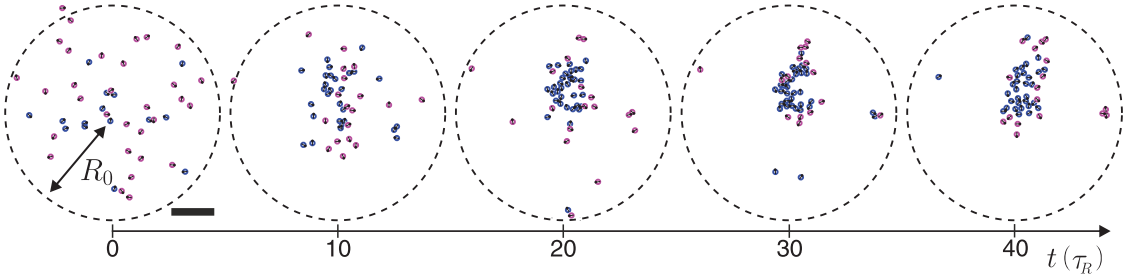

Figure 5.9: Formation of a cohesive group. Time series of experimental snapshots of 75 APs controlled by perception-dependent motility with threshold perception $P^* = P_\alpha^c$. Particles in blue (magenta) are active (passive) at the time of the snapshot. Note that the dashed circles only indicate the initial radius R_0 of the group and do not impose boundary conditions. Scale bar is 40 µm. Adapted from [3].

5.4 Summary

Many species of bacteria rely on quorum sensing to communicate in order to coordinate and synchronise their behaviour within the colony. Although many of the controlled functions cannot be transferred to a system of active Brownian particles, in some species, quorum sensing is crucial for the colonisation as it regulates the bacterial motility [133]. In this situation, active Brownian particles provide an ideal model system because all interaction parameters can be controlled precisely.

In this chapter, I showed that interaction via quorum sensing between active Brownian particles can induce and enhance the formation of clusters. Accordingly, stable clusters are observed at conditions, i.e. swimming velocity and particle density, which are not sufficient to lead to phase separation in systems of active Brownian particles interacting only via steric repulsion. Switches of the particle motility were identified to be the driving mechanism of cluster formation. An increasing cluster density, corresponding to an increasing deviation of the particle distribution to thermal equilibrium, requires a growing number of such motility switches to be sustained. In addition, I presented, that modifications of the quorum sensing response can be used to change the structure and shape of the clusters, resulting in 'ring'-like, elliptical or square clusters.

I also illustrated how the introduction of a non-reciprocal interaction using visual perception produces cohesive groups of particles. While quorum sensing clusters require a flux of particles from a surrounding gas, these groups can exist separated in space because the non-reciprocity hinders particles from leaving the group. Although the employed interaction differs strongly from quorum sensing, also many similarities exist, e.g. the sudden change of motility when a threshold is exceeded or the distance-dependence of the perception which is similar to quorum sensing with an infinite decay length.

As a concluding remark to this chapter I want to mention that further theo-

retical insights to the difference between clustering of active Brownian particles and cluster formation due to quorum sensing have been presented [145]. Although a density-dependent change of the particle motility is responsible in both cases, it was found that the discontinuity in case of quorum sensing drastically changes the phase diagram of cluster formation. This has the consequence that the critical point, which is present in case of phase separation of permanently active particles, vanishes (Fig. 5.10).

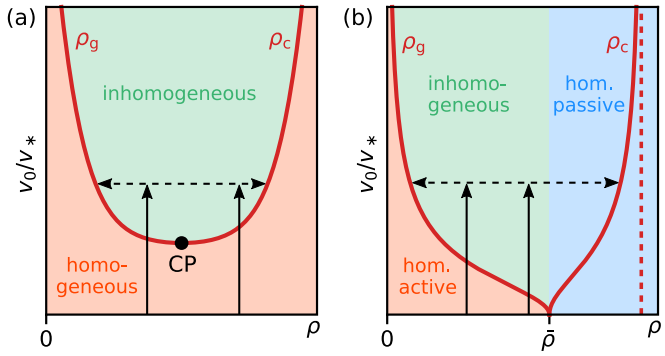

Figure 5.10: Phase diagrams for active Brownian particles (a) and quorum-sensing particles (b). Reprinted figure with permission from [145] (`https://doi.org/10.1103/PhysRevE.101.012601`). Copyright 2020 by the American Physical Society.

Chapter 6

Swirl formation of active Brownian particles with alignment interaction

The phenomenon of self-organisation of individuals into groups is known in many animal species. Among the many possible results of this collective behaviour, three collective states take an outstanding position: swarms, flocks and swirls. These collective states are cohesive and can be distinguished by the order within the group [9]. In swarms the direction of motion of individuals has no global order, in flocks all individuals are aligned and in swirls the group rotates around its centre of mass. The existence of collective states in groups of animals requires that individuals adjust their behaviour, i.e. the direction of motion and the velocity, depending on their neighbours and (possibly) external stimuli. This concept is referred to as social forces or social interactions [7]. In many models, social interactions between individuals are defined by a combination of avoidance, alignment and attraction [9, 46, 51]. In contrast to physical interactions where attraction and repulsion correspond to reciprocal forces between objects or particles, here they typically lead to a reorientation of the individual towards or away from the source of the social force [7]. Based on local (or global) information about the state of the other members of the group, such interactions were found to lead to the formation of swarms, flocks and swirls in numerical simulations [9, 10].

For the members of the group it is important that the collective state of the group is robust against noise and internal or external perturbations. However, it is also necessary that the group can adjust its behaviour depending on environmental conditions and external stimuli, e.g. the presence of a predator [7]. The balance between these competing aspects suggests that collective states are close to a critical point, i.e. near to a transition between ordered and disordered states [54, 55]. Strong indications for the presence of a critical point have been found in starling flocks [36, 42] and swarms of midges [58, 59] by the analysis of position and velocity correlations. In addition, numerical simulations of a model derived from observations in schools of fish show an enhanced susceptibility near the transition from swirl to flock [53]. However, the experimental observation of phase transition between different collective states by a controlled variation of interaction parameters in living

animals is difficult, if not impossible, to achieve. In a group of active Brownian particles, the parameters of a programmed social interaction rule can be precisely adjusted. Therefore, this system allows to obtain further evidence for the connection between collective states and critical phase transitions.

At the beginning of this chapter I will introduce a social interaction rule which is motivated by typical behavioural policies of animals: the desire to stay close to other individuals and the avoidance of collisions. When this rule is introduced to a group of individually controllable active Brownian particles, they self-organise into different collective states whose dynamics and robustness against perturbation will be investigated in the following. I will show that a phase transition between different collective states can be observed upon a variation of interaction parameters and validate that it is critical using the groups susceptibility, as well as finite size scaling and the Landau theory.

6.1 Social interaction between active Brownian particles

The specific social interaction between APs in this chapter is realised by actively reorienting the particles towards a preferred swimming direction $\hat{\mathbf{d}}$ which depends on the particle configuration in the surroundings of each AP. The motivation of the presented rule, which will be explained in detail in the following, is that APs try to form a cohesive group by moving towards their neighbours. However, swimming directly to the centre of the group, where the particle density is largest, also leads to a high number of collisions and the movement of individuals can be prevented. Therefore, APs misalign their swimming direction by a fixed angle to either side from the centre of the group. The choice of the two possibilities is then based on the orientation of close neighbours to increase local order and, thus, also reduce the amount of collisions.

To realise this behavioural policy, AP i senses its neighbours within its field of vision $V_i^{\alpha,R}$, defined by vision angle α and range R, centred around its orientation $\hat{\mathbf{u}}$ (Fig. 6.1a). In the first step, the AP determines the direction $\mathbf{P}_i$ to the centre of mass of the (visible) group by sensing the positions $\mathbf{r}_j$ of all neighbours closer than the position detection range R_p, i.e. $|\mathbf{r}_i - \mathbf{r}_j| \leq R_\mathrm{p}$, according to

$$\mathbf{P}_i = \frac{1}{n_\mathrm{p}} \sum_{j \in V_i^{\alpha,R_\mathrm{p}}} (\mathbf{r}_j - \mathbf{r}_i)\,, \tag{6.1}$$

with n_p the number of sensed neighbours in $V_i^{\alpha,R_\mathrm{p}}$ (dashed orange region in Fig. 6.1a). Because the AP tries to avoid the centre of the group, this leads to two possible swimming directions

$$\hat{\mathbf{d}}_i^{\pm} = R(\pm\Delta) \cdot \left(\frac{\mathbf{P}_i}{|\mathbf{P}_i|} \right), \tag{6.2}$$

where $R(\pm\Delta)$ denotes a rotation by the deviation angle Δ to the left $(+)$ or to the right $(-)$ (Fig. 6.1b). In order to choose its swimming direction $\hat{\mathbf{d}}_i$ from $\hat{\mathbf{d}}_i^{\pm}$, the AP

senses the orientations $\hat{\mathbf{u}}_j$ of its close neighbours within orientation detection range R_o and determines their mean orientation

$$\langle\hat{\mathbf{u}}\rangle_i = \frac{1}{n_\mathrm{o}} \sum_{j\in V_i^{\alpha,R_\mathrm{o}}} \hat{\mathbf{u}}_j, \tag{6.3}$$

with n_o the number of APs in $V_i^{\alpha,R_\mathrm{o}}$. Then the directions $\hat{\mathbf{d}}_i^{\pm}$ are compared with $\langle\hat{\mathbf{u}}\rangle_i$ and the one with best agreement, i.e. smallest angle between them, is selected as swimming direction $\hat{\mathbf{d}}_i$ (Fig. 6.1c). In addition to this interaction, which provides a mechanism for cohesion and local order, APs try to avoid direct collisions. This behaviour has highest priority and is realised by reorienting the APs away from neighbours to the front, i.e. within vision angle π and closer than the repulsion radius R_r, similar to the repulsion in e.g. [9]. To reduce the number of adjustable parameters, radii for orientation detection and repulsion are set to $R_\mathrm{o} = 25\ \mu\mathrm{m} \approx 4\sigma$ and $R_\mathrm{r} = 8\ \mu\mathrm{m} \approx 1.25\sigma$.

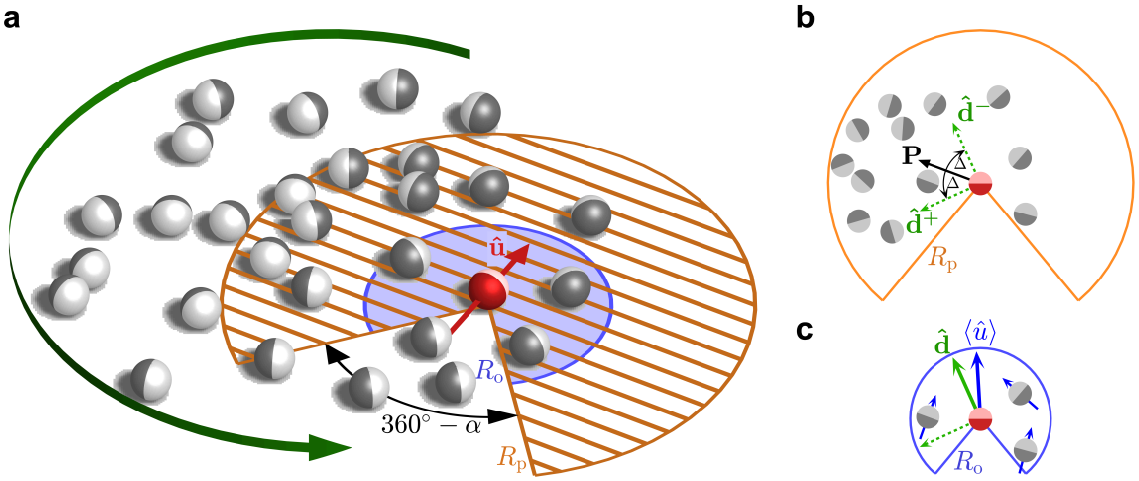

Figure 6.1: Illustration of the social interaction. **a** An AP (red) senses positions and orientations of its visible neighbours. The field of vision is centred around the AP's orientation $\hat{\mathbf{u}}$ and defined by full angle α and range R_p (orange dashed region) and R_o (blue region) for position and orientation detection, respectively. **b** From the position data, the direction $\mathbf{P}$ to the centre of mass of the (visible) group is determined. Possible swimming directions $\hat{\mathbf{d}}^+$ and $\hat{\mathbf{d}}^-$ deviate by angle Δ to the left or right from $\mathbf{P}$. **c** The swimming direction $\hat{\mathbf{d}}$ is then chosen from $\hat{\mathbf{d}}^+$ and $\hat{\mathbf{d}}^-$ to be the one that is closer to the mean orientation $\langle\hat{\mathbf{u}}\rangle$ of the APs neighbours.. [4]

6.2 Methods

6.2.1 Experimental parameters

The social interaction between APs requires active reorientation of particles depending on the position and orientation of other particles in the group. To meet these requirements, the diameter of APs is increased to $\sigma = 6.3$ µm and the thickness of the carbon coating on one hemisphere to 80 nm. With these parameters, the orientational response of APs to light gradients was found to be most reliable and the orientation detection is improved due to a better contrast between the hemispheres and an increased number of pixels per AP. The 200 nm-thick sample cells are heated to $T = 28°$ C, which is ≈ 6 K below the critical temperature of the water/lutidine mixture. Similar to the experimental conditions in Chapter 5, the motion of APs is restricted to the x-y-plane due to gravitation and the AP orientation aligns parallel to the substrate.

Self-propulsion of APs is achieved by illumination with a laser beam with beam waist $w = 5$ µm and intensity $I = 0.38$ W/mm^2 averaged over the AP area which leads to self-propulsion with velocity $v = 0.5$ µm/s. Translational and rotational diffusion constants were experimentally determined to $D_\mathrm{T} = 0.014$ µm^2/s and $D_\mathrm{R} = 0.0028$ 1/s corresponding to a reorientation time $\tau \approx 360$ s. During experiments, AP positions and orientations are acquired at a rate of 5 Hz and the supposed swimming direction of each AP is calculated. For the realisation of active reorientation, the laser beam is shifted by 1.8 µm from the AP centre, opposite to the supposed swimming direction (see below for details of the reorientation). Except otherwise stated, experiments are performed with $N \approx 50$ APs.

Experiments are started by moving all APs to the centre of the measurement area where they are stored on a hexagonal lattice until the social interaction is turned on. Although it is not necessary to obtain swarm or swirls (see e.g. Fig. 6.3b), the group of APs is typically initialised by allowing only counter-clockwise rotation, i.e. all APs have swimming direction $\hat{\mathbf{d}} = \hat{\mathbf{d}}^-$ independent of their neighbours' orientations. Without this initialisation, it is possible that the group leaves the measurement area before a steady-state forms.

6.2.2 Active reorientation

In contrast to the self-propulsion of APs under homogeneous illumination which does not influence their orientation, APs reorient in presence of a light gradient ∇I. Due to the asymmetric heating of the carbon cap, the demixing bubble of the water/lutidine becomes asymmetric which leads to a torque Γ acting on the orientation. In [72] it was shown that Γ depends on the relative misalignment γ between AP orientation $\hat{\mathbf{u}}$ and the negative direction $-\nabla I$ of the gradient according to

$$\Gamma(\gamma) = -\Gamma_\mathrm{max} \sin(\gamma), \tag{6.4}$$

with the maximum torque $\Gamma_{\max}$ when $\hat{\mathbf{u}} \perp \nabla I$. Accordingly, APs align opposite to the light gradient where the torque vanishes for $\gamma = 0$. In order to exploit this effect to dynamically align the orientation $\hat{\mathbf{u}}$ of an AP with its target direction $\hat{\mathbf{d}}$, the illumination with individual laser beams has to be changed such, that each AP is subjected to a local intensity gradient. This is realised by shifting the laser beam by 1.8 µm $\approx 0.3\sigma$ from the centre of the AP, opposite to the target direction $\hat{\mathbf{d}}$ (Fig. 6.2a), which results in a local intensity gradient $\nabla I \propto -\hat{\mathbf{d}}$. In principle, the position of the laser beam can also be defined relative to the AP's orientation $\hat{\mathbf{u}}$ rather than the target direction $\hat{\mathbf{d}}$, however, such configurations lead to less reliable reorientation in experiments.

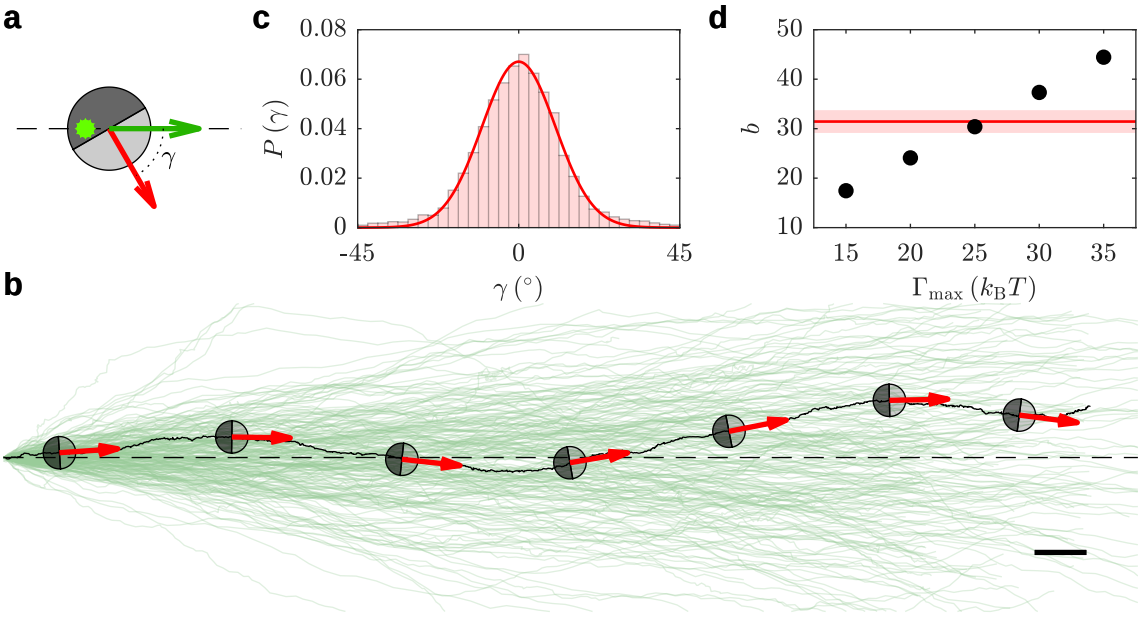

Figure 6.2: Active reorientation of APs. **a** Sketch of the experimental condition to characterise the active reorientation. Independent of the AP orientation (red arrow), the laser beam (green spot) is displaced by 1.8 µm $\approx 0.3\sigma$ opposite to the steering direction (green arrow). **b** Experimentally obtained trajectories (green) when APs are steered to the right. Scale bar is 10 µm. **c** Probability distribution of the AP orientation obtained from 20 s long segments of the trajectories (bars) and the corresponding fit to $P(\gamma) = a \exp(b \cos(\gamma))$ (solid line). **d** Comparison of the fit parameter b obtained from numerical simulations with different values $\Gamma_{\max}$ (symbols) and experiments (solid line) using an identical evaluation procedure. The standard deviation of independent experiments is shown as a shaded area. [4]

The strength of the torque acting on APs can be obtained from measurements with constant target direction $\hat{\mathbf{d}}$ as shown in Fig. 6.2b. In this situation APs align with $\hat{\mathbf{d}}$, i.e. $\gamma = 0$, however, their orientations still fluctuate due to rotational diffusion. As shown in Section 3.1.2, the probability distribution of γ is then given

by

$$P(\gamma) \propto \exp\left(\frac{\Gamma_{\max}\cos(\gamma)}{k_{\mathrm{B}}T}\right). \tag{6.5}$$

Although γ and hence $P(\gamma)$ are known from the detected orientations of the APs, this data is not suitable for the determination of $\Gamma_{\max}$ because small errors in the orientation detection lead to a broadening of the distribution and therefore cause an error in $\Gamma_{\max}$. Instead, $P(\gamma)$ is obtained from the measured trajectories of APs by evaluating the swimming direction in intervals of $\Delta t = 20$ s. The resulting distribution and the corresponding fit to $P(\gamma) = a\,\exp(b\,\cos(\gamma))$ is shown in Fig. 6.2c. Using this procedure, however, the width of the distribution shrinks with increasing time intervals Δt. Therefore, the fit parameter b obtained from experiments is compared with numerical simulation (see below) with different values of $\Gamma_{\max}$ which are evaluated with the identical procedure. As shown in Fig. 6.2d, best agreement of experimental (red solid line) and numerical (symbols) data is found for simulations with $\Gamma_{\max} = 25 k_{\mathrm{B}}T$. With the rotational mobility $\mu = \omega/\Gamma$ and the Einstein relation, the maximum torque $\Gamma_{\max}$ can be converted to a maximal rotation rate $\omega_{\max}$ according to

$$\omega_{\max} = \frac{\Gamma_{\max}}{k_{\mathrm{B}}T} D_{\mathrm{R}} \approx 4^\circ\ 1/\mathrm{s}. \tag{6.6}$$

6.2.3 Order parameters

The collective states can be characterised using two global properties of the group: the orientational and rotational order [9]. The orientational order parameter, also called polarisation, is given by

$$O_{\mathrm{P}} = \frac{1}{N}\left|\sum_{i=1}^{N}\hat{\mathbf{u}}_i\right|, \tag{6.7}$$

with N the number of APs in the group. O_{P} quantifies the directionality of the group and takes values $0 \leq O_{\mathrm{P}} \leq 1$. It reaches its maximum value $O_{\mathrm{P}} = 1$ when the orientations of all APs are aligned. The rotational order parameter is defined as

$$O_{\mathrm{R}} = \frac{1}{N}\sum_{i=1}^{N}(\hat{\mathbf{r}}_i \times \hat{\mathbf{u}}_i)\cdot\mathbf{e}_z, \tag{6.8}$$

where $\mathbf{r}_i$ is the position of AP i relative to the centre of the group. O_{R} becomes extremal with $O_{\mathrm{R}} = \pm 1$ when all APs are oriented perpendicular to their position in the group (with identical sense of rotation). Because O_{R} can take positive and negative values, equal probabilities of clockwise ($O_{\mathrm{R}} < 0$) and counter-clockwise ($O_{\mathrm{R}} > 0$) rotation of the group leads to a vanishing time-average $\langle O_{\mathrm{R}}\rangle$. Therefore, when the sense of rotation is irrelevant, the rotational order of the group is expressed by $|O_{\mathrm{R}}|$. The different collective states of a group can be classified according to their values of these order parameters into swarms (small O_{P}, small $|O_{\mathrm{R}}|$), flocks (large O_{P}, small $|O_{\mathrm{R}}|$) and swirls (small O_{P}, large $|O_{\mathrm{R}}|$).

6.2.4 Numerical simulations

Numerical simulations of the AP trajectories are obtained from the discrete integration of the overdamped coupled equations of motion of the APs (cf. Eqs. (2.12) and (2.13)). Because of the active reorientation of APs, it is convenient to define position $\mathbf{r}$ and orientation $\hat{\mathbf{u}}$ as complex values with the real (imaginary) part corresponding to the x- (y-) component. The discrete integration for AP i is then given by

$$\mathbf{r}_i(t+\tau) = \mathbf{r}_i(t) + v_i \hat{\mathbf{u}}_i \tau + \boldsymbol{\xi}_{\mathrm{T},i} \sqrt{\tau}, \tag{6.9}$$

$$\hat{\mathbf{u}}_i(t+\tau) = \hat{\mathbf{u}}_i(t) \exp\left(i \left(\frac{\Gamma_{\max}}{k_{\mathrm{B}}T} D_{\mathrm{R}} \sin(\gamma(t))\, \tau + \xi_{\mathrm{R},i} \sqrt{\tau} \right) \right), \tag{6.10}$$

with the angle γ between swimming direction $\hat{\mathbf{d}}_i$ and orientation $\hat{\mathbf{u}}_i$, and normal distributed, uncorrelated variables $\boldsymbol{\xi}_{\mathrm{T},i}$ and $\xi_{\mathrm{R},i}$, characterised by zero mean and component-wise variance $2D_{\mathrm{T}}$ and $2D_{\mathrm{R}}$, respectively. Steric interactions between APs are modelled by an event-driven treatment of collisions (similar to e.g [27]). After each integration step, the particle configuration is checked for overlapping APs with distance $< \sigma$ between them. If overlaps are found, they are recursively eliminated by increasing the distance to 1.01σ while keeping the common centre of mass constant. Especially in the case of few collisions, this method yields the same results as steric interactions modelled by a repulsive potential (Section 5.2.2).

The parameters in the numerical simulations are set to the experimental values $\tau = 0.2$ s, $v = 0.5$ µm/s, $\Gamma_{\max} = 25\, k_{\mathrm{B}}T$, $D_{\mathrm{T}} = 0.014$ µm/s^2 and $D_{\mathrm{R}} = 0.0028$ 1/s.

6.3 Results

6.3.1 Formation of stable swirls

In presence of the social interaction described above, APs move collectively and the group rotates around their centre as can be seen in an experimental snapshot (Fig. 6.3a) measured with deviation angle $\Delta = 67.5°$, vision angle $\alpha = 360°$ and position detection radius $R_{\mathrm{p}} = \infty$. The trajectories of APs in the 150 s before taking the snapshot are inserted to the video microscopy image as green lines. The dynamics of the group's rotation can be analysed using the rotational order parameter O_{R} which is plotted in Fig. 6.3b (green line). For $t < 0$ the APs are diffusive and their orientations are uncorrelated, i.e. $O_{\mathrm{R}} \approx 0$. When the social interaction is turned on at $t = 0$, the group spontaneously forms a swirl with counter-clockwise rotation ($O_{\mathrm{R}} > 0$). Due to fluctuations in the orientation of APs, the group can lose its order and O_{R} drops to zero. At this point the group can either re-establish the counter-clockwise rotation or change its sense of rotation to clockwise ($O_{\mathrm{R}} < 0$). In contrast to the collective motion of the group for a large deviation angle $\Delta = 67.5°$, the group remains in an unordered, but cohesive, state (swarm) with $O_{\mathrm{R}} \approx 0$ for

$\Delta = 0$ (black line). In this case, APs always try to approach the centre of the group and both potential swimming directions coincide, which makes the swimming direction of an AP independent of the orientations of its neighbours. These two cases illustrate that the emerging collective state of the group strongly depends on the choice of the interaction parameters.

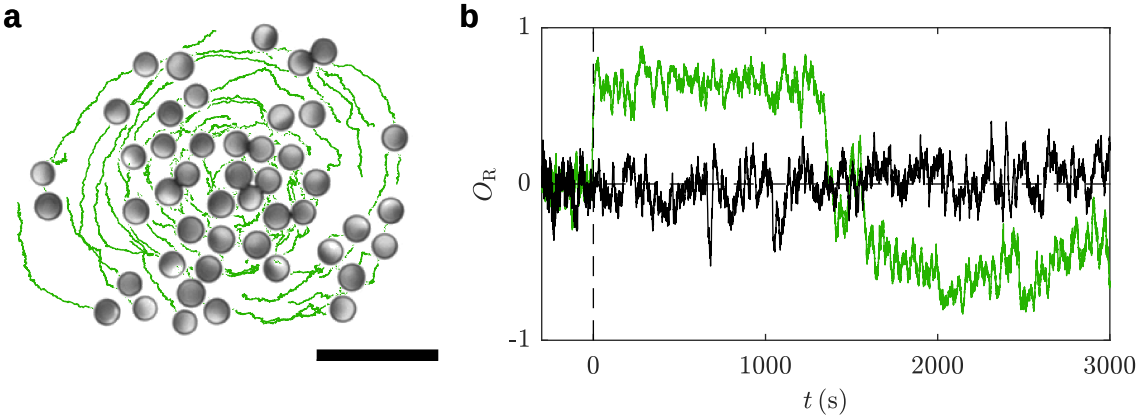

Figure 6.3: Spontaneous formation of swirls. **a** Experimental snapshot of a swirl with counter-clockwise rotation which forms for interaction parameters $\Delta = 67.5°$, $\alpha = 360°$ and $R_p = \infty$. Trajectories of 150 s are indicated as green lines. Scale bar is 30 µm. **b** Time evolution of the rotational order parameter O_R for experiments with $\Delta = 67.5°$ (green) and $\Delta = 0$ (black). At $t = 0$ the social interaction is turned on without prior initialisation of a swirl, i.e. $O_R \approx 0$ for $t < 0$. [4]

Considering an increasing deviation angle Δ, the angular motion of APs becomes more relevant and the time-average of the rotational order $\langle |O_R| \rangle$ of the group increases (Fig. 6.4a). Because the cohesion of the group relies on the component of the APs swimming direction towards the centre of the group, an increase of Δ also reduces cohesion. Therefore, the spatial extent of the group increases, i.e. the radial area fraction profile $\phi(r)$ broadens (Fig. 6.4b). This effect becomes relevant for $\Delta \gtrsim 70°$ (orange and red lines) and the average number of neighbours in the orientation detection radius R_o drops. This makes the rotational order more susceptible to fluctuations and $\langle |O_R| \rangle$ decreases. When $\Delta = 90°$, the swimming direction of APs is always perpendicular to the centre of the group and accordingly the group is no longer cohesive.

The collective behaviour is also influenced by a reduction of the sensing capabilities of APs, e.g. due to a reduction of the vision angle α and the position detection radius R_p. This leads to fewer neighbours contributing to an AP's swimming direction and therefore an increasing error in the determination of the group centre which can result in APs leaving the group. The range of α and R_p leading to the formation of cohesive swirls (green) is shown in Fig. 6.5 obtained from experiments (symbols) and numerical simulations (background) with $\Delta = 67.5°$. Here, a swirl is defined as cohesive when the radius of gyration of the group changes by less than 10 µm.

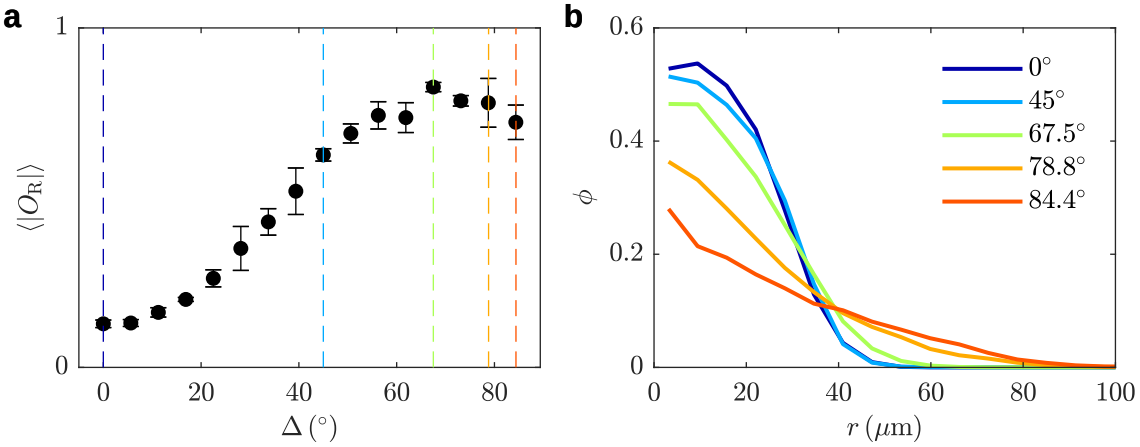

Figure 6.4: Dependence on the deviation angle Δ. **a** Mean of the absolute value of the rotational order parameter $\langle |O_R| \rangle$ vs. the deviation angle Δ. Error bars correspond to the standard deviation of different experiments. **b** Radial area fraction profiles $\phi(r)$ for $\Delta = [0°, 45°, 67.5°, 78.8°, 84.4°]$ (blue to red, dashed lines in **a**). All experiments are performed with $\alpha = 360°$ and $R_p = \infty$. [4]

This also excludes events in which APs leave the group and then come back due to rotational diffusion. Experiments and numerical simulations show good agreement, especially when considering that the simulations only take into account the motion of individual APs, but not the rather complex interactions in the experimental system, e.g. during collisions between APs. Swirls can be found for a large range of α- and R_o-values which indicates that this collective state is rather robust regarding imperfect sensing of the environment.

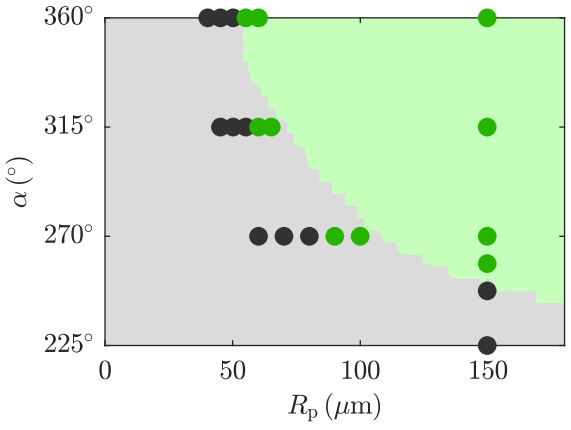

Figure 6.5: Existence of cohesive swirls (green) depending on the vision angle α and the position detection range R_p for deviation angle $\Delta = 67.5°$ obtained from experiments (symbols) and numerical simulations (background). [4]

The robustness of the swirls is an important feature of the presented social interaction. In contrast, swirls are only observed in a narrow range of interaction parameters in typical zonal models, e.g. [9]. Robustness of collective states is not only important when changing interaction parameters, but also when the group is subjected to external sources of noise. Obviously, the rotational diffusion cannot be

modified in experiments without changing various other properties of the system, however, in numerical simulations D_R can be varied. In Fig. 6.6 the green curve shows the impact of a change of D_R on $\langle|O_\mathrm{R}|\rangle$ for interaction parameters $\Delta = 67.5°$, $\alpha = 270°$, $R_\mathrm{r} = 8$ µm, $R_\mathrm{o} = 25$ µm, $R_\mathrm{p} = \infty$. Although the rotational order deteriorates with increasing noise strength, the comparison with simulations in which $\hat{\mathbf{d}}$ is calculated according to the zonal model in [9] (blue), shows that the presented interaction rule is rather robust against thermal noise. This difference can be explained by the different influence of the mean orientation $\langle\hat{\mathbf{u}}\rangle$ on $\hat{\mathbf{d}}$. Here, $\langle\hat{\mathbf{u}}\rangle$ is only used for the binary decision between $\hat{\mathbf{d}}^-$ and $\hat{\mathbf{d}}^+$ which reduces the effect of fluctuations of the orientations. Contrary to this, in zonal models individuals typically determine $\hat{\mathbf{d}}$ as a superposition of alignment with $\langle\hat{\mathbf{u}}\rangle$ and other contributions such as attraction to the group.

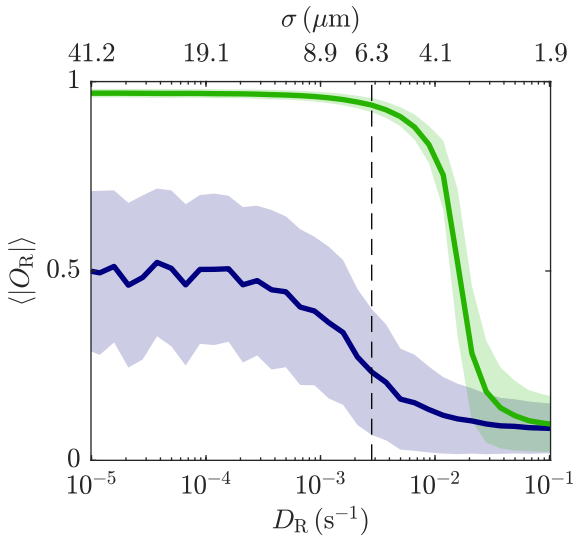

Figure 6.6: Robustness of swirl formation against rotational diffusion. $\langle|O_\mathrm{R}|\rangle$ vs. rotational diffusion constant D_R obtained from numerical simulations with parameters $R_\mathrm{r} = 8$ µm, $R_\mathrm{o} = 25$ µm, $R_\mathrm{p} = \infty$, $\Delta = 67.5°$, $\alpha = 270°$ (green). As a comparison, simulations with calculation of $\hat{\mathbf{d}}$ according to a typical zonal model [9] with (matched) parameters $r_\mathrm{r} = 8$ µm, $r_\mathrm{o} = \Delta r_\mathrm{o} + r_\mathrm{r} = 25$ µm, $r_\mathrm{a} = \Delta r_\mathrm{a} + r_\mathrm{o} = \infty$, $\alpha = 270°$ (blue). Error bands correspond to the standard deviation of 20 simulations. [4]

6.3.2 Internal dynamics of swirls

Considering the definition of the rotational order parameter O_R, perfect swirling motion is achieved when all particles move perpendicular to the vector between their position and the centre of the swirl. In this case, the radial position of APs within the swirl does not change. In addition, collisions are prevented when APs with a certain radial position r travel with a constant angular velocity $\omega(r)$. This condition could for example be met when all APs have the same velocity v independent of r leading to $\omega(r) \propto 1/r$, or when APs have a distance-dependent velocity $v \propto r$ leading to constant ω. In the latter case, APs would always have identical neighbours, but also in the first case the APs would lose their neighbours slowly. This is in strong contrast with the experimental findings. In Figs. 6.7a to 6.7d the motion of an AP (red) and its initial next neighbours (blue) at time $t = 0$ are shown for times $t = [0, 100, 300, 600]$ s. Already after 100 s the configuration changes and only

three of the initial six next neighbours remain. In the following the configuration fully randomises and the highlighted APs can be found on opposite sides of the group. The time evolution of the distances d_{ij} between AP i and its initial next neighbours j (Fig. 6.7e) shows that indeed distances rapidly increase and the mean $\langle d_{\mathrm{ij}} \rangle$ converges to the average particle distance (dashed line). These results show that perfect order is not necessary to obtain a stable swirl. From the time dependence of the probability distribution $P(\Delta\phi)$ of the angular displacement $\Delta\phi$ relative to the swirl centre (Fig. 6.7f), the mean rotation time of the swirl is determined to ≈ 600 s, corresponding to the mean of the distribution (solid line) reaching $\Delta\phi = 2\pi$. The probability distribution $P(\Delta r)$ of the radial AP displacement Δr (Fig. 6.7g) shows that APs in the experiments are not travelling on concentric orbits as assumed for a perfect swirl, but constantly change their radial position in the swirl. However, the mean of the distribution (solid line) remains at zero which demonstrates that the group is stable and does not change its spatial extent.

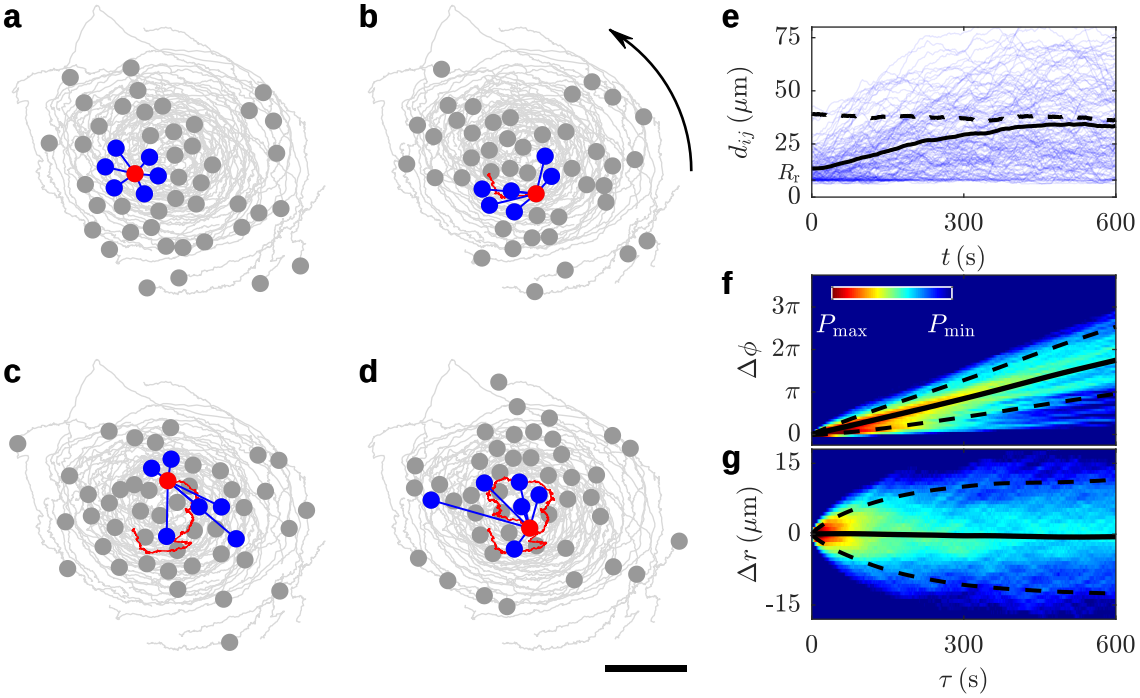

Figure 6.7: Next-neighbour correlations. **a-d** Time evolution of the AP position within a counter-clockwise rotating swirl at times $t = [0, 100, 300, 600]$ s. One AP (red) and its initial nearest neighbours (blue) at $t = 0$ are highlighted. Grey trajectories show the trajectories between $t = 0$ and $t = 600$ s. Scale bar is 30 µm. **e** Time dependence of distances d_{ij} to initial next neighbours (blue) and the corresponding average (black solid line). The average of all distances between particles is shown as a dashed line. **f**, **g** Time-dependence of the angular and radial displacements $\Delta\phi$ and Δr relative to the swirl centre. Solid and dashed lines correspond to the mean and standard deviation of the distribution, respectively. All experiments are performed with $\Delta = 67.5°$, $\alpha = 360°$ and $R_{\mathrm{p}} = \infty$. [4]

As previously mentioned, the otherwise stable rotation of swirls is sometimes interrupted by a short phase with vanishing rotational order, $O_\mathrm{R} \approx 0$, before the rotation is re-established. In these situations, the rotational direction, i.e. counter-clockwise with $O_\mathrm{R} > 0$ or clockwise with $O_\mathrm{R} < 0$, is randomised. In Fig. 6.8a the evolution of rotational order parameters O_R and the orientational order parameter O_P, i.e. polarisation of the group, is shown during a double rotational reversal. Whenever O_R is close to zero, the polarisation O_P peaks which indicates that transitions between clockwise and counter-clockwise rotation of the group are typically not via a swarm state with $O_\mathrm{R} \approx 0$ and $O_\mathrm{P} \approx 0$. This interpretation is supported when calculating the probability distribution $P(O_\mathrm{R}, O_\mathrm{P})$ (Fig. 6.8b). While the group dominantly stays in swirl state, the transition between both senses of rotation happens by forming an intermediate, metastable flock state with $O_\mathrm{R} \approx 0$ and large O_P. To get a further understanding of the microscopic details of these events, O_R can be calculated with spatial resolution. For this, the rotational order parameters $O_{\mathrm{R},i}$ is calculated for each AP i, but instead of taking the average to obtain O_R of the group, the position-dependent order $O_\mathrm{R}(x, y)$ is calculated according to

$$O_\mathrm{R}(x,y) = \frac{\sum_i O_{\mathrm{R},i} \, \exp\left(-\frac{|\mathbf{r}_i|^2}{2\,\sigma^2}\right)}{\sum_i \exp\left(-\frac{|\mathbf{r}_i|^2}{2\,\sigma^2}\right)}, \tag{6.11}$$

with distance $|\mathbf{r}_i|$ between position (x, y) and particle i. Analogue to $O_{\mathrm{R},i}$ and O_R, also $O_\mathrm{R}(x, y)$ can take values between -1 and 1. In Figs. 6.8c to 6.8h this spatially resolved order parameter is shown for the times marked in Fig. 6.8a. Spontaneous reversals typically begin from the edges of the group where APs have only few neighbours and therefore orientational fluctuations have a strong impact (blue region, Fig. 6.8d). Subsequently, the region with swapped sense of rotation grows until the group is split into two regions with opposite sense of rotation (Figs. 6.8e and 6.8f). In this situation the rotational order of the whole group vanishes, O_P becomes large and the sizes of the two regions strongly fluctuate. Because the local order within the two regions remains large, this state rapidly decays back into a swirl state with either sense of rotation. Although fluctuations can temporarily destabilise the swirling motion, the internal order of the group is not completely lost which allows a fast recovery of the rotational order.

6.3.3 Response to perturbations

In order to further investigate the robustness of the swirls, additional sources of perturbation can be introduced to the group. In groups of animals, for example, individuals can adapt their behaviour because they have access to additional information about food sources or migration routes [146]. Experimentally such effects can be realised by changing the response of some APs to their neighbours and observe the impact of these 'misbehaving' particles on the collective state of the group. In the following, the majority of APs choose, as before, the swimming direction $\hat{\mathbf{d}}$ from

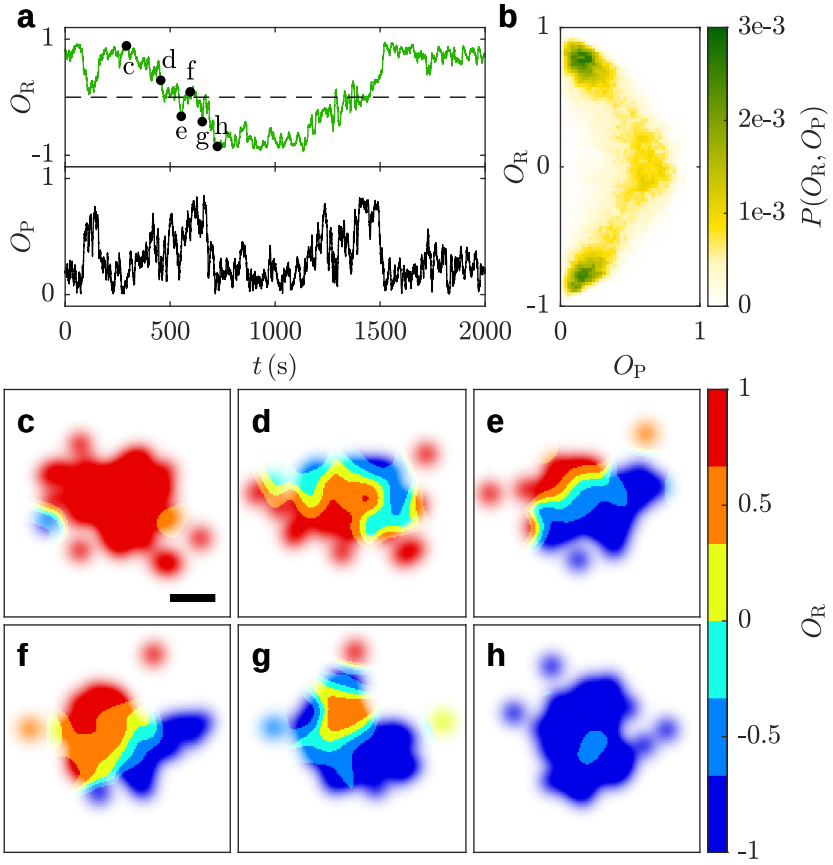

Figure 6.8: Spontaneous rotation reversal. **a** Rotational and orientational order parameters O_R and O_P vs. time during two spontaneous rotation reversals. **b** Probability distribution $P(O_R, O_P)$ obtained from measurements with ≈ 50 rotation reversals. **c-h** Spatially resolved O_R at the times marked in . Scale bar is 30 µm. All experiments are performed with $\Delta = 67.5°$, $\alpha = 360°$ and $R_p = \infty$. [4]

$\hat{\mathbf{d}}^{\pm}$ based on the orientations of their neighbours. In contrast, APs with modified response do not take into account these orientations, but always choose $\hat{\mathbf{d}} = \hat{\mathbf{d}}^{+}$. Accordingly, a group consisting of only modified APs would result in a clockwise rotating swirl. To investigate the impact of modified APs, the response of a number N_{mod} APs is changed when the group is rotating counter-clockwise. In Figs. 6.9a to 6.9f the reaction of the group is shown when five out of 50 APs with modified response are initialised in the centre of the swirl (open circles). In contrast to the spontaneous rotation reversal discussed above, now the reversal is not accompanied by large fluctuations. Instead, the modified APs transfer their sense of rotation to their neighbours which leads to a growing region of APs with clockwise rotation. Because the modified APs cannot accept counter-clockwise rotation, they stabilise this region and eventually the sense of rotation of the swirl is reversed. The impact of modified APs to the rotation of the swirl depends strongly on the number N_{mod}

(Fig. 6.9g). While a single AP is not sufficient to change the sense of rotation (dark blue), for $N_{\mathrm{mod}} \geq 5$ the swirl persistently changes to clockwise rotation (orange, dark red). For $N_{\mathrm{mod}} = 2$ (light blue), the swirl shows a preference for clockwise rotation, however, the impact of the modified APs is not strong enough to prevent counter-clockwise rotation at all times. In addition to the persistence of the reversal, larger N_{mod} also accelerates the reversal as can be seen in Fig. 6.9h where the inverse time until the group reaches $O_{\mathrm{R}} = 0$ is shown. Although the modified response of APs changes the sense of rotation of the group, in the experiments all swirls remain intact. Because the 'misbehaving' APs temporarily introduce disorder leading to an increased number of collisions between APs, a sudden change of the response of some particles could also lead to a destabilisation and fragmentation of the group.

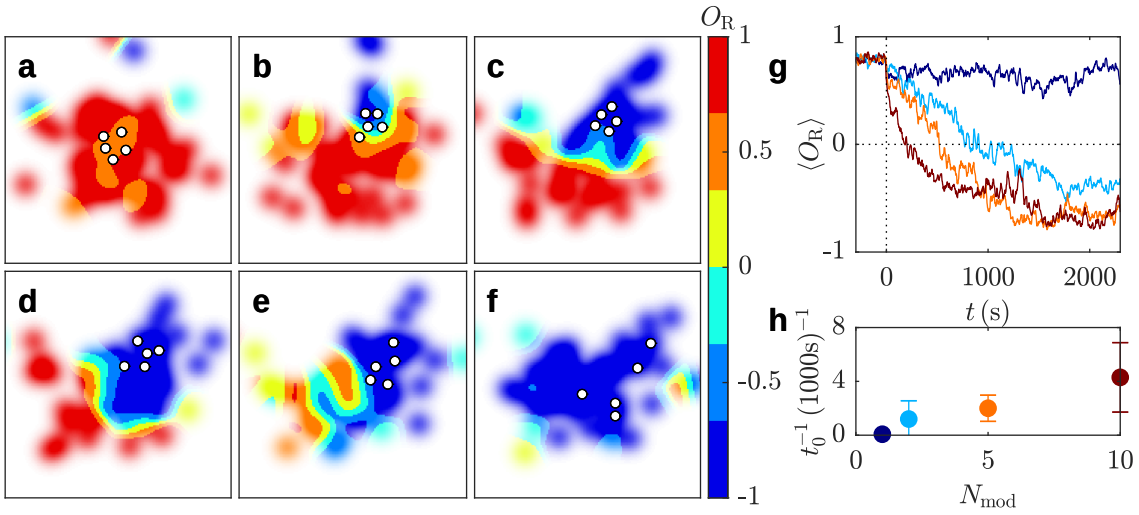

Figure 6.9: Robustness against modified AP response. **a-f** Time evolution of the spatially resolved O_{R} after $N_{\mathrm{mod}} = 5$ APs with modified response are initialised in the centre of the group (open circles). Snapshots are taken at $t = [0, 120, 240, 360, 480, 600]$ s. **g** $\langle O_{\mathrm{R}} \rangle$ vs. time for $N_{\mathrm{mod}} = [1, 2, 5, 10]$ APs with modified interaction initialised at $t = 0$. Curves correspond to the average of four different measurement. **h** Inverse time t_0^{-1} the group needs to reach $O_{\mathrm{R}} = 0$ after initialisation. Error bars correspond to the standard deviation of different measurements. All experiments are performed with $\Delta = 67.5°$, $\alpha = 360°$ and $R_{\mathrm{p}} = \infty$. [4]

Another possibility to introduce a perturbation to the swirling group of APs is the insertion of an obstacle into the centre of a swirl. In the experiments, virtual obstacles are realised as a region of increased angular deviation by increasing Δ_i depending on the position $\mathbf{r}_i$ of AP i according to

$$\Delta_i(|\mathbf{r}_i - \mathbf{r}_{\mathrm{obs}}|) = \Delta_0 + \Delta_{\mathrm{obs}} \left(\frac{1}{2} - \frac{1}{\pi} \arctan\left(\frac{|\mathbf{r}_i - \mathbf{r}_{\mathrm{obs}}| - R_{\mathrm{obs}}}{w_{\mathrm{obs}}} \right) \right), \tag{6.12}$$

with Δ_0 the deviation angle without obstacle, Δ_{obs} the additional deviation and $\mathbf{r}_{\mathrm{obs}}$, R_{obs} and w_{obs} centre, radius and width of the obstacle. Because such obstacles

are not physically manifested, APs can cross them, however, the increase of the deviation angle on the obstacle results in a preference to avoid this area. In fact, when $\Delta_0 + \Delta_{\text{obs}} > 90°$, the radial component of the swimming direction is not directed towards the centre of mass of the group but away from it. In Fig. 6.10a the resulting area fraction profiles are shown for an unperturbed swirl (green) and swirls with obstacles defined by $\Delta_{\text{obs}} = \pi/2$ and $R_{\text{obs}} = 15$ µm, $w_{\text{obs}} = 5$ µm (blue) and $R_{\text{obs}} = 30$ µm, $w_{\text{obs}} = 10$ µm (red). The corresponding trajectories are shown as insets and confirm that APs typically avoid the obstacle (orange discs), however, occasionally the trajectories lead across the edge.

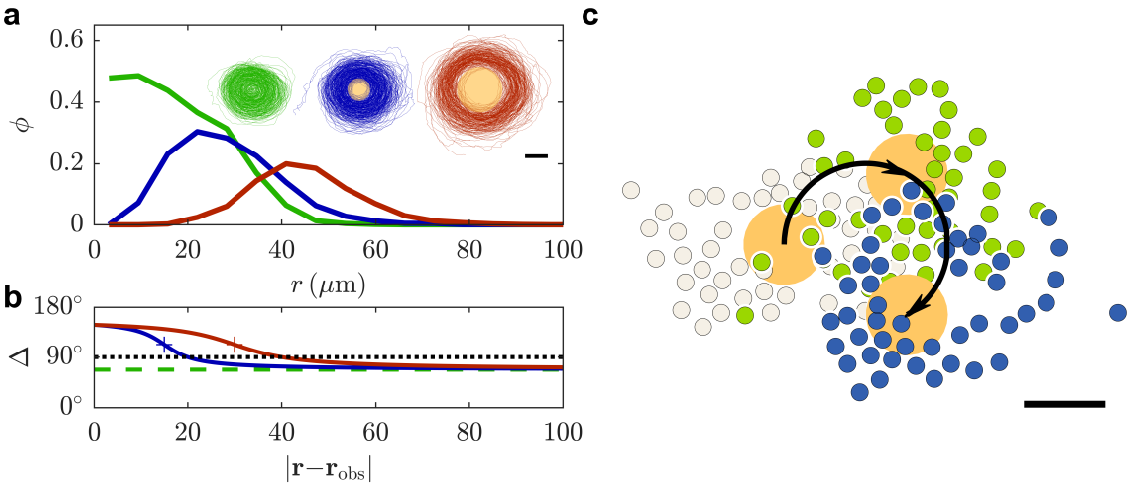

Figure 6.10: Response to obstacles. **a** Radial area fraction profiles $\phi(r)$ of swirls without (green) and with different obstacles defined by $R_{\text{obs}} = 15$ µm, $w_{\text{obs}} = 5$ µm (blue) and $R_{\text{obs}} = 30$ µm, $w_{\text{obs}} = 10$ µm (red) and $\Delta_{\text{obs}} = 90°$. The corresponding AP trajectories are shown as an inset with the obstacle as an orange disc. **b** Obstacles are realised as a distance-dependent enhancement of the deviation angle Δ depending on the distance $|\mathbf{r} - \mathbf{r}_{\text{obs}}|$ between AP position $\mathbf{r}$ and obstacle centre $\mathbf{r}_{\text{obs}}$. Colours correspond to the data in **a**. **c** Snapshots an a swirl following an obstacle with $R_{\text{obs}} = 15$ µm, $w_{\text{obs}} = 10$ µm, $\Delta_{\text{obs}} = 90°$ moving on a circular trajectory with 30 µm radius and velocity 0.025 µm/s. Different AP colours correspond to the different snapshots. All experiments are performed with $\Delta = 67.5°$, $\alpha = 360°$ and $R_{\text{p}} = \infty$. [4]

Obviously, virtual obstacles lead to a strongly reduced particle density in the centre of the group while the group rotates around the obstacle. In both cases, the maximum of the area fraction coincides with the radial distance r where $\Delta(r) \approx 90°$ (dotted line in Fig. 6.10b). At this distance, APs prefer to swim exactly tangential to the direction to the centre of mass of sensed neighbours, while APs with larger (smaller) distance to the obstacle move towards (away) from the group. In experiments with virtual obstacles, the swimming direction of APs is given by $\hat{\mathbf{d}} = \hat{\mathbf{d}}^-$ which leads to a counter-clockwise rotating swirl. Although this is not necessary for the swirl to rotate around the obstacle, the enhanced diameter of the swirl reduces

the number of close neighbours around each AP which makes the swirl more susceptible to fluctuations and, thus, spontaneous reversals of the rotation. In case of these events, the short flocking motion of the group is sufficient to move away from the obstacle.

In addition to a static obstacle, the swirl can also follow a moving obstacle (Fig. 6.10c). Here, the obstacle (orange discs) with $R_{\mathrm{obs}} = 15$ µm, $w_{\mathrm{obs}} = 5$ µm travels with a velocity of 0.025 µm/s on a circular trajectory with 30 µm radius. If the obstacle moves sufficiently slow, the swirl is able to continue to rotate around it, with an accumulation (depletion) of APs at the front (rear) of the obstacle. This effect can, potentially, be exploited to control the motion of a group of particles also in other swirling systems by inserting and translating an obstacle.

6.3.4 Critical transition between swirl and swarm

The choice of the deviation angle Δ has a drastic influence on the observed collective state of the group. While for large $\Delta = 67.5°$ stable swirls form, small $\Delta = 0$ leads to unordered swarms. In the following, the details of the transition between these two states are investigated. In Fig. 6.11a the probability distribution of $|O_{\mathrm{R}}|$ is shown for different values of Δ. When the group forms a swirl for $\Delta = 67.5°$, the distribution has a single peak around $|O_{\mathrm{R}}| \approx 0.8$ (green). A reduction of Δ first leads to a broadening of the distribution and the peak is shifted towards smaller $|O_{\mathrm{R}}|$, then also the probability at $|O_{\mathrm{R}}| = 0$ starts to increase. Most importantly, the distribution still only displays a single maximum ($\Delta = 33.8°$, blue) rather than a second peak at $O_{\mathrm{R}} = 0$. This is a first indication that the transition between swirl and swarm is continuous, analogue to a second-order phase transition in thermal equilibrium. Further decreasing Δ results in a broad distribution with a single peak at $O_{\mathrm{R}} = 0$ which becomes sharper until $\Delta = 0$.

Further details about the transition can be obtained from the susceptibility χ which quantifies the response of a system to a weak external field $h \approx 0$. The general definition of χ is given by

$$\chi = \frac{\partial \langle O \rangle}{\partial h}_{|h=0}, \tag{6.13}$$

with a time-averaged order parameter $\langle O \rangle$. According to the fluctuation-dissipation theorem, χ can be expressed in terms of the fluctuations of the order parameter O in the stationary state of the system. χ is then calculated according to

$$\chi \propto N \left(\langle O^2 \rangle - \langle O \rangle^2 \right), \tag{6.14}$$

with N the particle number [53, 147]. In order to evaluate χ for the group of APs, O_{R} is not a proper choice for the order parameter O. O_{R} can take positive and negative values, corresponding to clockwise and counter-clockwise rotation of the swirl, with equal probability and, thus, $\langle O_{\mathrm{R}} \rangle = 0$ independent of Δ. Accordingly, the choice of O_{R} leads to $\chi \propto N \langle O_{\mathrm{R}}^2 \rangle$ which increases with the rotational order.

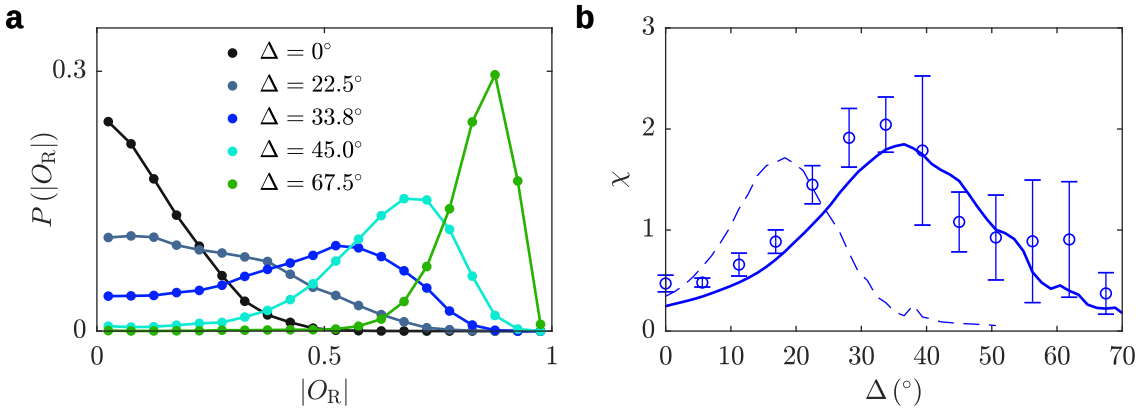

Figure 6.11: Transition between swirl and swarm. **a** Probability distribution $P(|O_\mathrm{R}|)$ for $\Delta = [0°, 22.5°, 33.8°, 45°, 67.5°]$. All experiments are performed with $\alpha = 360°$ and $R_\mathrm{p} = \infty$. **b** Corresponding susceptibility $\chi = N\left(\langle|O_\mathrm{R}|^2\rangle - \langle|O_\mathrm{R}|\rangle^2\right)$ obtained from experiments (symbols) and numerical simulations with experimental rotational diffusion constant D_R (dashed line) and effective $D_\mathrm{R,eff} = 3D_\mathrm{R}$ (solid line). Error bars correspond to the standard deviation of different experiments. [4]

This effect is analogous to the situation in the Ising model where the magnetisation m can also take positive and negative values with equal probability and $\langle m\rangle = 0$. Therefore, typically the absolute value of the magnetisation $|m|$ is used to calculate χ [147]. Similarly, the calculation of the susceptibilities of the collective states of APs is done with $|O_\mathrm{R}|$. In Fig. 6.11b the resulting susceptibility is plotted vs. the deviation angle Δ (symbols). Clearly the susceptibility peaks at intermediate $\Delta \approx 33.8°$ which further indicates a critical phase transition between swirls and swarms. The comparison of the experimental results with numerical simulations (dashed line) shows a significant shift of the susceptibility peak towards smaller Δ. This difference is not too surprising because the simulations consider only simple Langevin dynamics of the AP motion and experimental details are not covered. An important example for the differences is the collision between APs: in experiments the orientation of the involved APs typically changes while this effect is not included in simulations. In addition, also polydispersity in the motion of APs is not considered which also increases disorder in the group due to an enhancement of collisions. Because such effects dominantly lead to additional disorder of the AP orientation, in the following numerical simulations are performed with an increased rotational diffusion coefficient $D_\mathrm{R,eff}$ to account (partly) for the deviations. Best agreement with the experimental data is achieved for $D_\mathrm{R,eff} = 3D_\mathrm{R}$ (solid line in Fig. 6.11b).

To exclude the possibility that the maximum of χ is a finite size effect and to obtain further evidence for a critical phase transition, finite size scaling is performed. This method predicts the influence of the system size on the properties of the system, for example the order parameter and the susceptibility (see e.g. [147,148]). In case of a critical phase transition the correlation length diverges when the control parameter

of the system approaches the critical point. Typically this control parameter is the temperature of the system, here the deviation angle Δ controls the collective state. Because the system in experiments and simulations only has a finite size, the diverging correlation length is limited to the size of the system and as a consequence all relevant properties of the system change. However, it is possible to collapse data for different system sizes onto a single curve when the critical exponents of the system and the critical value of the control parameter are known. Adapting the formalism for finite size scaling, the rescaling of control parameter Δ, susceptibility χ and order parameter $\langle|O_\mathrm{R}|\rangle$ is given by

$$\widetilde{\Delta} = \frac{\Delta - \Delta_\mathrm{c}}{\Delta_\mathrm{c}} N^{1/\nu}, \tag{6.15}$$

$$\widetilde{\chi} = \chi N^{-\gamma/\nu}, \tag{6.16}$$

$$\widetilde{\langle|O_\mathrm{R}|\rangle} = \langle|O_\mathrm{R}|\rangle N^{\beta/\nu}. \tag{6.17}$$

Δ_c is the critical deviation angle and ν, γ, β are the critical exponents of correlation length, susceptibility and order parameter, respectively. Because experimentally the number of APs is limited due to the illumination system and the finite size of the measurement area, the finite size scaling is mainly based on numerical simulations. Simulation results with $N = [50, 100, 150, 250, 500]$ APs for χ and $\langle|O_\mathrm{R}|\rangle$ are shown in Figs. 6.12a and 6.12b. For increasing N, the peak of χ shifts towards larger Δ, i.e. towards the ordered phase, and becomes higher and sharper, $\langle|O_\mathrm{R}|\rangle$ slightly decreases with increasing N. The finite size scaling according to the equations above is performed in two steps. First, the curves of the susceptibility χ are collapsed by simultaneously fitting Δ_c, ν and γ which results in $\Delta_\mathrm{c} = 56.15°$, $\nu = 3.87$, $\gamma = 2.24$ (Fig. 6.12c). In the second step, curves of $\langle|O_\mathrm{R}|\rangle$ are collapsed. Now, only β is used as a fitting parameter which leads to $\beta = 0.66$, whereas Δ_c and ν are fixed at the previously determined values (Fig. 6.12d). Because data collapse can be achieved only partially for simulations with $N = 50$ APs (blue dotted lines), these curves are excluded from the fitting procedure. It can be speculated that at very small system sizes the singularity in the centre of the swirl additionally impacts the properties of the system. Experimentally obtained data for $N = 50$ and $N = 120$ APs is rescaled with the previously determined values of Δ_c, ν, γ and β and shows good agreement with the collapsed data, except that for $N = 50$ the experimental data shows the same deviation as the simulations. The achieved data collapse using the finite size scaling method corroborates the existence of a critical phase transition between swirls and swarms.

Landau theory

Second-order phase transitions in equilibrium can be described by the Landau theory which is explained in detail in the literature, e.g. in [149, 150]. The fundamental

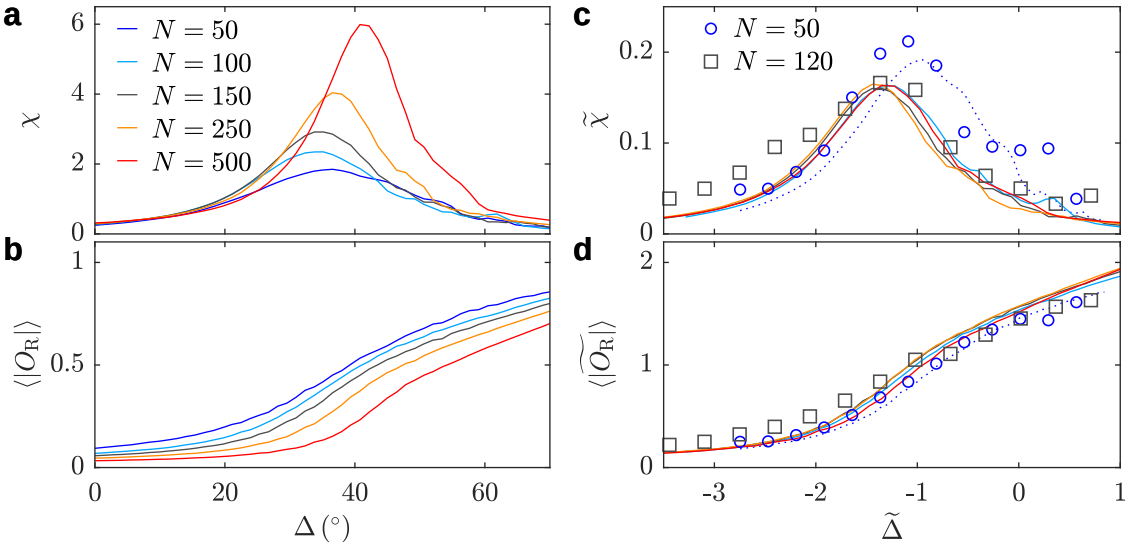

Figure 6.12: Finite size scaling. **a**,**b** χ and $\langle |O_R| \rangle$ vs. Δ obtained from numerical simulations with $N = [50, 100, 150, 200, 500]$ APs and effective rotational diffusion constant $D_{R,\text{eff}} = 3D_R$. **c**,**d** Rescaled susceptibility $\widetilde{\chi}$ and rescaled order parameter $\widetilde{\langle |O_R| \rangle}$ vs. rescaled control parameter $\widetilde{\Delta}$ for the data shown in **a** and **b** (lines). Experimental data (symbols) for $N = 50$ and $N = 120$ APs is rescaled with the parameters obtained from the collapse of the numerical data. [4]

assumption of this theory is that the free energy f of a system is given by an analytic expression which depends on an order parameter Φ. At the critical point with critical temperature T_c, the value of the order parameter changes from $\Phi = 0$ in the unordered high-temperature phase ($T > T_c$) to a finite value $\Phi \neq 0$ in the ordered low-temperature phase ($T < T_c$). Because Φ is small near the critical point, the free energy $f(\Phi)$ can be expanded to

$$f(\Phi) \approx f_0 + a(T)\,\Phi^2 + b(T)\,\Phi^4, \tag{6.18}$$

with temperature-dependent coefficients $a(T)$ and $b(T)$. In absence of an external field, odd terms in the expansion typically vanish due to the symmetry of the order parameter and the resulting requirement $f(\Phi) = f(-\Phi)$. To ensure that the equilibrium state has a bounded value of Φ, $b(T)$ needs to be positive [150]. Because $f(\Phi)$ has a minimum at $\Phi = 0$ for $T > T_c$ and symmetric minima at $\Phi \neq 0$ for $T < T_c$, $a(T)$ needs to change its sign at $T = T_c$. Sufficiently close to the critical point, it is assumed that $b(T) = b_0$ and $a(T) = a_0\,(T - T_c)$ which leads to

$$f(\Phi) \approx f_0 + a_0\,(T - T_c)\,\Phi^2 + b_0\,\Phi^4. \tag{6.19}$$

Although the group of APs with social interaction is out-of-equilibrium, this formalism can be adapted to the phase transition between swirl and swarm under

the assumption that the group has an analogue f' to the free energy f, and that the order parameter $|O_\mathrm{R}|$ is Boltzmann distributed. Then

$$\frac{P(|O_\mathrm{R}|)}{P_0} = \exp\left(\beta' \, \Delta f'\right), \tag{6.20}$$

with P_0 the probability for $|O_\mathrm{R}| = 0$, $\Delta f' = f'_0 - f'(|O_\mathrm{R}|)$ the potential difference and β' an effective temperature. Defining $f'_0 = 0$ the analogue of the free energy is given by

$$f' = -\frac{1}{\beta'} \, \ln\left(\frac{P(|O_\mathrm{R}|)}{P_0}\right). \tag{6.21}$$

If the Landau theory is applicable to the transition between swirl and swarm, the resulting potentials can be expressed as

$$f'(|O_\mathrm{R}|) = a(\Delta) \, |O_\mathrm{R}|^2 + b \, |O_\mathrm{R}|^4, \tag{6.22}$$

with $a(\Delta) = a_0 \, (\Delta_\mathrm{c} - \Delta)$ and b a positive constant. Because $\Delta > \Delta_\mathrm{c}$ corresponds to the ordered phase, the term in brackets has a different sign compared to $(T - T_\mathrm{c})$.

In Fig. 6.13a the order parameter distributions $P(|O_\mathrm{R}|)$ are shown for deviation angles $\Delta = [11°, 16.9°, 22.5°, 28.1°, 33.8°]$ close to the critical point. From these distributions, the potentials $f'(|O_\mathrm{R}|)$ are calculated (symbols in Fig. 6.13b) and all curves[1] are fitted simultaneously to Eq. (6.22) (solid lines). The result for the common parameter is $b = 8.89$ and the independently fitted parameters $a(\Delta)$ depend linearly on Δ (Fig. 6.13c). Deviations between data and fits are mainly found for large values of $|O_\mathrm{R}|$ where the expansion of $f'(|O_\mathrm{R}|)$ around $|O_\mathrm{R}| = 0$ is no longer valid and also experimental statistics deteriorate. Other possible sources of deviations from the theory, e.g. finite-size effects and the possibility to form meta-stable flock states which enhance the probability for $|O_\mathrm{R}| \approx 0$, seem to have a negligible impact. The remarkably good agreement between experimental data and the prediction of the Landau theory provides further evidence that the phase transition between swirl and swarm is critical.

Swirls in an external field

The previous results indicate some similarities between the group of APs with social interaction and the Ising model (with dimensionality $d \geq 2$), e.g. the range of the order parameter and the existence of a critical phase transition. The relevant details of the Ising model for the discussion below can be found in textbooks, e.g. [151]. To compare the phase transition in the group of APs to the Ising model, first the relevant parameters of the critical phase transition are summarised:

[1] All data points less than $2\beta'$ larger than the minimum of the corresponding curve are taken into account because statistics become insufficient for larger values of f'.

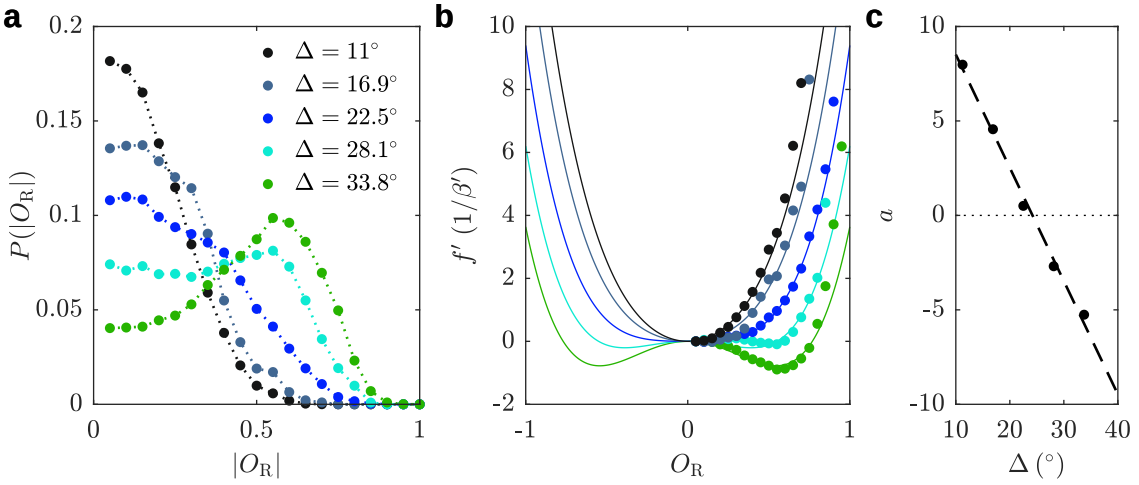

Figure 6.13: Landau theory. **a** Experimental probability distributions $P(|O_\mathrm{R}|)$ for $\Delta = [11°, 16.9°, 22.5°, 28.1°, 33.8°]$. Dotted lines are a guide to the eye. All experiments are performed with $\alpha = 360°$ and $R_\mathrm{p} = \infty$. **b** Corresponding potentials $f'(|O_\mathrm{R}|)$ (symbols) and fits to $f'(|O_\mathrm{R}|) = a(\Delta)\ |O_\mathrm{R}|^2 + b\ |O_\mathrm{R}|^4$ with b identical for all curves (lines). Fits are shown symmetrically to enhance visibility. **c** The resulting fit parameters $a(\Delta)$ (symbols) decrease linearly with Δ.

	Ising model	APs with social interaction
Order parameter	$m \in [-1, 1]$	$O_\mathrm{R} \in [-1, 1]$
Control parameter	Temperature T	Deviation angle Δ
Ordered phase	$T < T_\mathrm{c}$	$\Delta > \Delta_\mathrm{c}$

In the Ising model, a grid of N spins in d dimensions is considered which can either point up or down so that spin i can take values $s_i = \pm 1$. These spins interact with their nearest neighbours j via the ferromagnetic coupling constant $J > 0$ and they also couple to an external magnetic field h. The energy of the system is then given by

$$E = -\sum_{ij} J s_i s_j - \sum_{i=1}^{N} h s_i. \tag{6.23}$$

Considering the case without external field, i.e. $h = 0$, the system shows a critical phase transition at temperature T_c when $d \geq 2$. Identical to the above discussion of the Landau theory, the free energy of the system has one minimum for $T > T_\mathrm{c}$ at $m = 0$ (unordered phase) and two symmetric minima for $T < T_\mathrm{c}$ at $m \neq 0$ (ordered phase). In presence of an external field $h \neq 0$, an additional linear contribution is added to the free energy. In the unordered phase, this just shifts the position of the minimum. In the ordered phase, however, the linear term breaks the symmetry between the two minima. When h is small, a potential barrier remains between the local minimum and the global minimum of the free energy, which prevents the

system from reaching the global minimum. This leads to hysteresis as the final state of the system depends on its initial state. For larger h, the local minimum vanishes and the system reaches the global minimum.

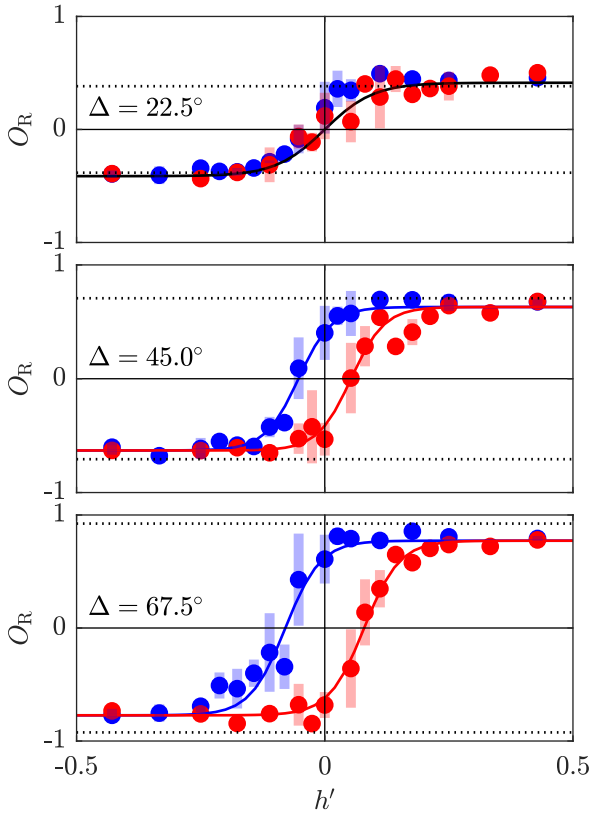

Figure 6.14: Hysteresis of swirls in an external field. O_R vs. external field h' for $\Delta = [22.5°, 45°, 67.5°]$ (top to bottom) when swirls are prepared with $h' = +\infty$ (blue) or $h' = -\infty$ (red), corresponding to a clockwise ($O_R < 0$) or counter-clockwise ($O_R > 0$) rotating swirl, respectively. Solid lines are a fit of both branches to $O_R = a \tanh(b\,(h \pm c))$ and thus the curves are symmetrically shifted from $h' = 0$. For $\Delta = 22.5°$, $c = 0$ is fixed because no hysteresis is observed. Dotted lines indicate the saturation value $O_R = \sin(\Delta)$ of an ideal swirl. Error bars correspond to the standard deviation of different experiments. All experiments are performed with $\alpha = 360°$ and $R_p = \infty$.

Although it is unclear if such energetic considerations could be made in the system of APs, qualitatively the situation is similar to the Ising model. The orientation of AP i is coupled to its neighbours in the orientation detection zone R_o via their mean orientation $\langle\hat{\mathbf{u}}\rangle_i$ which decides the swimming direction $\hat{\mathbf{d}}_i$ from $\hat{\mathbf{d}}_i^{\pm}$. The analogue to the external field h can be realised when the choice of $\hat{\mathbf{d}}_i$ does not solely rely on $\langle\hat{\mathbf{u}}\rangle_i$ anymore, but one of the orientations $\hat{\mathbf{d}}_i^+$ or $\hat{\mathbf{d}}_i^-$ is preferred. This preference can be added as an modification of $\langle\hat{\mathbf{u}}\rangle_i$ according to

$$\widetilde{\langle\hat{\mathbf{u}}\rangle}_i = \langle\hat{\mathbf{u}}\rangle_i + h'\,(-\mathbf{P}_i \times \mathbf{e}_z)\,, \tag{6.24}$$

with the external field h' and $\mathbf{P}_i$ the direction to the centre of mass of sensed neighbours in the position detection range[2]. For $h' > 0$ this corresponds to a preference for $\hat{\mathbf{d}}^-$ and accordingly counter-clockwise rotating swirls with $O_R > 0$.

To measure the effect of the external field, first the swirl is prepared in a clockwise or counter-clockwise rotating state, i.e. $h' = -\infty$ and $h' = \infty$, respectively.

[2] Because measurements with external field are performed with $\alpha = 360°$ and $R_p = \infty$, $\mathbf{P}_i$ is antiparallel to the position of the AP in the group, i.e. $-\mathbf{P}_i = \mathbf{r}_i$.

Then the external field is suddenly switched to its supposed value and the order parameter O_{R} is recorded for 30 min. It is important that swirls are unlikely to have spontaneous rotational reversals within this time interval as otherwise the hysteresis cannot be measured. In Fig. 6.14 the resulting O_{R} vs. h' curves are shown for $\Delta = [22.5°, 45°, 67.5°]$ for clockwise (red) and counter-clockwise (blue) rotating initial swirls. Clearly, for $\Delta = 45°$ and $\Delta = 67.5°$ hysteresis is observed while for $\Delta = 22.5°$ the order parameter is independent of the initial sense of rotation. These findings are in agreement with the expectation from the Ising model as $\Delta = 45°$ and $\Delta = 67.5°$ are in the ordered phase while $\Delta = 22.5° \lesssim \Delta_{\mathrm{c}}$. As a guide to the eye, the data of both branches is simultaneously fitted to $O_{\mathrm{R}} = a \tanh(b\ (h' \pm c))$ with fitting parameters a, b and c, which confirms that the observed hysteresis is symmetrical.

In contrast to the Ising model in which an infinite external field $h = \pm\infty$ yields $m = \pm 1$ for any finite temperature, here the saturation value depends on Δ. To explain this feature, an ideal, counter-clockwise rotating group is considered. In this case, the orientation of every AP is misaligned by Δ to the right from the direction to the centre of the group. However, this does not yield $O_{\mathrm{R}} = 1$ because, per definition, $O_{\mathrm{R}} = 1$ requires that all APs are oriented perpendicular to their position in the group. Accordingly, even an ideal swirl will have a saturation value $O_{\mathrm{R}}^{\mathrm{max}} = \sin(\Delta)$ (dotted lines in Fig. 6.14).

6.4 Summary

The formation of collective states is found in various animal species. For the groups it is important to be robust against noise and perturbations, yet be able to adapt the behaviour to external stimuli, such as the presence of a predator. Therefore, it is expected that groups of animals exist close to a critical phase transition between ordered and unordered states.

In this chapter I presented the implementation of a social interaction rule into a group of active Brownian particles. This interaction rule is designed to produce cohesive groups and additionally reduce collisions by avoidance of regions with high density and enhancement of the local order. Depending on the interaction parameters, stable swirls and swarms were observed which are remarkably robust against external and internal perturbation. Upon varying a single interaction parameter a critical phase transition between swirls and swarms can be triggered. Using the susceptibility of the emerging collective states and finite size scaling, the critical nature of this transition was confirmed. Furthermore, the order parameter distribution close to the phase transition is in agreement with the predictions of the Landau theory for a critical phase transition in thermal equilibrium. Motivated by the similarities between Ising model and the observed collective behaviour, the response of swirls to an external field was investigated. Analogue to the magnetisation of the Ising model in an external field, swirls show hysteresis in their sense of rotation.

Chapter 7

Conclusion and outlook

In this thesis I developed and applied an experimental system to control the self-propulsion of active Brownian particles individually. This is realised by combining a light-activated propulsion mechanism with feedback controlled laser illumination. Using an acousto-optical deflector, each particle is illuminated independently with a focused laser beam, whose intensity sets the propulsion velocity. To adjust the propulsion direction, the position of the laser beam is shifted from the particle centre leading to active reorientation. Because both velocity and direction of the propulsion can be controlled, it is possible to freely program interactions between the active Brownian particles.

In the first application of the experimental system, single particles were navigated towards a target using different control strategies that determine the propulsion velocity. The comparison of these strategies, regarding different possible limitations of resources, revealed that none of the applied strategies is superior in all aspects. This illustrates the relevance of a suitable control strategy to navigate active particles in possible future applications as e.g. drug delivery in medicine or the controlled assembly of structures.

The focus of this thesis is on the investigation of collective phenomena in groups of active Brownian particles. Therefore, different biologically motivated interaction rules have been applied. Based on the positions and orientations of all particles in the system, the supposed propulsion velocity and direction of each particle is calculated and the laser illumination is adjusted accordingly.

The first interaction rule resembles the quorum sensing of bacteria. Particles switch between active and diffusive motion, depending on the local particle density that is obtained from the concentration of virtual signalling molecules. This results in the formation of clusters with variable size and density, determined by the interaction parameters. In contrast to the phase separation of permanently active Brownian particles, cluster formation by quorum sensing is observed at significantly smaller swimming velocity and particle density. However, in both cases clusters are not cohesive and can only coexist with a dilute gas surrounding them. In order to achieve cohesion, it is necessary that particles move preferentially towards the cluster. This was realised by adding a restricted field of vision around the orientation of each particle. Thereby the interaction between particles becomes non-reciprocal and it is possible to achieve the required preference. When particles are active only

in case they perceive a large fraction of the group, this leads to the formation of cohesive dynamic groups without the need of alignment or attraction.

In the last chapter, a significantly more complex interaction rule was presented. This rule is motivated by the preference of animals to remain close to the group while also avoiding collisions. According to this rule, particles first sense the positions of their neighbours to determine the direction to the centre of the group. Then they choose their propulsion direction to deviate by a fixed angle from this direction and to maximise the alignment with close neighbours. Depending on the choice of interaction parameters, the formation of remarkably robust, cohesive swirls and swarms was observed. It was found that the change of the deviation angle triggers a critical phase transition between these two states. Because it is expected that animals often form collective states close to a critical point, these findings are particularly important for the understanding of collective behaviour. Although the details of the interaction rule are not identical to the interactions in real animals, it was confirmed that a change of interaction parameters can indeed trigger a critical phase transition between different collective states.

The experimental results presented in this thesis do not completely exhaust the possibilities of the experimental system. Therefore I want to point out some future experiments that have the potential to further deepen the understanding of collective behaviour.

So far, the social interaction introduced in the last chapter was investigated regarding the formation of swirls and the phase transition between swirls and swarms. However, simulations show that a suitable choice of interaction parameters, in particular a large value of the orientation detection radius, also leads to the formation of flocks. Detailed investigation of these flocks and the transition between flocks and swarms as well as flocks and swirls can be expected to reveal interesting results. Because of the centre of mass motion of flocks, however, this requires a modification of the experimental setup to increase the accessible area to perform measurements with sufficient statistics. Furthermore, adding interactions with a simulated predator can help to understand escape mechanisms that are observed in nature.

In addition to biologically motivated problems, the experimental system can also be used in a more technical context. For example, it is possible to test the applicability of machine learning algorithms in presence of noise and imperfections, which can be relevant for the development of autonomous microrobots.

Bibliography

[1] Haeufle, D. F. B., Bäuerle, T., Steiner, J., Bremicker, L., Schmitt, S. & Bechinger, C. External control strategies for self-propelled particles: Optimizing navigational efficiency in the presence of limited resources. *Phys. Rev. E* **94**, 012617 (2016).

[2] Bäuerle, T., Fischer, A., Speck, T. & Bechinger, C. Self-organization of active particles by quorum sensing rules. *Nat. Commun.* **9**, 3232 (2018).

[3] Lavergne, F. A., Wendehenne, H., Bäuerle, T. & Bechinger, C. Group formation and cohesion of active particles with visual perception–dependent motility. *Science* **364**, 70–74 (2019).

[4] Bäuerle, T., Löffler, R. C. & Bechinger, C. Formation of stable and responsive collective states in suspensions of active colloids. *Nat. Commun.* **11**, 2547 (2020).

[5] Heylighen, F. The science of self-organization and adaptivity. *The encyclopedia of life support systems* **5**, 253–280 (2001).

[6] Camazine, S., Deneubourg, J.-L. & Franks, N. R. *Self-organization in biological systems* (Princeton University Press, 2003).

[7] Couzin, I. D. & Krause, J. Self-organization and collective behavior in vertebrates. *Adv. Study Behav.* **32**, 1–75 (2003).

[8] Vicsek, T. & Zafeiris, A. Collective motion. *Phys. Rep.* **517**, 71 – 140 (2012). Collective motion.

[9] Couzin, I. D., Krause, J., James, R., Ruxton, G. D. & Franks, N. R. Collective memory and spatial sorting in animal groups. *J. Theor. Biol.* **218**, 1–12 (2002).

[10] Calovi, D. S., Lopez, U., Ngo, S., Sire, C., Chaté, H. & Theraulaz, G. Swarming, schooling, milling: phase diagram of a data-driven fish school model. *New J. Phys.* **16**, 015026 (2014).

[11] Lukeman, R., Li, Y.-X. & Edelstein-Keshet, L. Inferring individual rules from collective behavior. *Proc. Natl. Acad. Sci. U.S.A.* **107**, 12576–12580 (2010).

[12] Herbert-Read, J. E., Perna, A., Mann, R. P., Schaerf, T. M., Sumpter, D. J. T. & Ward, A. J. W. Inferring the rules of interaction of shoaling fish. *Proc. Natl. Acad. Sci. U.S.A.* **108**, 18726–18731 (2011).

[13] Gautrais, J., Ginelli, F., Fournier, R., Blanco, S., Soria, M., Chaté, H. & Theraulaz, G. Deciphering interactions in moving animal groups. *PLoS Comput. Biol.* **8**, 1–11 (2012).

[14] Filella, A., Nadal, F., Sire, C., Kanso, E. & Eloy, C. Model of collective fish behavior with hydrodynamic interactions. *Phys. Rev. Lett.* **120**, 198101 (2018).

[15] Ashkin, A., Dziedzic, J. M., Bjorkholm, J. E. & Chu, S. Observation of a single-beam gradient force optical trap for dielectric particles. *Opt. Lett.* **11**, 288–290 (1986).

[16] Gasser, U., Weeks, E. R., Schofield, A., Pusey, P. N. & Weitz, D. A. Real-space imaging of nucleation and growth in colloidal crystallization. *Science* **292**, 258–262 (2001).

[17] Gasser, U., Eisenmann, C., Maret, G. & Keim, P. Melting of crystals in two dimensions. *ChemPhysChem* **11**, 963–970 (2010).

[18] van Blaaderen, A. & Wiltzius, P. Real-space structure of colloidal hard-sphere glasses. *Science* **270**, 1177–1179 (1995).

[19] Bohlein, T., Mikhael, J. & Bechinger, C. Observation of kinks and antikinks in colloidal monolayers driven across ordered surfaces. *Nat. Mater.* **11**, 126–130 (2012).

[20] Blickle, V., Speck, T., Helden, L., Seifert, U. & Bechinger, C. Thermodynamics of a colloidal particle in a time-dependent nonharmonic potential. *Phys. Rev. Lett.* **96**, 070603 (2006).

[21] Blickle, V. & Bechinger, C. Realization of a micrometre-sized stochastic heat engine. *Nat. Phys.* **8**, 143–146 (2012).

[22] Seifert, U. Stochastic thermodynamics, fluctuation theorems and molecular machines. *Rep. Prog. Phys.* **75**, 126001 (2012).

[23] Ciliberto, S. Experiments in stochastic thermodynamics: Short history and perspectives. *Phys. Rev. X* **7**, 021051 (2017).

[24] Paxton, W. F., Kistler, K. C., Olmeda, C. C., Sen, A., St. Angelo, S. K., Cao, Y., Mallouk, T. E., Lammert, P. E. & Crespi, V. H. Catalytic nanomotors: autonomous movement of striped nanorods. *J. Am. Chem. Soc.* **126**, 13424–13431 (2004).

[25] Bechinger, C., Di Leonardo, R., Löwen, H., Reichhardt, C., Volpe, G. & Volpe, G. Active particles in complex and crowded environments. *Rev. Mod. Phys.* **88**, 045006 (2016).

[26] Buttinoni, I., Volpe, G., Kümmel, F., Volpe, G. & Bechinger, C. Active Brownian motion tunable by light. *J. Phys.: Condens. Matter* **24**, 284129 (2012).

[27] Palacci, J., Sacanna, S., Steinberg, A. P., Pine, D. J. & Chaikin, P. M. Living crystals of light-activated colloidal surfers. *Science* **339**, 936–940 (2013).

[28] Qian, B., Montiel, D., Bregulla, A., Cichos, F. & Yang, H. Harnessing thermal fluctuations for purposeful activities: the manipulation of single microswimmers by adaptive photon nudging. *Chem. Sci.* **4**, 1420–1429 (2013).

[29] Krause, J. & Ruxton, G. D. *Living in groups* (Oxford University Press, 2002).

[30] Jolles, J. W., Boogert, N. J., Sridhar, V. H., Couzin, I. D. & Manica, A. Consistent individual differences drive collective behavior and group functioning of schooling fish. *Curr. Biol.* **27**, 2862 – 2868.e7 (2017).

[31] Ward, A. J. W., Herbert-Read, J. E., Sumpter, D. J. T. & Krause, J. Fast and accurate decisions through collective vigilance in fish shoals. *Proc. Natl. Acad. Sci. U.S.A.* **108**, 2312–2315 (2011).

[32] Muro, C., Escobedo, R., Spector, L. & Coppinger, R. P. Wolf-pack (Canis lupus) hunting strategies emerge from simple rules in computational simulations. *Behav. Process.* **88**, 192 – 197 (2011).

[33] Attanasi, A., Cavagna, A., Del Castello, L., Giardina, I., Melillo, S., Parisi, L., Pohl, O., Rossaro, B., Shen, E., Silvestri, E. & Viale, M. Collective behaviour without collective order in wild swarms of midges. *PLoS Comput. Biol.* **10**, 1–10 (2014).

[34] Czirók, A., Ben-Jacob, E., Cohen, I. & Vicsek, T. Formation of complex bacterial colonies via self-generated vortices. *Phys. Rev. E* **54**, 1791–1801 (1996).

[35] Couzin, I. D. & Franks, N. R. Self-organized lane formation and optimized traffic flow in army ants. *Proc. R. Soc. Lond. B Biol. Sci.* **270**, 139–146 (2003).

[36] Ballerini, M., Cabibbo, N., Candelier, R., Cavagna, A., Cisbani, E., Giardina, I., Lecomte, V., Orlandi, A., Parisi, G., Procaccini, A., Viale, M. & Zdravkovic, V. Interaction ruling animal collective behavior depends on topological rather than metric distance: Evidence from a field study. *Proc. Natl. Acad. Sci. U.S.A.* **105**, 1232–1237 (2008).

[37] Partridge, B. L. & Pitcher, T. J. The sensory basis of fish schools: relative roles of lateral line and vision. *J. Comp. Physiol.* **135**, 315–325 (1980).

[38] Delcourt, J., Bode, N. W. F. & Denoël, M. Collective vortex behaviors: Diversity, proximate, and ultimate causes of circular animal group movements. *Q. Rev. Biol.* **91**, 1–24 (2016).

[39] Tunstrøm, K., Katz, Y., Ioannou, C. C., Huepe, C., Lutz, M. J. & Couzin, I. D. Collective states, multistability and transitional behavior in schooling fish. *PLoS Comput. Biol.* **9**, 1–11 (2013).

[40] Downes, J. A. The swarming and mating flight of Diptera. *Annu. Rev. Entomol.* **14**, 271–298 (1969).

[41] Kelley, D. H. & Ouellette, N. T. Emergent dynamics of laboratory insect swarms. *Sci. Rep.* **3**, 1073 (2013).

[42] Cavagna, A., Cimarelli, A., Giardina, I., Parisi, G., Santagati, R., Stefanini, F. & Viale, M. Scale-free correlations in starling flocks. *Proc. Natl. Acad. Sci. U.S.A.* **107**, 11865–11870 (2010).

[43] Buhl, J., Sumpter, D. J. T., Couzin, I. D., Hale, J. J., Despland, E., Miller, E. R. & Simpson, S. J. From disorder to order in marching locusts. *Science* **312**, 1402–1406 (2006).

[44] Couzin, I. Collective minds. *Nature* **445**, 715–715 (2007).

[45] Vicsek, T., Czirók, A., Ben-Jacob, E., Cohen, I. & Shochet, O. Novel type of phase transition in a system of self-driven particles. *Phys. Rev. Lett.* **75**, 1226 (1995).

[46] Aoki. A simulation study on the schooling mechanism in fish. *Bull. Japan. Soc. Sci. Fish.* **48**, 1081–1088 (1982).

[47] Huth, A. & Wissel, C. The simulation of the movement of fish schools. *J. Theor. Biol.* **156**, 365–385 (1992).

[48] Vicsek, T. *Fluctuations and scaling in biology* (Oxford University Press Oxford, 2001).

[49] Grégoire, G. & Chaté, H. Onset of collective and cohesive motion. *Phys. Rev. Lett.* **92**, 025702 (2004).

[50] Ginelli, F. The physics of the Vicsek model. *Eur. Phys. J.: Special Topics* **225**, 2099–2117 (2016).

[51] Gautrais, J., Jost, C. & Theraulaz, G. Key behavioural factors in a self-organised fish school model. *Ann. Zool. Fenn.* **45**, 415 – 428 (2008).

[52] Hemelrijk, C. K. & Hildenbrandt, H. Self-organized shape and frontal density of fish schools. *Ethology* **114**, 245–254 (2008).

[53] Calovi, D. S., Lopez, U., Schuhmacher, P., Chaté, H., Sire, C. & Theraulaz, G. Collective response to perturbations in a data-driven fish school model. *J. R. Soc. Interface* **12**, 20141362 (2015).

[54] Mora, T. & Bialek, W. Are biological systems poised at criticality? *J. Stat. Phys.* **144**, 268–302 (2011).

[55] Muñoz, M. A. Colloquium: criticality and dynamical scaling in living systems. *Rev. Mod. Phys.* **90**, 031001 (2018).

[56] Feinerman, O., Pinkoviezky, I., Gelblum, A., Fonio, E. & Gov, N. S. The physics of cooperative transport in groups of ants. *Nat. Phys.* **14**, 683–693 (2018).

[57] Gelblum, A., Pinkoviezky, I., Fonio, E., Ghosh, A., Gov, N. & Feinerman, O. Ant groups optimally amplify the effect of transiently informed individuals. *Nat. Commun.* **6**, 7729 (2015).

[58] Attanasi, A., Cavagna, A., Del Castello, L., Giardina, I., Melillo, S., Parisi, L., Pohl, O., Rossaro, B., Shen, E., Silvestri, E. & Viale, M. Finite-size scaling as a way to probe near-criticality in natural swarms. *Phys. Rev. Lett.* **113**, 238102 (2014).

[59] Cavagna, A., Conti, D., Creato, C., Del Castello, L., Giardina, I., Grigera, T. S., Melillo, S., Parisi, L. & Viale, M. Dynamic scaling in natural swarms. *Nat. Phys.* **13**, 914–918 (2017).

[60] Brown, R. XXVII. A brief account of microscopical observations made in the months of june, july and august 1827, on the particles contained in the pollen of plants; and on the general existence of active molecules in organic and inorganic bodies. *Philos. Mag.* **4**, 161–173 (1828).

[61] Purcell, E. M. Life at low Reynolds number. *Am. J. Phys* **45**, 3–11 (1977).

[62] Berg, H. C. & Brown, D. A. Chemotaxis in Escherichia coli analysed by three-dimensional tracking. *Nature* **239**, 500–504 (1972).

[63] Lauga, E. Bacterial hydrodynamics. *Annu. Rev. Fluid Mech.* **48**, 105–130 (2016).

[64] Friedrich, B. M., Riedel-Kruse, I. H., Howard, J. & Jülicher, F. High-precision tracking of sperm swimming fine structure provides strong test of resistive force theory. *J. Exp. Biol.* **213**, 1226–1234 (2010).

[65] Bayly, P. V., Lewis, B. L., Ranz, E. C., Okamoto, R. J., Pless, R. B. & Dutcher, S. K. Propulsive forces on the flagellum during locomotion of Chlamydomonas reinhardtii. *Biophys. J.* **100**, 2716–2725 (2011).

[66] Lauga, E. & Powers, T. R. The hydrodynamics of swimming microorganisms. *Rep. Prog. Phys.* **72**, 096601 (2009).

[67] Tso, W.-W. & Adler, J. Negative chemotaxis in Escherichia coli. *J. Bacteriol.* **118**, 560–576 (1974).

[68] Witman, G. B. Chlamydomonas phototaxis. *Trends Cell Biol.* **3**, 403–408 (1993).

[69] Tailleur, J. & Cates, M. E. Statistical mechanics of interacting run-and-tumble bacteria. *Phys. Rev. Lett.* **100**, 218103 (2008).

[70] Cates, M. E. Diffusive transport without detailed balance in motile bacteria: does microbiology need statistical physics? *Rep. Prog. Phys.* **75**, 042601 (2012).

[71] Mijalkov, M. & Volpe, G. Sorting of chiral microswimmers. *Soft Matter* **9**, 6376–6381 (2013).

[72] Lozano, C., Ten Hagen, B., Löwen, H. & Bechinger, C. Phototaxis of synthetic microswimmers in optical landscapes. *Nat. Commun.* **7**, 12828 (2016).

[73] Maggi, C., Simmchen, J., Saglimbeni, F., Katuri, J., Dipalo, M., De Angelis, F., Sanchez, S. & Di Leonardo, R. Self-assembly of micromachining systems powered by Janus micromotors. *Small* **12**, 446–451 (2016).

[74] Nelson, B. J., Kaliakatsos, I. K. & Abbott, J. J. Microrobots for minimally invasive medicine. *Annu. Rev. Biomed. Eng.* **12**, 55–85 (2010).

[75] Wang, J. & Gao, W. Nano/microscale motors: biomedical opportunities and challenges. *ACS Nano* **6**, 5745–5751 (2012).

[76] Patra, D., Sengupta, S., Duan, W., Zhang, H., Pavlick, R. & Sen, A. Intelligent, self-powered, drug delivery systems. *Nanoscale* **5**, 1273–1283 (2013).

[77] Dreyfus, R., Baudry, J., Roper, M. L., Fermigier, M., Stone, H. A. & Bibette, J. Microscopic artificial swimmers. *Nature* **437**, 862–865 (2005).

[78] Ghosh, A. & Fischer, P. Controlled propulsion of artificial magnetic nanostructured propellers. *Nano Lett.* **9**, 2243–2245 (2009).

[79] Zhang, L., Abbott, J. J., Dong, L., Peyer, K. E., Kratochvil, B. E., Zhang, H., Bergeles, C. & Nelson, B. J. Characterizing the swimming properties of artificial bacterial flagella. *Nano Lett.* **9**, 3663–3667 (2009).

[80] Anderson, J. L. Colloid transport by interfacial forces. *Annu. Rev. Fluid Mech.* **21**, 61–99 (1989).

[81] Paxton, W. F., Baker, P. T., Kline, T. R., Wang, Y., Mallouk, T. E. & Sen, A. Catalytically induced electrokinetics for motors and micropumps. *J. Am. Chem. Soc.* **128**, 14881–14888 (2006).

[82] Zhang, J., Zheng, X., Cui, H. & Silber-Li, Z. The self-propulsion of the spherical Pt–SiO_2 Janus micro-motor. *Micromachines* **8**, 123 (2017).

[83] Ginot, F., Theurkauff, I., Levis, D., Ybert, C., Bocquet, L., Berthier, L. & Cottin-Bizonne, C. Nonequilibrium equation of state in suspensions of active colloids. *Phys. Rev. X* **5**, 011004 (2015).

[84] Fournier-Bidoz, S., Arsenault, A. C., Manners, I. & Ozin, G. A. Synthetic self-propelled nanorotors. *Chem. Commun.* 441–443 (2005).

[85] Laocharoensuk, R., Burdick, J. & Wang, J. Carbon-nanotube-induced acceleration of catalytic nanomotors. *ACS Nano* **2**, 1069–1075 (2008).

[86] Wang, Y., Hernandez, R. M., Bartlett, D. J., Bingham, J. M., Kline, T. R., Sen, A. & Mallouk, T. E. Bipolar electrochemical mechanism for the propulsion of catalytic nanomotors in hydrogen peroxide solutions. *Langmuir* **22**, 10451–10456 (2006).

[87] Howse, J. R., Jones, R. A. L., Ryan, A. J., Gough, T., Vafabakhsh, R. & Golestanian, R. Self-motile colloidal particles: from directed propulsion to random walk. *Phys. Rev. Lett.* **99**, 048102 (2007).

[88] Brown, A. & Poon, W. Ionic effects in self-propelled Pt-coated Janus swimmers. *Soft Matter* **10**, 4016–4027 (2014).

[89] Ismagilov, R. F., Schwartz, A., Bowden, N. & Whitesides, G. M. Autonomous movement and self-assembly. *Angew. Chem. Int. Ed.* **41**, 652–654 (2002).

[90] Solovev, A. A., Mei, Y., Bermúdez Ureña, E., Huang, G. & Schmidt, O. G. Catalytic microtubular jet engines self-propelled by accumulated gas bubbles. *Small* **5**, 1688–1692 (2009).

[91] Ma, X., Wang, X., Hahn, K. & Sánchez, S. Motion control of urea-powered biocompatible hollow microcapsules. *ACS Nano* **10**, 3597–3605 (2016).

[92] Jiang, H.-R., Yoshinaga, N. & Sano, M. Active motion of a Janus particle by self-thermophoresis in a defocused laser beam. *Phys. Rev. Lett.* **105**, 268302 (2010).

[93] Bregulla, A. P., Yang, H. & Cichos, F. Stochastic localization of microswimmers by photon nudging. *ACS Nano* **8**, 6542–6550 (2014).

[94] Hanczyc, M. M., Toyota, T., Ikegami, T., Packard, N. & Sugawara, T. Fatty acid chemistry at the oil-water interface: self-propelled oil droplets. *J. Am. Chem. Soc.* **129**, 9386–9391 (2007).

[95] Thutupalli, S., Seemann, R. & Herminghaus, S. Swarming behavior of simple model squirmers. *New J. Phys.* **13**, 073021 (2011).

[96] Izri, Z., Van Der Linden, M. N., Michelin, S. & Dauchot, O. Self-propulsion of pure water droplets by spontaneous Marangoni-stress-driven motion. *Phys. Rev. Lett.* **113**, 248302 (2014).

[97] Bricard, A., Caussin, J.-B., Desreumaux, N., Dauchot, O. & Bartolo, D. Emergence of macroscopic directed motion in populations of motile colloids. *Nature* **503**, 95–98 (2013).

[98] Bricard, A., Caussin, J.-B., Das, D., Savoie, C., Chikkadi, V., Shitara, K., Chepizhko, O., Peruani, F., Saintillan, D. & Bartolo, D. Emergent vortices in populations of colloidal rollers. *Nat. Commun.* **6**, 7470 (2015).

[99] Kaiser, A., Snezhko, A. & Aranson, I. S. Flocking ferromagnetic colloids. *Sci. Adv.* **3**, e1601469 (2017).

[100] Kokot, G. & Snezhko, A. Manipulation of emergent vortices in swarms of magnetic rollers. *Nat. Commun.* **9**, 2344 (2018).

[101] Nelson, E. *Dynamical theories of Brownian motion*, vol. 3 (Princeton University Press, 1967).

[102] ten Hagen, B., van Teeffelen, S. & Löwen, H. Brownian motion of a self-propelled particle. *J. Phys.: Condens. Matter* **23**, 194119 (2011).

[103] Fily, Y. & Marchetti, M. C. Athermal phase separation of self-propelled particles with no alignment. *Phys. Rev. Lett.* **108**, 235702 (2012).

[104] Redner, G. S., Hagan, M. F. & Baskaran, A. Structure and dynamics of a phase-separating active colloidal fluid. *Phys. Rev. Lett.* **110**, 055701 (2013).

[105] Theurkauff, I., Cottin-Bizonne, C., Palacci, J., Ybert, C. & Bocquet, L. Dynamic clustering in active colloidal suspensions with chemical signaling. *Phys. Rev. Lett.* **108**, 268303 (2012).

[106] Buttinoni, I., Bialké, J., Kümmel, F., Löwen, H., Bechinger, C. & Speck, T. Dynamical clustering and phase separation in suspensions of self-propelled colloidal particles. *Phys. Rev. Lett.* **110**, 238301 (2013).

[107] Speck, T., Bialké, J., Menzel, A. M. & Löwen, H. Effective Cahn-Hilliard equation for the phase separation of active Brownian particles. *Phys. Rev. Lett.* **112**, 218304 (2014).

[108] Speck, T., Menzel, A. M., Bialké, J. & Löwen, H. Dynamical mean-field theory and weakly non-linear analysis for the phase separation of active Brownian particles. *J. Chem. Phys.* **142**, 224109 (2015).

[109] Cates, J., Michael E .and Tailleur. Motility-induced phase separation. *Annu. Rev. Condens. Matter Phys.* **6**, 219–244 (2015).

[110] Volpe, G., Buttinoni, I., Vogt, D., Kümmerer, H.-J. & Bechinger, C. Microswimmers in patterned environments. *Soft Matter* **7**, 8810–8815 (2011).

[111] Grattoni, C. A., Dawe, R. A., Seah, C. Y. & Gray, J. D. Lower critical solution coexistence curve and physical properties (density, viscosity, surface tension, and interfacial tension) of 2,6-lutidine + water. *J. Chem. Eng. Data* **38**, 516–519 (1993).

[112] Andon, R. J. L. & Cox, J. D. Phase relationships in the pyridine series. Part I. The miscibility of some pyridine homologues with water. *J. Chem. Soc.* 4601–4606 (1952).

[113] Gomez-Solano, J. R., Samin, S., Lozano, C., Ruedas-Batuecas, P., van Roij, R. & Bechinger, C. Tuning the motility and directionality of self-propelled colloids. *Scientific Reports* **7**, 14891 (2017).

[114] Das, S., Garg, A., Campbell, A. I., Howse, J., Sen, A., Velegol, D., Golestanian, R. & Ebbens, S. J. Boundaries can steer active Janus spheres. *Nat. Commun.* **6**, 8999 (2015).

[115] Samin, S. & Roij, R. Self-propulsion mechanism of active Janus particles in near-critical binary mixtures. *Phys. Rev. Lett.* **115** (2015).

[116] Saleh, B. E. A. & Teich, M. C. *Fundamentals of photonics* (Wiley, 1991).

[117] Clunie, J. C. & Baird, J. K. Interdiffusion coefficient and dynamic viscosity for the mixture 2,6-lutidine + water near the lower consolute point. *Phys. Chem. Liq.* **37**, 357–371 (1999).

[118] Köhler, A. Ein neues Beleuchtungsverfahren für mikrophotographische Zwecke. *Z. Wiss. Mikrosk. Mikrosk. Tech.* **10**, 433–440 (1893).

[119] Atherton, T. J. & Kerbyson, D. J. Size invariant circle detection. *Image Vision Comput.* **17**, 795–803 (1999).

[120] The Mathworks, Inc., Natick, Massachusetts. *MATLAB version 9.6.0.1150989 (R2019a)* (2019).

[121] Wang, W., Castro, L. A., Hoyos, M. & Mallouk, T. E. Autonomous motion of metallic microrods propelled by ultrasound. *ACS Nano* **6**, 6122–6132 (2012).

[122] Martel, S. & Mohammadi, M. Using a swarm of self-propelled natural microrobots in the form of flagellated bacteria to perform complex micro-assembly tasks. In *2010 IEEE International Conference on Robotics and Automation*, 500–505 (IEEE, 2010).

[123] Tottori, S., Zhang, L., Qiu, F., Krawczyk, K. K., Franco-Obregón, A. & Nelson, B. J. Magnetic helical micromachines: fabrication, controlled swimming, and cargo transport. *Adv. Mater.* **24**, 811–816 (2012).

[124] Grosjean, G., Lagubeau, G., Darras, A., Hubert, M., Lumay, G. & Vandewalle, N. Remote control of self-assembled microswimmers. *Sci. Rep.* **5**, 16035 (2015).

[125] Simmchen, J., Katuri, J., Uspal, W. E., Popescu, M. N., Tasinkevych, M. & Sánchez, S. Topographical pathways guide chemical microswimmers. *Nat. Commun.* **7**, 10598 (2016).

[126] Hong, Y., Blackman, N. M. K., Kopp, N. D., Sen, A. & Velegol, D. Chemotaxis of nonbiological colloidal rods. *Phys. Rev. Lett.* **99**, 178103 (2007).

[127] Dai, B., Wang, J., Xiong, Z., Zhan, X., Dai, W., Li, C.-C., Feng, S.-P. & Tang, J. Programmable artificial phototactic microswimmer. *Nat. Nanotechnol.* **11**, 1087 (2016).

[128] Ilic, O., Kaminer, I., Lahini, Y., Buljan, H. & Soljacic, M. Exploiting optical asymmetry for controlled guiding of particles with light. *ACS Photonics* **3**, 197–202 (2016).

[129] Pearce, D. J. G., Miller, A. M., Rowlands, G. & Turner, M. S. Role of projection in the control of bird flocks. *Proc. Natl. Acad. Sci. U.S.A.* **111**, 10422–10426 (2014).

[130] Gorbonos, D., Ianconescu, R., Puckett, J. G., Ni, R., Ouellette, N. T. & Gov, N. S. Long-range acoustic interactions in insect swarms: an adaptive gravity model. *New J. Phys.* **18**, 073042 (2016).

[131] Miller, M. B. & Bassler, B. L. Quorum sensing in bacteria. *Annu. Rev. Microbiol.* **55**, 165–199 (2001).

[132] Nealson, K. H. & Hastings, J. W. Bacterial bioluminescence: its control and ecological significance. *Microbiol. Rev.* **43**, 496 (1979).

[133] Lupp, C. & Ruby, E. G. Vibrio fischeri uses two quorum-sensing systems for the regulation of early and late colonization factors. *J. Bacteriol.* **187**, 3620–3629 (2005).

[134] Ruby, E. G. Lessons from a cooperative, bacterial-animal association: the Vibrio fischeri–Euprymna scolopes light organ symbiosis. *Annu. Rev. Microbiol.* **50**, 591–624 (1996).

[135] Zhu, J., Miller, M. B., Vance, R. E., Dziejman, M., Bassler, B. L. & Mekalanos, J. J. Quorum-sensing regulators control virulence gene expression in Vibrio cholerae. *Proc. Natl. Acad. Sci. U.S.A.* **99**, 3129–3134 (2002).

[136] Parsek, M. R. & Greenberg, E. P. Sociomicrobiology: the connections between quorum sensing and biofilms. *Trends Microbiol.* **13**, 27–33 (2005).

[137] Sperandio, V., Torres, A. G. & Kaper, J. B. Quorum sensing Escherichia coli regulators B and C (QseBC): a novel two-component regulatory system involved in the regulation of flagella and motility by quorum sensing in E. coli. *Mol. Microbiol.* **43**, 809–821 (2002).

[138] Trovato, A., Seno, F., Zanardo, M., Alberghini, S., Tondello, A. & Squartini, A. Quorum vs. diffusion sensing: a quantitative analysis of the relevance of absorbing or reflecting boundaries. *FEMS Microbiol. Lett.* **352**, 198–203 (2014).

[139] Magariyama, Y., Sugiyama, S. & Kudo, S. Bacterial swimming speed and rotation rate of bundled flagella. *FEMS Microbiol. Lett.* **199**, 125–129 (2001).

[140] Ben-Amotz, D. & Stell, G. Reformulation of Weeks-Chandler-Andersen perturbation theory directly in terms of a hard-sphere reference system. *J. Phys. Chem. B* **108**, 6877–6882 (2004).

[141] Siebert, J. T., Letz, J., Speck, T. & Virnau, P. Phase behavior of active Brownian disks, spheres, and dimers. *Soft Matter* **13**, 1020–1026 (2017).

[142] Rein, M., Heinß, N., Schmid, F. & Speck, T. Collective behavior of quorum-sensing run-and-tumble particles under confinement. *Phys. Rev. Lett.* **116**, 058102 (2016).

[143] van Drongelen, R., Pal, A., Goodrich, C. P. & Idema, T. Collective dynamics of soft active particles. *Phys. Rev. E* **91**, 032706 (2015).

[144] Durve, M., Saha, A. & Sayeed, A. Active particle condensation by non-reciprocal and time-delayed interactions. *Eur. Phys. J. E* **41**, 49 (2018).

[145] Fischer, A., Schmid, F. & Speck, T. Quorum-sensing active particles with discontinuous motility. *Phys. Rev. E* **101**, 012601 (2020).

[146] Couzin, I. D., Krause, J., Franks, N. R. & Levin, S. A. Effective leadership and decision-making in animal groups on the move. *Nature* **433**, 513–516 (2005).

[147] Landau, D. P. Finite-size behavior of the Ising square lattice. *Phys. Rev. B* **13**, 2997 (1976).

[148] Cardy, J. *Scaling and renormalization in statistical physics*, vol. 5 (Cambridge University Press, 1996).

[149] Cowley, R. A. Structural phase transitions I. Landau theory. *Adv. Phys.* **29**, 1–110 (1980).

[150] Chaikin, P. M. & Lubensky, T. C. *Principles of Condensed Matter Physics* (Cambridge University Press, 1995).

[151] Christensen, K. & Moloney, N. R. *Complexity and criticality*. Imperial College Press Advanced Physics Texts (World Scientific Publishing Company, 2005).

Acknowledgements

On the last page of my thesis I want to thank everyone who supported me and my work during the last years. Without ...[1], it would not have been possible to complete this work. Joking aside, there are quite a few people I want to thank explicitly.

First of all, I want to thank Professor Clemens Bechinger for giving me the opportunity to do my doctorate in his group. At all times, he was happy to discuss new results (or experimental difficulties) and his knowledge and ideas were a great help to make progress.

I also want to thank Professor Peter Nielaba for reviewing this thesis, and him and Professor Johannes Boneberg for being part of the examination committee.

In addition, I want to thank all colleagues who worked together with me on the projects I presented in this thesis. In particular, I want to mention Robert Löffler, Hugo Wendehenne and François Lavergne on the experimental side and Andreas Fischer, Professor Thomas Speck and Daniel Häufle on the theoretical side.

Moreover, I want to thank all the other former or current members of the group, especially Johannes Berner, Celia Lozano and Felix Kümmel, for their scientific input and the leisure activities, which unluckily became rarer after the group moved from Stuttgart to Konstanz.

I also want to acknowledge the organisational and technical support from Ulrike Offenbeck, Hans-Jürgen Kümmerer, Christa Mayer and Uwe Rau (Stuttgart) and Doris Drexler, Jakob Steindl and Dieter Barth (Konstanz).

Furthermore, I want to thank Johannes Berner and Hugo Wendehenne once more for being great weekday-flatmates in Konstanz.

Finally, I want to thank my wife Larissa and my family for all their support and Larissa also for proofreading the thesis.

[1] Fill in what you think your contribution was.